Light-induced Electronic Hole Dynamics and Its Application

Dissertation zur Erlangung des Doktorgrades
an der Fakultät für Mathematik, Informatik und Naturwissenschaften
Fachbereich Physik
der Universität Hamburg

vorgelegt von

Jhih-An You

Hamburg, 2016

Tag der Disputation: 21.10.2016

Folgende Gutachter empfehlen die Annahme der Dissertation:

Dr. Nina Rohringer

Prof. Dr. Franz Kärtner

Abstract

With the development of the high-energy photon sources in extreme ultraviolet (XUV) and X-ray regime, the control of the inner-shell hole dynamics becomes possible. This thesis focuses on the theoretical studies of light-induced hole dynamics. We proposes two time resolved spectroscopies based on the hole transitions between different atomic shells: the XUV-assisted high-harmonic generation (HHG) spectroscopy and Stimulation of a Transition in the Remaining Ion for a Detuned Electron Recoil (STRIDER). Both of the works are treated with 1D time-dependent configuration interaction singles (TDCIS) calculation.

In the XUV-assisted HHG spectroscopy, an additional XUV field, that coupling the two different shells is applied with a strong infrared (IR) field which drives HHG. We show that the resonant XUV field, an isolated attosecond pulse or an attosecond pulse train, can lead to excitation of inner-shell electrons and to the generation of a second HHG plateau. XUV-assisted HHG spectrum reveals the duration of the semi-classical electron trajectories. The results are interpreted by the strong-field approximation (SFA). Moreover, the coherent population transfer between inner and outer hole with attosecond pulse trains is discussed with the use of an attosecond pulse train.

In STRIDER method, an atom is ionized by an attosecond pump pulse in the presence of two coherent XUV or X-ray probe fields. The probe fields are tuned to a core-valence transition in the residual ion and induce spectral shearing of the photoelectron distributions. We show that the photoelectron-ion coincidence signal contains an interference pattern that depends on the temporal structure of the attosecond pump pulse and the stimulated core-valence transition using a neon atom. With the many-body perturbation theory, the behavior for the stimulation to the inner-core hole ($2p \leftrightarrow 1s$) shows less response time than the stimulation to outer-core hole ($2p \leftrightarrow 2s$). We stress the application of STRIDER to pulse characterization and the decay of the inner-core hole does not affect the usefulness.

Zusammenfassung

Die Entwicklung von kurzwelligen Lichtquellen im Spektralbereich von extremen ultravioletter (XUV) und Röntgenstrahlung ermöglicht die Kontrolle von dynamischen Prozessen von Rumpfelektronen. Diese Arbeit beinhaltet theoretische Studien von diesen lichtinduzierten dynamischen Prozessen von Rumpfelektronen und Löchern in den inneren Elektronenschalen. Wir entwickeln zwei verschieden zeitaufgelöste spektroskopische Methoden, die auf elektronischen Übergängen zwischen elektronischen Rumpfschalen und Valenzschalen basieren: Höhere Harmonische Generierung (HHG), die durch Rumpfanregungen mit XUV Pulsen modifiziert wird (XUV assistierende HHG), sowie die sogenannte STRIDER Methode - „Stimulation of a Transition in the Remaining Ion for Detuned Electron Recoil (STRIDER), in der Photoelektronen Spektroskopie durch stimulierte Rumpfanregungen in den verbleibenden Ionen studiert wird. Beide Prozesse werde mithilfe eines eindimensionalen Atommodells studiert und mit der zeitabhängiger Konfigurationswechselwirkungsmethode mit einfachen Elektronen-Loch Anregungen (time-dependent configuration interaction singles - TDCIS) beschrieben.

In der XUV assistierenden HHG Spektroskopie wird zusätzlich zu dem starken infrarot (IR) Laserpuls, der den HHG Prozess antreibt, ein XUV Puls angewandt, der den HHG Prozess durch die Anregung von Elektronen von Rumpf- in das freiwerdende Valenzloch modifiziert. Wir zeigen dass für die Fälle von einem resonanten, monochromen XUV Feld, für einen isolierten Attosekundenpuls, sowie für einen Zug von Attosekundenpulsen, eine Rumpfanregung während des HHG Prozesses stattfindet und ein zweites HHG Plateau entsteht. Das XUV induzierte zweite HHG Plateau gibt Aufschluss über die Dauer der Elektronentrajektorie des HHG Prozesses, der durch das IR Feld getrieben wird. Die Resultate werden mithilfe der Starkfeldnäherung (Strong-field approximation - SFA) interpretiert. Im Falle von periodischer Anwendung von Attosekundenpulsen (Pulszüge) diskutieren wir zusätzlich auch den kohärenten Transfer von Elektronen aus den Rumpf- in die Valenzschale.

In der STRIDER Methode wird ein Valenzelektron eines Atoms durch einen Attose-

kundenpuls ionisiert, bei gleichzeitiger Anwendung zweier XUV oder Röntgen Kontrollfeldes. Die Frequenz der kohärenten Kontrollfelder ist mit einer Rump-Valenzanregung des Atoms abgestimmt und jeweils etwas höher und niedriger als der resonante Übergang eingestellt. Das verbleibende / fehlende Energiequantum wird bei der resonanten Rumpfanregung dann auf das Photoelektron übertragen und dessen Spektrum wird verändert („Shearing“ des Photoelektronspektrums). Wir zeigen, dass das in Koinzidenz mit dem verbleibenden Ion gemessene Photoelektronspektrum ein Interferenzmuster aufweist, das von dem zeitlichen Verlauf des Attosekundenpulses abhängt. Als Beispiel betrachten wir Rumpf-Valenz Anregungen in Neon. Dabei, kann die zeitliche Struktur des Attosekundenpulses mit Genauigkeit einer der Methode intrinsischen Reaktionszeit rekonstruiert werden. Für den realistischen Fall dreidimensionaler Atome wenden wir Vielteilchenstörungstheorie (Many-body perturbation theory) an und stellen dabei fest, dass sich im Falle von Neon für eine resonante Rumpf-Valenz Anregung von 1s nach 2p eine deutlich kleinere Reaktionszeit als für 2s-2p ergibt. Die kurze Lebensdauer der 1s Vakanz beeinträchtigt die Methode überraschenderweise nicht. Die Anwendungen von STRIDER zur Charakterisierung von Attosekundepulsen werden diskutiert.

List of publications

- **Attosecond photoionization dynamics with stimulated core-valence transitions**
  Jhih-An You, Nina Rohringer, and Marcus Jan Dahlström
  Phys. Rev. A **93**, 033413 (2016)

- **Attosecond dynamics of light-induced resonant hole transfer in high harmonic generation**
  Jhih-An You, Marcus Jan Dahlström, and Nina Rohringer
  Submitted to *Phys. Rev. A*

List of abbreviations

ATI	above-threshold ionization
APT	attosecond pulse train
CEO	carrier envelope offset
CEP	carrier envelope phase
CI	configuration interaction
CIS	configuration interaction singles
CPA	chirped pulse amplification
DFT	density functional theory
FEL	free electron laser
FWHM	full-width at half-maximum
HHG	high-order harmonic generation
IR	infrared
PROOF	Phase-Retrieval by Omega Oscillation Filtering
RABITT	Reconstruction of Attosecond Beating By Interference of Two-photons transitions
RPAE	random phase approximation with exchange
RWA	rotating wave approximation
SAE	single active electron
SB	side band
SFA	strong field approximation
SAP	single attosecond pulse
STRIDER	Stimulation of Two Resonant and Instantaneously Detuned Electron Replicas
TDCIS	time-dependent configuration interaction singles
TDDFT	time-dependent density functional theory
TO	time orders
t-SURFF	time-dependent surface flux method
XFEL	X-ray free electron lasers
XUV	extreme ultraviolet

Contents

Chapter 1

Introduction

1.1 Laser sources

Since the invention in 1960 by Theodore H. Maiman as well as the basic theoretical work by Charles Hard Townes and Arthur Leonard Schawlow, lasers have had a huge impact on science and are widely applied in many areas from physics, chemistry and biology to medical uses. Lasers are coherent lights based on the stimulated emission of electromagnetic radiation. The spatial coherent property of a laser allows it to be focused to a tiny spot so that it can reach high intensity and to have a stable phase over a great distance. The temporal coherent property leads to a highly stable monochromatic light.

The first laser was a visible red light with the intensity in the kW/cm^{-2} scale and pulse duration in the microsecond regime. Afterwards, lasers with different frequencies ranging from visible light to infrared (IR) light were invented. For more broad applications, there are many progress on decreasing of the laser pulse duration, increasing the laser peak intensity, and extending the frequency to other ranges. To make pulses shorter, the technique of mode-locking [1], which induces a fixed-phase relationship between the longitudinal modes of the laser's resonant cavity, was introduced in the mid 60s and developed continuously afterwards. However, a short pulse requires large bandwidth, which leads to high peak powers and causes damage to the laser material through some nonlinear processes. With the technique of chirped pulse amplification (CPA) developed in the mid 1980s [2], the peak intensity can reach $10^{14}kW/cm^2$, which corresponds to the same order of the electric field felt by an electron in an atom. The setup of CPA is shown in Fig. 1.1, a stretcher in the time domain is used in order to lower the peak intensity before the amplifier and then a

compressor is used to compress the amplified pulse to extremely high intensity with its initial duration. The principle of the stretcher and the compressor is based on the optical devices dispersion which can control the optical dispersion – the time delay of different spectral components. Therefore, the limitation of the pulse intensity is related to its accessible duration. With CPA, the peak intensity can reach $10^{14}\mathrm{kW/cm^2}$, which corresponds to the same order of the electric field felt by an electron in an atom, with several femtosecond (fs, 10^{-15} s) few-cycle duration. Ultrafast dynamics and strong field physics are associated to each other.

To produce a pulse in attosecond (as, 10^{-18} s) time scale, which is the time scale for electron dynamics in atoms and molecules, higher frequency such as extreme ultraviolet (XUV) or X-ray is needed because this time scale is already shorter than the period of IR and visible light. However, the traditional way to produce an optical laser is unfeasible for the XUV or X-ray because of the lack of material for the mirror used in the resonant cavity to reflect the light at these frequency regime. One way to produce tabletop XUV laser is using the high harmonic generation (HHG) from the intense laser-atom interaction [3–11]. HHG is a strong field phenomenon in which the spectrum shows a plateau structure in the high frequency range when an atom or other material is illuminated by an intense laser field. The mechanism of HHG relies on the bremsstrahlung of the quantum tunneling ionized electrons recolliding with the parent ion [12, 13]. The cutoff energy of the emitted photon depends on the kinetic energy of electrons accelerated by the intense laser field, and the maximal kinetic energy of the returning electronic wave packet is $3.17U_p$, where ponderomotive energy $U_p = E_0^2/(4\omega_0^2)$ is the cycle-averaged quiver energy of the electron in the oscillating laser electric field with the field amplitude E_0 and the frequency ω_0. Therefore, XUV attosecond pulses can be generated from the plateau of atomic HHG and higher frequency can be obtained by using driving fields with higher intensity or lower frequency. The HHG is not only a high energy photon source but also a useful tool to study the material property due to the scattering between the returning wavepacket and the parent ion. For example, the rescattering process to each atom in a molecule can be treated as a interferometry, so the HHG radiation is also applied to reconstruct the valence orbitals and the molecular structures [14–16].

HHG is already widely used in the XUV or soft X-ray pulse generation. However, this kind of source suffers from low conversion efficiency. It was already shown that the

conversion efficiency decreases quickly as the laser wavelength is increased [17–22], and this wavelength scaling of the HHG yield limits the production of efficient X-ray sources. Compared with the HHG source, the availability of X-ray free electron lasers (XFEL) overcomes the limitation of pulse intensity and provides many different characterization from other light source. The first operation of a free electron laser (FEL) was in 1976 at Sanford University at a wavelength of $3.4\mu m$ based on the periodic arrangement of magnets to force an electron beam to wiggle transversely resulting in the release of photons [23]. The first soft X-ray free electron laser was developed in FLASH at DESY in Hamburg in 2005 with the photon energy ranging from range 10 eV to 200 eV. With the development of free-electron laser technologies. the limitation of pulse intensity and the wavelength tunability of the HHG source can be overcome. The high intensity property of XFELs enables non-linear optics, which was intensively studied in the optical domain, in the X-ray domain. This development leads to the study of non-linear X-ray spectroscopy such as stimulated Raman scattering [24] using the pulse that covers different transition frequencies. Moreover, a great advantage of the FEL is that it can be combined with an external highly coherent source of radiation, as called a seeded pulse to amplifies this external pulse [25–27]. This approach can be used to amplify the XUV pulse produced from HHG.

1.2 Ultrafast dynamics and time-resolved spectroscopy

Lasers are often used to study the structure of materials via laser transitions between different energy levels, and the related measurement, which is called spectroscopy, can be electromagnetic radiation such as absorption spectroscopy or emitted electrons in photoelectron spectroscopy. The static properties such as the ionization potential and the molecular structures can be determined. However, in static measurements, the signal only represents a particular final state of the system and there are many kind of dynamics missing in the measurement. For example, the electron can be triggered by the interaction with photons, phonons, or the electron correlation. In molecules or solids, the electron dynamics can also drive the motion of atoms, such as ionization-induced dissociation [29, 30]. To measure the real-time dynamics, pump-probe techniques, which relies on the combination of two laser pulses with varying time delay between them, is commonly used and the scheme is shown as Fig. 1.2. Mostly, processes are studied by shining a pump laser field to trigger the dynamic processes we are concerned

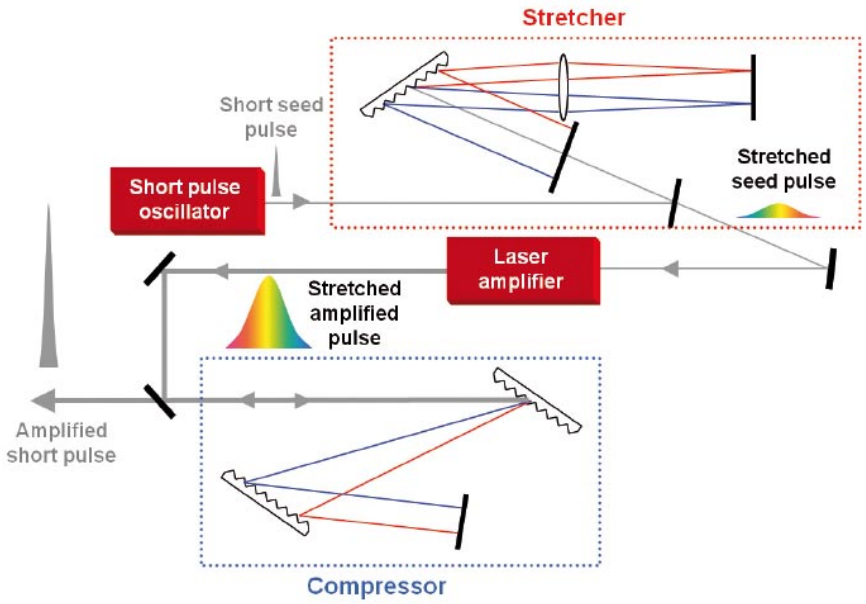

Figure 1.1: Schematic of chirped pulse amplification: After a generation of an ultrashort pulse, it is stretched by a stretcher. The stretched pulse is amplified, and then compressed to an extremely intense pulse with original duration. This figure is taken from [28]

.

about. Meanwhile, a delayed probe pulse is used to strike the sample again with the use of an optical delay line, which consists of a pair of mirrors to control the delay of the pulse. Finally, the desired signal, which can be emitted electron, ion, or photon, is measured by the detector. When varying the time delay between the pump and probe pulses, the variation of the signal encodes the information of the desired dynamics. The time resolution is determined by the pulse duration, and the femtosecond or attosecond pulses should be used to resolve the electronic or molecular dynamics.

In ultrafast regime, the spectroscopy based on the combination of a femtosecond IR laser field and phase-locked attosecond XUV pulses, which are generated from the same source, has found numerous applications. The IR pulses and the XUV pulses play different roles depending on the purposes. For example, in the IR-pump XUV-probe experiments, IR field can be used to breaking chemical bonds [31] or producing valence holes [32, 33]. At the same time, the XUV field acts as a probe to study electron-hole dynamics by transient absorption techniques [32–34]. In the XUV-pump IR-probe

experiments, the IR field can be used to map the temporal structure of the XUV-induced photoelectron to the frequency space by the attosecond streaking techniques [35–38]. The IR probe field is also applied to streak other kinds of emitted electrons such as Auger electrons to study the lifetime of the core hole produced by the XUV pulse [39].

With the capabilities of XFELs with the pulse duration in the femtosecond region [40, 41], the traditional pump-probe techniques has already been extended to the X-ray region. However, the FEL pulses arrival time with respect for an external locked IR laser has instability up to hundreds of femtoseconds [42], which can be comparable to or more than the duration of the pulse itself. The timing instability, or jitter, limits the temporal resolution of the time-resolved experiments using the FEL with an external laser source. To overcome the error due to arrival-time jitter, the synchronization of FEL pulses to optical lasers [43] or the additional measurement of the arrival time [44] is needed. The streaking techniques is extended to the ultrafast X-ray regime and the temporal structure of individual FEL pulses with 5 fs full-width at half-maximum (FWHM) accuracy is recently measured [44]. Furthermore, diverse femtosecond pump-probe schemes at FELs led to groundbreaking experiments in chemical-reaction dynamics [45–48]. Furthermore, the demonstration of XFEL pulse pairs with precisely controlled time delay, wavelength and intensity ratio were achieved at LCLS [49]. Because X-rays can provide site-specific excitation and trigger the inter-shell hole transfer, tunable XFEL pulse pairs could open new avenues for the new kinds of X-ray pump X-ray probe experiments [49–52] beyond the traditional time-resolved experiments with the use of optical lasers.

One of the important challenges of the real-time observation of ultrafast dynamics is to define the "time zero." During light-matter interaction, there is a response time of the production of the induced wavepacket to the occurrence of the event, such as the time delay between the photoionized electronic wavepacket to the photoabsorption event [54]. For example, recent experiments indicate that the photoelectrons resulting from different atomic initial states presents tens to hundreds time delay difference [38, 55],which is defined by the time difference between the two photoionization events compared to the driving laser pulse. The above experiments, which relies on XUV-IR attosecond streaking schemes, suffer from uncertainties on the order of tens of attoseconds [38, 55–59] and this uncertainty is non-negligible in the studies of attosecond science. The

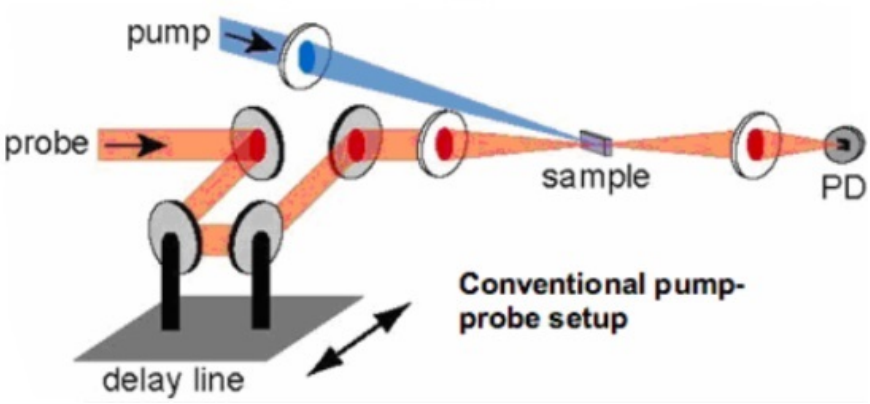

Figure 1.2: Schematic of conventional pump probe setup. A pump and a probe pulse is employed with a delay line consisting of a pair of mirrors to delay the probe pulse. This figure is taken from the Keith Nelson Group website @ MIT [53].

"timing" problem in attosecond science is originated to how the time delay between to an events is defined and how the probe field is used to take a measurement. The definition of different kinds of time delay relies on the quantum phase. For instance, the Wigner time delay is the time delay of the electronic wavepacket during the scattering process and defined with the energy derivative of the scattering phase [60, 61]; In the quantum tunneling, the time delay, often referred as tunneling time, is related to the complex ionization time of the quasiclassical trajectories derived from the phase used in strong field approximation (SFA) model [13, 62, 63]. When an additional field is added to the original system, there is an extra quantum phase so that the time delay also changes. How a probe field affects the time delay in the ultrafast dynamics and the possible scheme to avoid the unwanted measurement-induced time delay will be discussed in this thesis.

1.3 Theoretical approaches in ultrafast light-matter interaction

The most accurate way to describe the electron dynamics of light-matter interaction is to solve the exact time-dependent Schödinger equation. However, solving the full many-electron problem is rather unreachable and the different dynamical process

underlined the full ab-initio calculation are difficult to be analyzed. Some intuitive models and efficient time-dependent approaches should be implemented to extract the main physics from the complicated time-dependent many-electron wavefunction. The usual tragedy is to use single active electron (SAE) approach [64–66], in which only a valence electron is assumed to move in an effective potential V_{SFA}:

$$i\frac{\partial}{\partial t}\psi(\mathbf{r},t) = \left(-\frac{1}{2}\nabla^2 + V_{\mathrm{SFA}}(\mathbf{r}) + V_{\mathrm{ext}}(\mathbf{r},t)\right)\psi(\mathbf{r},t), \tag{1.1}$$

where $V_{\mathbf{ext}}$ is the time-dependent external potential and the physical observable properties can be obtained from the one particle wavefunction ψ. There are many successful models based on the SAE. For example, the Leweinstein's SFA approach used to describe intense laser-matter interaction such as HHG [13] and above-threshold ionization (ATI) [67]. However, there are several topics concerning many-electron or multi-channel effects which cannot be described in the SAE approach such as double ionization [68, 69], quantum exchange effect in the strong ionization of molecules[70], and the electronic hole dynamics during the ionization process [33, 71].

To describe the physics beyond SAE, there are several time-dependent approaches. One way to avoid many-electron wavefunction is using density functional theory (DFT). DFT is based on Hohenberg–Kohn theorems [72], stating that one-to-one correspondence between the ground electron density and a single-particle potential, and the Kohn–Sham equations [73]. The time dependent version of this theory is proposed and can be applied to the study of the excited-state properties [74, 75]. The advantages of time-dependent DFT (TDDFT) is its computational efficiency and it is especially powerful for solids because the electronic density only relies on 3 spatial variables rather than 3N spatial variables. However, TDDFT suffers from several drawbacks [76–80]. The formalism relies on different kinds of exchange-correlation functionals such that it is difficult to be systematically improved, and many of them induces large error in extended or weakly bounded system such as in molecular dissociation [76, 78]. In addition to density-based approaches, many-body-wavefunctions can also be treated by some wavefunction-based approaches such as configuration-interaction (CI), which is a post-Hartree–Fock method built from variational orbitals [81]. Hartree–Fock method is a variational approximation for a many-electron wavefunction using a single slater determinant. The ionization potential can be determined by Koopmans' theorem

[81, 82], which states that the energy difference between the singly-ionized states with a hole at orbital i and the Hartree-Fock ground state is equal to $-\epsilon_i$, the negative of the orbital energy. In contrast to the Hartree–Fock method, which is based on a single Slater determinant, the CI approach adapts a linear combination of more slater determinants

$$\Phi = \sum_{I=0} c_I \Phi_I, \tag{1.2}$$

in which Φ_0 is the Hartree-Fock ground state and Φ_I is the slater determinant by replacing I orbitals from c_0 with other virtual orbitals. The advantage of CI approach is that the correlation effect can be systematically included in addition to the Hartree-Fock ($I = 0$). For example, $I = 1$ represents CI singles (CIS) states, which are singly excited determinants generated by replacing one of the orbitals from the Hartree-Fock ground state with a virtual orbital. The advantage of CI singles (CIS) is that it is a size-consistent approach, which means the energy of two infinitely separated particles is the double of the energy of two infinitely separated particles. This implies correct dissociation into fragments for molecular system [84]. Therefore, its time dependent version, time-dependent CIS (TDCIS), is a good choice for studying finite atomic and molecular systems interacting with light. TDCIS has recently been applied to laser-induced excitation of a polyatomic molecule [85, 86] as well as the strong-field ionization and HHG of an atom [83, 87–89].

Besides the many-body formalism of the electron dynamics, the other challenge is the description of the ionized wavepacket. The wavefunction can represented in both the momentum and the real space. The momentum representation is more directly linked to the photoelectron spectrum, but the representation of the electric dipole interaction becomes a non-diagonal matrix, which causes the time propagation time–consuming. Instead, the real space representation is often used in finite-systems and the computational box can be split into two parts: an inner part including all atomic nucleus and an outer part only containing the ionized wavepacket which never comes back to nucleus. However, the ionized wavepacket suffers from the boundary condition of the computational box. Therefore, a new numerical method time-dependent surface flux method (t-SURFF) was proposed, that treats the outgoing electronic wavepacket as a flux through the surface which separates the inner and the outer regions [90–93]. This method is widely applied to many time-dependent formalisms, including multi-channel TDCIS formalism [94, 95].

1.4 Outline

This thesis focuses on the hole dynamics triggered by the XUV/X-ray pulses in combination with strong optical laser or other XUV/X-Ray pulses. We present a theoretical studies on how to model and numerically calculate the desired strong-field phenomena and the perturbative photoabsorption process. There are two proposed time-resolved spectroscopies: XUV-assisted HHG [96], in which an additional XUV pulse is applied to drive the hole transition during the HHG process, and Stimulation of Two Resonant and Instantaneously Detuned Electron Replicas (STRIDER) [95], which relies on a pair of XUV pulses detuned from core-valence hole transition to characterize attosecond pulses. These works would be realizable with the current source technology. Our goal is to study the electron dynamics involving the core-valence transitions as well as the bound-free transitions in attosecond time scale. In this thesis, every equation is written in terms of atomic units: electron mass m_e, elementary charge e, Reduced Plank's constant $\hbar$, and Coulomb's constant $k_e = 1/(4\pi\epsilon_0)$ are set to be 1.

Chapter 2 introduces the basic concepts about light-atom interaction. The photoionization effect and the time-dependent perturbation theory for the photoelectric effect are described. The perturbation theory is used to explain the phenomena of the second and the third harmonics in nonlinear optics. Then we explain the strong field phenomena such as high-harmonic generation and why the perturbation theory fails. The concept of tunneling ionization and a more suitable theoretical model, three step model, is introduced to describe the physics in the strong field regime. Several methods to generated attosecond pulses via High-harmonic generation are presented. Finally, we introduce on how to characterize these pulses using IR-streaking photoelectrons and the related "atomic response time" induced by light-atom interactions in 2.4.

Chapter 3 introduces the theoretical methods used in the following projects. In section 3.1, the strong field approximation for HHG and the mathematical form for a 1D system is mentioned. In section 3.2, the time-dependent configuration interaction singles (TDCIS) method – an ab-initio electronic structure technique– is formulated for studying strong-field phenomena in many-electron systems. In section 3.3, the time-dependent surface flux (t-SURFF) is introduced to efficiently calculate a photo electron spectrum. The combination of TDCIS and t-SURFF with the consideration of channel-coupling is proposed, and the significance of the channel-coupling is discussed.

Chapter 4 presents a theoretical study of the XUV-assisted HHG. Using resonant

XUV pulses in addition to the intense driving field, a second plateau beyond the original HHG cutoff is generated. The extended semiclassical SFA model, which includes two bound states and resonant XUV pulses, is derived and used to explain this second plateau. The calculation results from the TDCIS scheme and the extended SFA model are compared. The concept and the effect of the resonant XUV excitation during the quantum tunneling process are used to explained the interference pattern from the SFA calculation. In the case of the IR driving field + XUV pulse train, the coherent accumulation of occupation in the inner shell hole is discussed.

Chapter 5 presents a theoretical study of a new approach for attosecond pulse characterization using two coherent extreme ultraviolet or x-ray probe fields, which are tuned to a core-valence transition in the residual ion and induce spectral shearing of the photoelectron distributions. The interference pattern of the photoelectron-ion coincidence signal is shown to depend on the spectral phase of the attosecond pulse. The combination of TDCIS and t-SURFF is used to calculate the photoelectron spectrum in the case of both single pulse and pulse train. We discuss the error of the characterization originating from "atomic response times." In the end, we discuss the difference between the use of the inner-core hole and the outer-core hole as the core-valence transition.

Chapter 6 gives the summary of these theoretical works. Future possible topics and possible experimental setups are proposed.

Chapter 2

Light-atom interaction

Electron excitation and ionization as well as the light absorption and emission under the influence of ultrashort lasers are the key points of attosecond physics. The study of light-matter interaction at the microscopic level can be traced back to the spectroscopy of Hydrogen atom and the photoelectric effect in the early history of quantum mechanics. Until now, most of the explanation of light-matter interaction process is based on perturbation theory. With the development of laser technology, the laser intensity can reach the regime in which the perturbation theory becomes invalid. In this chapter, we will discuss the main mechanism of light-atom interaction, related phenomena and current obstacles in the theoretical descriptions of those processes.

2.1 Photoelectric effect and photoionization

The photoelectric effect is the phenomenon that electrons escape from metals when a light shines on the metal surface. Photoionization is the same process but with more regard to finite systems such as atoms and molecules. This process was explained by Einstein using the concept of photon and the energy conservation – the energy of the emitted electron is equal to difference between the photon energy and the ionization potential. From the photoionization spectrum, one can directly measure the static information such as binding energies of electrons as well as the light's frequency. With the use of two laser pulses, referred to as a pump and a probe pulse, the photoelectron spectrum as a function of time delay between two pulses encodes the dynamical information. The spectral yields are described in terms of probability amplitudes from

the time-dependent Schrödinger equation with the Hamiltonian

$$H(r,t) = [H_0(r) + V(r,t)] = H_0(r) - zE(t), \tag{2.1}$$

where $H_0(r)$ is the field-free Hamiltonian with eigen states $|\, v \,\rangle$ and eigen energies ϵ_v, and $V(r,t)$ is the time-dependent laser-matter interaction in which the dipole approximation in the length gauge is used. The wavefunction in the interaction picture and the time evolution operator can be expanded as

$$|\, \Psi, t_0; t \,\rangle_I = \sum_v c_v(t) |\, v \,\rangle. \tag{2.2}$$

and the time evolution operator in interaction picture notation

$$U_I(t,t_0) = 1 + \frac{1}{i}\int_{t_0}^{t} dt' V_I(t') U_I(t',t_0), \tag{2.3}$$

where the index I represents the representation of interaction picture. Assuming the electron is in the eigenstate i at the beginning, then the initial condition is $c_v(t_0) = \delta_{vi}$. In the perturbation theory, the transition amplitudes can be approximated by perturbation expansion $c_v(t) = c_v^{(0)} + c_v^{(1)} + c_v^{(2)} + \cdots$, and the nth-order perturbation amplitude can be expressed recursively

$$c_v^{(n)}(t) = \frac{1}{i}\sum_{\xi}\int_{t_0}^{t} dt' \langle\, v \,|\, V(t') \,|\, \xi \,\rangle \exp[i\omega_{v\xi}t'] c_\xi^{(n-1)}(t'), \tag{2.4}$$

with $c_v^{(0)}(t) = \delta_{vi}$. The first order perturbation amplitude for excitation from i to v by the external field is given by

$$\begin{aligned} c_v^{(1)}(t) &= -\frac{z_{vi}}{i}\int_{t_0}^{t} dt' \int_{-\infty}^{\infty} d\omega \frac{\tilde{E}(\omega)}{2\pi} \exp[-i\omega t'] \exp[i\omega_{vi}t'] \\ &= -\frac{z_{vi}}{i}\int_{-\infty}^{\infty} d\omega \frac{\tilde{E}(\omega)}{2\pi}\left[\frac{e^{i(\omega_{vi}-\omega+i\eta)t}}{i(\omega_{vi}-\omega+i\eta)} + 2\pi\delta(\omega_{vi}-\omega)\right], \end{aligned} \tag{2.5}$$

where $\eta \to 0^+$ is implied due to the slow turn-on of the laser pulse. Here the electric field is assumed to be linearly polarized along the z-axis and the light-matter interaction is treated in the electric dipole approximation in length gauge $V(t) = E(t)z$, in which

$E(t)$ can be represented in the frequency domain

$$E(t) = \int d\omega \tilde{E}(\omega) \exp[-i\omega t]. \tag{2.6}$$

Assuming the interaction starts at $t_0 = -\infty$ and ends at $t = \infty$, the relation for the delta function enforces energy conservation $\omega_{vi} = \epsilon_v - \epsilon_i = \omega$, which recovers Einstein's photoelectric effect if the state v is a continuum state. Although laser fields here are treated as classical fields, the energy conservation reveals the energy quantum of the electromagnetic field. The final complex amplitude in the first order approximation is given by

$$S_v^{(1)} = \lim_{t\to\infty} c_v^{(1)}(t) = -\frac{1}{i} z_{vi} \tilde{E}(\omega_{vi}) \tag{2.7}$$

and its absolute value square represents the photoelectron spectrum for the one-photon process. The transition amplitude copies the spectral structure of the laser field with the prefactor proportional to z_{vi}, so that the photoelectron wavepacket can be considered as the replica of the corresponding laser pulse. If the transition we consider is below the ionization threshold, the transition is only allowed when the frequency domain of the electric field covers the transition energy ω_{vi}. From the experimental perspective, many spectroscopic techniques are based on the photoelectric effect because the photoelectron wavepacket carries both laser field spectral information and the energy levels of the matter.

2.2 High-Harmonic generation

With the invention of the laser, harmonic generation has been studied since 1960s in the perturbative multiphoton regime. In 1961, second harmonic generation, as an even-order nonlinear optical effect which is only allowed in media without inversion symmetry, was demonstrated in a crystalline quartz sample [97]. In 1967, third harmonic generation was observed in rare gases, in which the even-order effect is forbidden due to inversion symmetry [98]. The conversion efficiency decreases rapidly compared with increasing harmonic order and is well understood with perturbation theory. The power of emitted radiation is related to its dipole response in Larmor formula

$$S(\Omega) = \frac{D_a^2(\Omega)}{2c^3} = \frac{D^2(\Omega)\Omega^4}{2c^3}. \tag{2.8}$$

Here $D_a(\Omega)$ is the dipole acceleration and $D(\Omega)$ is the dipole moment in frequency domain. In microscopic perspective, the time-dependent dipole moment is nothing but the expectation value of the electric dipole moment operator over the wavefunction

$$\begin{aligned} D(\Omega) &= \int_{-\infty}^{+\infty} dt \langle\, \Phi_I(t) \,|\, z_I \,|\, \Phi_I(t) \,\rangle \exp(i\Omega t) \\ &= \int_{-\infty}^{+\infty} dt \sum_{v_m, v_n} \sum_{m,n} c_{v_m}^{(m)*}(t) c_{v_n}^{(n)}(t) z_{v_m v_n} \exp[i(\omega_{v_m v_n} + \Omega)t], \end{aligned} \tag{2.9}$$

where v_m and v_n run over all eigenstates of the system. Each individual term corresponds to n-photon absorption and m-photon emission process. Assuming the driving laser field is a weak monochromatic field $E(t) = E_0 \cos \omega t$ and there is no resonant transition, then the n-photon absorption from the ground state, denoted by g, corresponds to the coefficient

$$\begin{aligned} c_{v_n}^{(n)}(t) &= \left(-\frac{1}{i}\right)^n \sum_{v_{n-1} \cdots v_1} \int_{t_0}^{t} dt_n \cdots \int_{t_0}^{t_2} dt_1 z_{v_n v_{n-1}} z_{v_{n-1} v_{n-2}} \cdots z_{v_1 g} (\frac{E_0}{2})^n \\ &\quad \times \exp[i((\omega_{v_n v_{n-1}} - \omega)t_n + (\omega_{v_{n-1} v_{n-2}} - \omega)t_{n-1} + \cdots + (\omega_{v_1 g} - \omega)t_1)] \\ &= \sum_{v_{n-1} \cdots v_1} \left(-\frac{E_0}{2i}\right)^n \frac{z_{v_n v_{n-1}} z_{v_{n-1} v_{n-2}} \cdots z_{v_1 g}}{(\omega_{v_n v_{n-1}} - \omega)(\omega_{v_{n-1} v_{n-2}} - \omega) \cdots (\omega_{v_1 g} - \omega)} \exp[i(\omega_{v_n g} - n\omega)t]. \end{aligned} \tag{2.10}$$

The dipole response of this n-photon absorption and single-photon emission process is

$$D(\Omega) = \int_{-\infty}^{+\infty} dt \sum_{v_n} c_g^{(0)*}(t) z_{g v_n} c_{v_n}^{(n)}(t) \exp[i(-\omega_{v_n g} + \Omega)t] = C_n (E_0)^n \delta(\Omega - n\omega), \tag{2.11}$$

where C_n is a constant depending on the structure of the system. The energy of the emitted photon is equal to the energy of the total photons absorbed. In macroscopic perspective, when there are lights with frequency $\omega_1, \omega_2, ...$ launched into a nonlinear sample, the dielectric polarization in terms of the electrical field can be written as

$$P(\Omega) = \chi^{(1)}(\omega_i) E_i(\omega_i) + \chi^{(2)}(\omega_i, \omega_j) E_i(\omega_i) E_j(\omega_j) + \chi^{(3)}(\omega_i, \omega_j, \omega_k) E_i(\omega_i) E_j(\omega_j) E_k(\omega_k) \cdots. \tag{2.12}$$

Here, the coefficients $\chi^{(n)}(\omega_{i_1}, ..., \omega_{i_n})$ are the nth-order nonlinear susceptibilities of the medium with energy conservation $\Omega = \omega_{i_1} + ... \omega_{i_n}$. If the eigenstates of the system can be categorized into odd parities and even parities, such as a single atom, the even

order harmonics disappears because of selection rules.

In the late 1980s, the HHG spectrum consisting of plateau structure in the high harmonic order was observed in rare gas with high intense driving laser field (10^{13} – 10^{16}W/cm^2) [99, 100]. The perturbation theory, which predicts the harmonic yields exponentially falling off, is not sufficient to describe this behavior. The first successful model to understand the HHG process, together with other strong field phenomena such as above-threshold ionization, is the simple-man model, or the so called three step model [101, 12]. In this model, the intense electric laser field is treated as classical field and can distort the atomic potential as shown in Fig. 2.1 (a). First, the valence electron has the possibility to tunneling ionize to the continuum at time t_i. The ionization rate is given by the DC tunneling rate

$$W_{dc} = C(I_p, E_0) \exp\left[-\frac{4\sqrt{2} I_p^{\frac{3}{2}}}{3E_0} \right], \tag{2.13}$$

which is the quasistatic limit ($\omega \to 0$) of the AC tunneling rate predicted by Keldysh [62]. Here $C(I_p, E_0)$ is a system-dependent coefficient which has a polynomial dependence on the ionization potential I_p and the electric field amplitude. Second, the electron moving in the continuum is accelerated by the electric laser field so that it will directly fly away or recollide to the parent ion at time t_r. Finally, the electron may rescatter again, transferring the energy to other bound-state electrons, or recombining to the ground state by emission of a photon. By assuming an electron with the initial position of the outer tunnel point of the distorted potential and velocity equal to zero, the recollision occurs when the electron comes back to the initial position

$$\Delta z = \int_{t_i}^{t_r} (A(t) - A(t_i)) dt = 0, \tag{2.14}$$

where the $A(t)$ is the vector potential of the electric laser field. The energy of the emitted photon E_p during the recombination process follows the energy conservation

$$E_p = E_r + I_p = \frac{1}{2}[A(t_r) - A(t_i)]^2 + I_p, \tag{2.15}$$

where E_r is the returning kinetic energy of the electron. By assuming the electric field $E(t) = E_0 \cos \omega t$ and solving Eq. 2.14 and 2.15, we can obtain the one-to-one mapping between recollision time and ionization time in one optical cycle as shown in Fig. 2.1

(c), and the returning kinetic energy as the function of t_r or t_i as shown in Fig. 2.1 (b). The maximal energy of the emitted photon and is predicted by [12, 102]

$$E_{\text{cutoff}} = I_p + 3.17U_p, \tag{2.16}$$

where $U_p = E^2/(4\omega^2)$ is the Ponderomotive potential, which is defined as the cycle-averaged quiver energy of a free electron in the monochromatic laser field. Most of the HHG trajectories give similar ionization rates because all of them are born around the peak of the laser field. For the recollision energy below the maximum, there are two trajectories along which the electron can acquire the same energy by the time it returns to the parent ion. These two sets of trajectories are called long trajectories with ionization time earlier than $t_{i,\text{cut}}$ and recollision time later then $t_{r,\text{cut}}$, and short trajectories, which is contrary to long trajectories. The trajectories with duration longer than one optical cycle are negligible because of the diffusion of the electron wavepacket. It is worth noting that the ionization time of the trajectories with high returning energy are focused on the region close to the peak amplitude of the laser field as indicated with the blue dashed line ($0 < t_i/T_{\text{laser}} < 0.1$) in Fig. 2.1 (b) and (c). In addition, the HHG process has the duration less than one optical cycle and iterates for each half optical cycle. This periodic repetition of the HHG process together with the inversion symmetry of atomic gases results in an odd-order harmonic. The study of the classical trajectory provides us some ideas to manipulate the HHG process. For example, adding an additional field with different frequency in combination with the driving laser field can alter the semi-classical electron trajectories in the continuum so that the cutoff energy can be extended [103–105]. In conclusion, the simple-man model gives us an intuitive physical picture about the generation of high harmonics and results in a good prediction to the cutoff energy. To study a quantum phase and interference such as the phase of HHG radiation, the quantum mechanical approach is needed and will discussed in the next chapter.

From Eq. 2.16, it is clear that the higher harmonics order or the higher emitted photon energy can be achieved by using longer wavelength, higher field intensity, or larger atomic potential. With the use of high intensity laser fields, the harmonic spectrum has been extended to the water window, which is important for bio- and nano-imaging [106, 107]. However, most of the applications are still focused in the XUV range rather than soft X-ray range due to the limited flux [108]. To get brighter the

high energy photon, the emitted radiation from different atoms must be added in the phase. In addition to the microscopic dipole phase, the control of the phase-matching condition includes the dispersion of both neutral and ionized medium, focusing geometry [109–111]. In recent experiments, the IR laser at wavelengths up to $2-4\mu m$ has been used to generate brighter soft x-ray in the water window [108] and even higher energy around 1.6 keV [112] with more than a 5000 harmonic order.

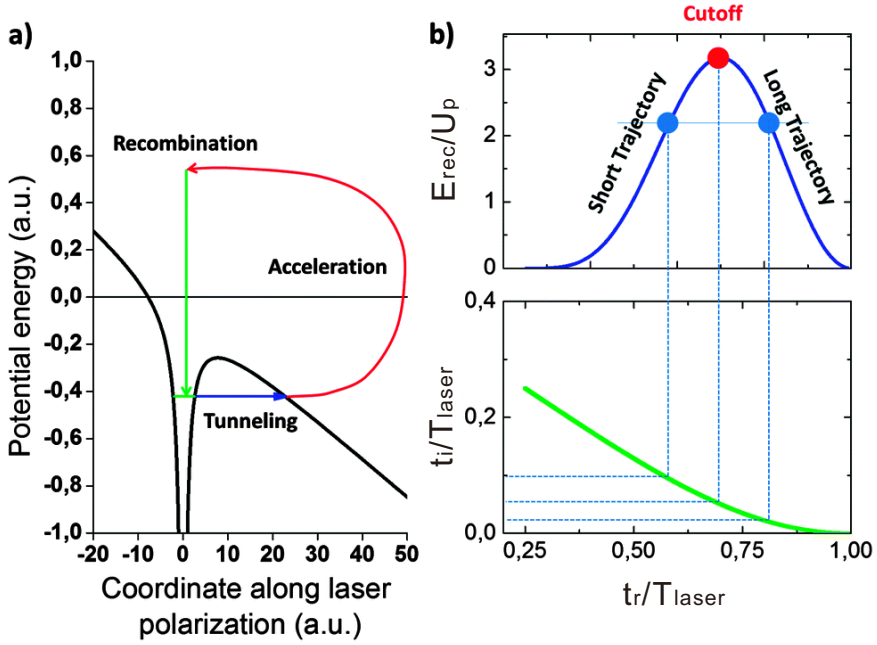

Figure 2.1: (a) Schematic of three-step model of HHG process: tunneling ionization, acceleration and recombination. (b) Returning kinetic energy as the function of recollision time. (c) The one-to one map between the ionization time and the recollision time. This figure is taken from [113]

2.3 Attosecond pulse generation

The broadband property of the plateau of the HHG spectra can be used to generate attoseond pulses. This schematic was first realized in 2001 [3] and a train of 250-attosecond pulses extending over 10 fs was observed. Because the HHG process with the use of multicycle driving fields is repetitive in the time domain, a train of pulses with only one pulse per half-cycle rather than a single pulse is generated as shown

in Fig. 2.2. In addition, atomic HHG spectra contain only odd harmonics in the spectral domain, hence the carrier envelope phase between adjacent pulses has π phase difference. With the production of attosecond pulse train (APT), some attosecond time-resolved measurements within the time window of the half optical cycle can be achieved so that the related ultrafast dynamics can be studied. However, to get the more straightforward interpretation of ultrafast measurements, isolated attosecond pulses are needed.

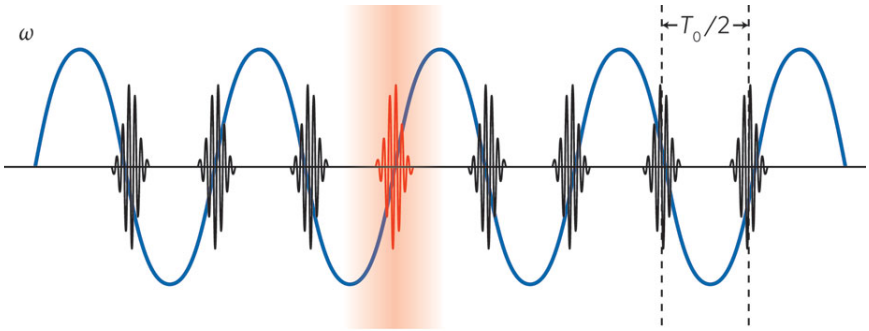

Figure 2.2: An attosecond pulse train is generated from HHG by a multicycle driving IR field. A single pulse can be obtained from the pulse train by different gating techniques. This figure is taken from [9].

Because the generation of APT is based on the periodicity of the HHG process, the key idea that produces a single attosecond pulse (SAP) is to destroy this periodicity. The first single pulse via HHG was generated by the few cycle IR field and an isolated XUV pulse of 90 eV with duration of 2.7 fs has obtained [4]. With the use of few cycle driving fields, each half cycle represents unique spectral properties and a SAP can be extracted by spectral filtering from the cut-off region of the HHG spectrum. Pulses of central photon energy of 80 eV with duration as short as 80 as have been produced in neon using this spectral gating techniques [114]. There are also several generation methods based on temporal gating schemes. For example, modulating the polarization of the driving field such that the field is only linearly polarized in some short time duration and elliptically polarized in the reminder of the duration [5, 6]. This kind of method, which is also called polarization gating, only allows the XUV photons generated from that short time duration because the conversion efficiency of HHG decreases rapidly with increasing ellipticity. With the use of an additional

linear polarized second harmonics field, a high harmonic burst can occur only once a cycle so that the duration requirement of the polarization gate can be relaxed. Using this two-color field scheme together with the polarization gating, a SAP with central photon energy of 100 eV and a duration of 67 as can be achieved [10]. Compared with APT, SAP can give more intuitive pictures to the attosecond dynamics in the time domain. In the spectral domain, SAPs have broad spectral bandwidths such that a great number of excitation energies can be covered while APTs can be used for exciting more selective states or specific resonances.

Because the emitted photons of different frequency are generated at different times, the pulse generated from HHG is not Fourier-limited and presents a time-dependent frequency, or "'chirp'. For example, the HHG spectra using the double optical gating technique are capable of supporting a 16 as Fourier-limited pulse while the measurement showed a 107 as pulse duration [115]. In addition, a pulse propagating in the medium can also be stretched or compressed. All of these effects are represented in the spectral phase $\delta(\omega)$

$$E(t) = \int d\omega |\tilde{E}(\omega)| \exp[-i\omega t + i\delta(\omega)]. \tag{2.17}$$

The group delay defined as

$$\tau_{\mathrm{GD}}(\omega) = \frac{d\delta(\omega)}{d\omega} \tag{2.18}$$

can be related to the time when the coherent superposition of all wave packets in the neighborhood of ω is constructive. For example, we consider an attosecond pulse centered at frequency ω_0 with a Gaussian envelope

$$|\tilde{E}(\omega)| = E_0 \exp[-g(\omega - \omega_0)^2] \tag{2.19}$$

and the spectral phase $\delta(\omega) = \delta_0 + t_0(\omega - \omega_0) + \alpha(\omega - \omega_0)^2$ up to the second order. To deal with Eq. 2.17 with stationary phase approximation, both of the shape and the phase effects should be taken into consideration. We can obtain a complex stationary frequency

$$\omega_s(t) = \omega_0 + \frac{\alpha - ig}{2(\alpha^2 + g^2)}(t - t_0) \tag{2.20}$$

and the electric field in time domain reads

$$E(t) = \frac{E_0}{2\pi}\sqrt{\frac{\pi}{\beta}} \exp\left\{ -i\left[(-\delta_0 + \omega_0 t_0) + \omega_0(t - t_0) + \frac{\alpha(t - t_0)^2}{4(g^2 + \alpha^2)}\right] - \frac{g(t - t_0)^2}{4(g^2 + \alpha^2)}\right\}, \tag{2.21}$$

where $\beta = \alpha - ig$. After the Fourier transform, it is obvious that the zeroth order of the phase contributes to a pure phase shift and the linear phase induces time shift t_0 in the time domain. Compared with Fourier-limit pulses, the quadratic phase stretches the pulse with the stationary frequency change linearly in time. The real part of $\omega_s(t)$ is equal to the instantaneous temporal frequency

$$\mathrm{Re}(\omega_s(t)) = -\frac{\partial \arg(E(t))}{\partial t} = \omega_0 + \frac{\alpha}{2(g^2+\alpha^2)}t \tag{2.22}$$

and the imaginary part of $\omega_s(t)$ implies the duration of the pulse. In Fig. 2.3 (a), a Fourier-limited pulse with central frequency 68 eV and bandwidth 7.5 eV, and the stretched pulse with quadratic phase $\alpha = 25$ are shown. The dominant frequencies of these two pulse as a function of time are shown in Fig. 2.3 (b). Therefore, from the spectral domain point of view, the phase information as well as amplitude information of broadband pulses, such as APs, is important.

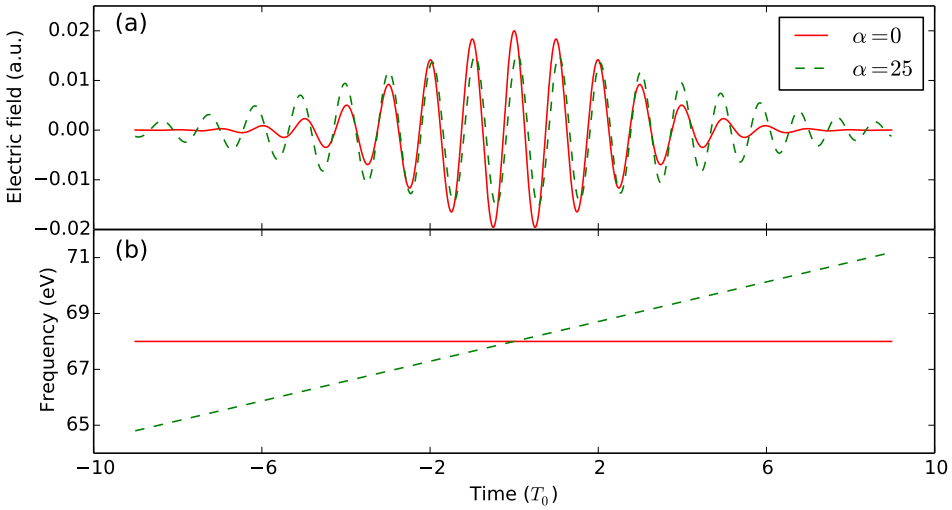

Figure 2.3: A Fourier limited pulse and a stretched pulse with quadratic phase $\phi(\omega) = \alpha(\omega-\omega_0)^2$ with $\alpha = 25$: (a) The electric fields $E(t)$ in time domain; (b) The dominant frequency as the function of time $\mathrm{Re}(\omega_s(t))$.

2.4 Pulse characterization and atomic Response time

Not only generating but also characterizing a broadband attosecond pulse is challenging. Autocorrelation or crosscorrelation methods in the optical domain using nonlinear optical effects are widely used for femtosecond pulses. However, these kinds of method cannot be straight-forwardly extended to attoseconnd time domain due to both the lack of effective nonlinear materials in the XUV spectral region and the low photon flux of attosecond pulses. Instead, attosecond spectroscopy methods such as attosecond streaking rely on a set of photoelectron spectra over a range of time delay between the XUV pulse, which ionizes the electron, and the streaking IR field, which interacts with the photoelectron [36]. In Fig. 2.4 (a), the basic principle of streaking method is illustrated. The photoelectron wavepacket can be treated as the replica of the XUV field. Assuming the vector potential $A(t)$ at the end of the IR field is zero, the field can transfer additional momentum $\Delta p(t)$ to the photoelectron which is equal to $A(t)$ at the time t when the electron ionizes. The duration of the XUV pulse has to be shorter than the half period of the IR pulse in order to map the transfer of momentum $\Delta p(t) = A(t)$ one-to-one to the time t. Therefore, the distortion of the spectra depends on both time delay and the temporal character of the ionized wavepacket. In the experiment, the streaking field should be strong enough to significantly accelerate photoelectrons, while it should be weak enough to avoid the distortion of the atomic structure.

We can also understand the XUV+IR scheme in the frequency domain as shown in Fig. 2.4 (b). There are different interference pathways leading to the energy ϵ_k in the spectrum. The dominant contribution is from the path (d), which is contributed from the lowest order perturbation and corresponds to the absorption of a single XUV photon with energy Ω. Furthermore, the same energy can be reached by absorbing a less energetic photon $\Omega_<$ and an additional IR photon ω, indicated as path (a) ; or the path (e) — the combination of absorbing higher energetic photon and emitting ω. The interference between these three pathways as a function of the XUV-IR delay can be used to reconstruct the spectral phase of the attosecond pulse by the algorithm called Phase-Retrieval by Omega Oscillation Filtering (PROOF)[116]. Because this interpretation relies on an additional IR photon absorption or emission, the IR field should be weak enough to be treated as a perturbation.

The same idea can also be applied to the attosecond pulse train characterization, such as Reconstruction of Attosecond Beating By Interference of Two-photons transitions

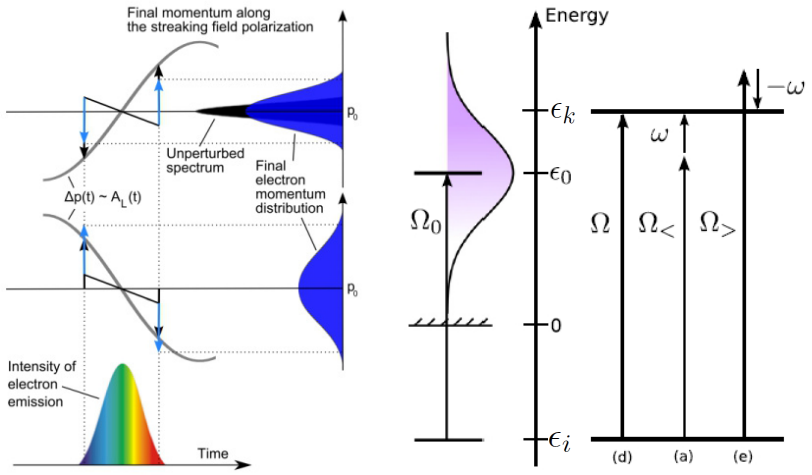

Figure 2.4: (color online) The sketch of streaking for a photoelectron ionized by a single attosecond pulse and probed by a monochromatic laser field in time domain (a) and frequency domain (b). (a) The IR field transfer can transfer additional momentum $\delta p(t) = -A(t)$ at the ionization time t of the electron. The distorted spectrum depends on both the time delay and the temporal structure of the unstreaked photoelectron wavepacket. This figure is taken from [117]. (b) In addition to the pathway by the one-photon absorption to reach the energy Ω, the photoelectron can reach the same energy by absorbing an the absorption or the emission of an additional IR photon with frequency ω: $\Omega = \Omega_< + \omega$ and $\Omega = \Omega_> - \omega$. This figure is taken from [57].

(RABITT) as illustrated in Fig. 2.5. The attosecond pulse train generated from the atomic HHG process contains only odd harmonics, which results in the Comb structure in the photoelectron spectrum. If a weak periodic probe IR field with the fundamental frequency is applied, the additional IR photo absorption and emission by the free electron wavepacket results in the side peaks corresponding to the frequency of even harmonics, as the dashed lines shown in Fig. 2.5 (b). A typical experimental RABITT spectrum is displayed in Fig. 2.5 (a). The side peaks show a modulation as the function of APT-laser delay due to the interference between the pathways of IR photo-absorption and -emission.

The XUV-IR streaking techniques can be explained by the second order perturbation theory. The electric laser field is written as $E(t) = E_1(t) + E_2(t)$, where E_1 is the XUV field with central frequency Ω_0 larger than the ionization potential $I_p = -\epsilon_i$ and E_2 is

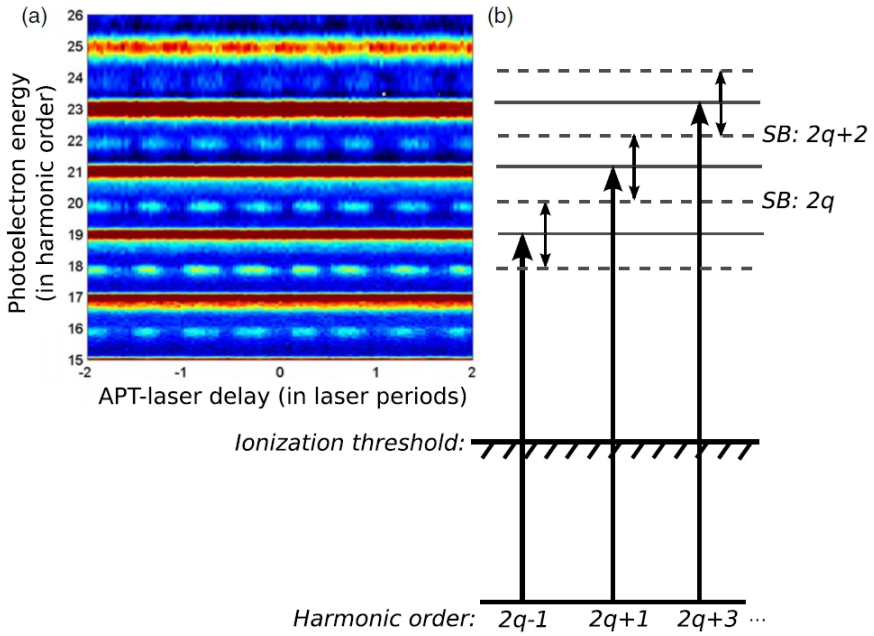

Figure 2.5: RABITT method. (a) Photoelectron spectrogram over photon energy and delay between the APT and the IR field. The offset in the modulation of the sidebands contains information about the attosecond pulses and the ionization process. (b) Schematic energy diagram over the quantum paths leading to the same final energy in SB 2q. This figure is taken from [57].

the IR field. The time-dependent two-photon transition amplitude to the continuum state with momentum k is

$$c_k^{(2)}(t) = \left(\frac{-1}{i}\right)^2 \int_{-\infty}^{t} dt_2 \int_{-\infty}^{t_2} dt_1 \int d\kappa z_{k\kappa} z_{\kappa i} E_2(t_2) E_1(t_1) \exp[i(\omega_{k\kappa} t_2 + \omega_{\kappa i} t_1)] \quad (2.23)$$

for the time-ordered process, in which the electron interacts with E_1 first and then E_2 later. The final two-photon transition amplitude is

$$\begin{aligned} S_k^{(2)} &= \lim_{t\to\infty} c_k^{(2)}(t) \\ &= \frac{1}{i} \int d\Omega \tilde{E}_2(\omega_{ki} - \Omega) \tilde{E}_1(\Omega) M(k, \Omega), \end{aligned} \quad (2.24)$$

where

$$M(k,\Omega) = \int d\kappa \frac{z_{k\kappa} z_{\kappa i}}{\omega_{\kappa i} - \Omega} \tag{2.25}$$

is the two-photon matrix element. Eq. 2.24 indicates that the two-photon transition process is nothing but the convolution integration resulting from energy conservation. In addition to the laser field, the two-photon matrix element M also contributes the phase to the two-photon transition amplitude. For example, in an atomic system, the momentum state wavefunction $\psi_{\hat{k}}(\hat{r})$ can be expanded in partial waves [57, 59, 118, 119]

$$\Psi_{\hat{k}}(\hat{r}) \propto \sum_{L,M} i^L e^{-i\eta_L(k)} Y^*_{L,M}(\hat{k}) Y_{L,M}(\hat{r}) R_{k,L}(r), \tag{2.26}$$

where $\eta_L(k)$ are angular-momentum dependent scattering phases of the real radial functions $R_{k,L}(r)$. The transition amplitude is the combination of different angular-momentum channels $l_i \to l_\kappa \to l_k$

$$M(k,\Omega) = \sum_{l_\kappa, l_k} M_{l_\kappa, l_k}(k,\Omega) \tag{2.27}$$

and the phase of the partial transition amplitude is [57, 59]

$$\mathrm{Arg}(M_{l_\kappa,l_k}(k,\Omega)) = \pi + \mathrm{Arg}[Y_{l_k,m_i}(k)] - \frac{\pi l_\kappa}{2} + \eta_{l_\kappa}(\kappa) + \phi_{cc}(k,\kappa). \tag{2.28}$$

Here $-\pi l_\kappa/2 + \eta_{l_\kappa}(\kappa)$ is the phase shift between the partial scattering wave of the intermediate state and the partial plane wave, and $\phi_{cc}(k,k')$ describes the continuum-continuum transition in the presence of the long-range Coulomb potential. For a hydrogen-like atom with potential which is exactly $-Z/r$, there are analytical solutions of the real radial functions $R_{k,L}(r)$ and the phases of the partial transition amplitudes can be computed directly. For other kinds of potential, such as Hartree-Fock potentials for many-electron atoms, a numerical calculation should be performed and suffers from the accurate description of the asymptotic behavior of the scattering wavefunction. The method called exterior complex scaling, which transforms the radial coordinates at large distance into the complex plane, can enforce the outgoing wave functions exponentially decay so that the real-space numerical calculation is applicable.

In the attosecond streaking techniques, the probe field is assumed to be a monochromatic IR field $E_2(t) = 2|\tilde{E}_{2,\omega}|\cos(\omega(t-\tau))$ with time delay τ and $\tilde{E}_{2,\omega} = |\tilde{E}_{2,\omega}|\exp[i\omega\tau]$,

so the convolution integration in Eq. 2.24 can be reduced to the sum of two pathways indicated in Fig. 2.4: $S_k^{(a)} = \tilde{E}_{2,\omega}\tilde{E}_1(\Omega_<)M(k,\Omega_<)$ with $\Omega_< = \omega_{ki} - \omega$ and $S_k^{(e)} = \tilde{E}_{2,\omega}^*\tilde{E}_1(\Omega_>)M(k,\Omega_>)$ with $\Omega_> = \omega_{ki} + \omega$. In the case of the RABBIT scheme, the pump field $\tilde{E}_1(\Omega) = \sum_q \tilde{E}_{1,2q+1}\delta(\Omega - (2q+1)\omega)$ is the pulse train consisting of a comb of odd high-order harmonics with $|\tilde{E}_{1,2q+1}| = \tilde{E}_{1,2q+1}\exp[i\phi_{2q+1}]$, then the side peaks predicted by the perturbation theory is located at $\epsilon_k = 2q\omega + \epsilon_i$. Assuming the total contribution of the transition amplitude is dominated by single angular-momentum channel, then the interference term can be written as

$$\begin{aligned}\mathrm{Arg}(S_k^{(a)*}S_k^{(e)}) &= -2\omega\tau + \phi_{2q+1} - \phi_{2q-1} + \eta_\lambda(\kappa_>) - \eta_\lambda(\kappa_<) + \phi_{cc}(k,\kappa_>) - \phi_{cc}(k,\kappa_<) \\ &\approx -2\omega_2[\tau - \tau_k - \tau_{\mathrm{GD}}(\Omega)],\end{aligned} \tag{2.29}$$

Here $\tau_{\mathrm{GD}}(\Omega) \approx (\phi_{2q+1} - \phi_{2q-1})/(2\omega)$ is the finite difference approximation to the group delay using the consecutive harmonics $(2q+1)\omega$ and $(2q-1)\omega$. The atomic response time $\tau_k = \tau_\lambda(k) + \tau_{cc}(k)$ consists of two contributions:

$$\tau_\lambda(k) = \frac{d\eta_\lambda(k)}{d\epsilon_k} \approx \frac{\eta_\lambda(\kappa_>) - \eta_\lambda(\kappa_<)}{2\omega} \tag{2.30}$$

is called Wigner delay, which represents the temporal shift of single-photon ionization wavepacket;

$$\tau_{cc}(k) = \left.\frac{d\phi_{cc}(k,\kappa)}{d\epsilon_\kappa}\right|_{\kappa=k} \approx \frac{\phi_{cc}(k,\kappa_>) - \phi_{cc}(k,\kappa_<)}{2\omega} \tag{2.31}$$

is the continuum-continuum delay due to the electron probed by the streaking field in the presence of long-range potential with a Coulomb tail, so this is also called measurement-induced delay. The maximal signal of the interference pattern occurs when these two pathway, (a) and (e), are in phase, which results in

$$\tau = \tau_{\mathrm{GD}}(\Omega) + \tau_k. \tag{2.32}$$

Therefore, the interference pattern shows a periodic modulation and the temporal position of the side peaks depend on the group delay of APT. If the atomic response time is known or negligible, the APT can be characterized. The direct measurement of the atomic response time is unknown, but the difference of τ_k between the two

photoelectrons from different atomic orbitals can be measured by using the same attosecond pulse without knowing its temporal structure [38, 55]. However, recent studies using the streaking measurement schemes, which relies on the ATI transition of photoelectron wavepackets, shows that the photoelectron ionized from different atomic orbitals suffers from the uncertainties on the order of tens of attoseconds [38, 55], which is non-negligible in the studies of attosecond dynamics. Therefore, the problem of atomic response time in the the streaking-based methods is inevitable and new methods must be proposed to overcome this obstacle.

Chapter 3

Theoretical methods

In this chapter, the theoretical model and the computational scheme used in following topics about the light-induced hole dynamics are presented. The electronic hole can be produced by different ways depending on the driving laser fields. The characteristic for the different regimes of matter-light interactions was already described in the last chapter: the multiphoton regime which is described in quantum perturbation theory; the tunneling regime which is understood in the combination of quantum tunneling and the electron trajectories based on classical mechanics. The quantum mechanical study of the tunneling regime is introduced in 3.1. The use of strong field approximation provides a semiclassical action which connects to the concept of classical trajectories via stationary phase approximation. The TDCIS method which is used to describe the wavepacket dynamics is introduced in 3.2. The t-SURFF method within the TDCIS scheme for the calculation of photoelectron spectrum is discussed in 3.3. The importance of the additional channel-coupling term is specified here as well as in our publication [95].

3.1 Strong-field approximation of high harmonic generation

As mentioned in the previous chapter, the classical three step model provides the fundamental physical insight of the origin of the HHG. The quantum mechanics study can provide us more accurate description of the property of the harmonic radiation. The most successful quantum-mechanical treatment was proposed by Lewenstein et al [13], known as Lewenstein model. This model is based on the strong field approximation (SFA), which was originally developed by Keldysh [62] to describe the ionization of an atom affected by an external field in the adiabatic limit. In SFA, the laser field

effects after the ionization are dominant in such a way that the influence of the nuclear potential on the continuum states can be neglected. An electron moving in the laser field can be expressed in the Volkov state basis

$$\langle \mathbf{r}|\Psi_A(\boldsymbol{p},t)\rangle = e^{i\boldsymbol{p}\cdot\mathbf{r}}e^{-i\Phi(\boldsymbol{p},t)}. \tag{3.1}$$

The wavefunction is a plane wave with an additional space-independent phase factor

$$\Phi(\boldsymbol{p},t) = \frac{1}{2}\int_{t_0}^{t}\left(\boldsymbol{p}+\boldsymbol{A}(t')\right)^2 dt' \tag{3.2}$$

with the initial time t_0 and satisfies the time dependent Schrödinger equation with electric laser field in velocity form

$$i\frac{\partial}{\partial t}|\Psi_A(\boldsymbol{p},t)\rangle = \frac{1}{2}\left[\hat{\mathbf{P}}+\boldsymbol{A}(t)\right]^2|\Psi_A(\boldsymbol{p},t)\rangle. \tag{3.3}$$

Rather than the kinetic momentum $\boldsymbol{k} = \boldsymbol{p} + \boldsymbol{A}(t)$, the canonical momentum $\boldsymbol{p}$ here is a conserved quantity. In the length gauge, the Volkov state is transformed to

$$\langle \mathbf{r}|\Psi_L(\boldsymbol{p},t)\rangle = e^{i(\boldsymbol{p}+\boldsymbol{A}(t))\cdot\mathbf{r}}e^{-i\Phi(\boldsymbol{p},t)}. \tag{3.4}$$

In the Lewenstein model, there are three assumptions in addition to SFA. First, the contribution from all bound states except the ground state $|G\rangle$ with energy $-I_p$ can be neglected. Second, the depletion of the ground state is neglected. Third, there is only one electron taken into consideration, as called single active electron approximation (SAE). Within these assumptions, the wavefunction can be presented by

$$|\Phi(t)\rangle = |\Phi_{\mathrm{G}}(t)\rangle + |\Phi_{\mathrm{c}}(t)\rangle, \tag{3.5}$$

where $|\Phi_{\mathrm{G}}(t)\rangle = e^{iI_p t}|G\rangle$ is the time evolution of the ground state wavefunction and

$$|\Phi_{\mathrm{c}}(t)\rangle = \int a_{\boldsymbol{k}}(t)|\boldsymbol{k}\rangle d\boldsymbol{k} \tag{3.6}$$

is the continuum wavepacket in the linear combination of the plane wave basis. Here we use the plane waves rather than the Volkov states as a basis because the field-induced phase will be discussed together with other other phases in the in the amplitude term $a_{\boldsymbol{k}}$. The time evolution operator $U(t,t_0)$ from the initial time t_0 to t in the Schrödinger

picture in the integral form satisfies [120]

$$U(t,t_0) = U_0(t,t_0) - i\int_{t_0}^{t} dt_1 U(t,t_1)H_{\rm int}(t_1)U_0(t_1,t_0), \tag{3.7}$$

where $U_0(t,t_0) = \exp[-iH_0(t-t_0)]$ is the field-free propagator with the time-independent field-free Hamiltonian H_0 and $H_{\rm int}(t_1)$ is the external interaction. With the initial condition $|\,\Phi(t_0)\,\rangle = |\,\mathrm{G}\,\rangle$, we can obtain the transition amplitude

$$a_{\boldsymbol{k}}(t) = -i\int_{t_0}^{t} dt_1 \langle\, \boldsymbol{k}\,|U(t,t_1)H_{\rm int}(t_1)U_0(t_1,t_0)|\,\mathrm{G}\,\rangle. \tag{3.8}$$

The electron starts in the ground state $|\,\mathrm{G}\,\rangle$, and then is excited to the continuum state through the interaction at time t_1. For the free electron moving in a laser field, the external interaction can be written as $H_{\rm int}(t_1) = E(t)x$ in the dipole approximation in the length form. Here the electric field is assumed to be linearly polarized along the x-axis. When the electron propagates in the continuum, we apply SFA to the time evolution operator $U(t,t_1) \approx U_V(t,t_1)$, in which Volkov propagator

$$U_V(t,t_1) = \exp\left\{-i\int_{t_1}^{t}\left[-\frac{1}{2}\nabla^2 + H_{\rm int}(t')\right]dt'\right\} \tag{3.9}$$

describes a free particle moving in the electromagnetic fields without any other potentials. Following Volkov propagator, the canonical momentum $\boldsymbol{p} = \boldsymbol{k} - \boldsymbol{A}(t)$ is a conserved quantity such that

$$U_V(t,t_1) = \int d\boldsymbol{p}|\Psi_A(\boldsymbol{p},t)\rangle\langle\Psi_A(\boldsymbol{p},t_1)| \tag{3.10}$$

and

$$\langle\, \boldsymbol{p}+\boldsymbol{A}(t)\,|U_V(t,t_1)|\,\boldsymbol{p}'+\boldsymbol{A}(t_1)\,\rangle = \delta(\boldsymbol{p}-\boldsymbol{p}')e^{-i\tilde{S}(\boldsymbol{p},t,t_1)}, \tag{3.11}$$

where

$$\tilde{S}(\boldsymbol{p},t,t_1) = \int_{t_1}^{t} dt' \frac{(\boldsymbol{p}+\boldsymbol{A}(t'))^2}{2} \tag{3.12}$$

is the additional phase coming from the Volkov state wavefunction and has a physical meaning as the classical action of a charged particle moving in the electromagnetic field. The time dependent wavefunction and the related physical quantity can be obtained from $a_{\boldsymbol{k}}(t)$ and $|\Phi_{\rm c}(t)\rangle$. The HHG power spectrum can be calculated from the Larmor

formula (Eq. 2.8) with dipole acceleration, as well as the second order time derivative of the electric dipole expectation value. With the above expression, the time dependent dipole moment can be written as

$$\begin{aligned} D(t) &= \langle \Phi_{\mathrm{G}}(t)|x|\Phi_{\mathrm{c}}(t)\rangle + \text{c.c} \\ &= i\int_{t_0}^{t} dt_1 \int d\boldsymbol{p} E(t_1) d_x(\boldsymbol{p}+\boldsymbol{A}(t_1)) d_x^*(\boldsymbol{p}+\boldsymbol{A}(t)) \exp[-iS(\boldsymbol{p},t,t_1)] + \text{c.c}, \end{aligned} \tag{3.13}$$

where $d_x(\boldsymbol{p}+\boldsymbol{A}(t)) = \langle \boldsymbol{p}+\boldsymbol{A}(t)\,|\,x\,|\,G\rangle$ is the bound-free dipole transition matrix element and $S(\boldsymbol{p},t,t_1) = \tilde{S}(\boldsymbol{p},t,t_1) + I_p(t-t_1)$. Here the contribution of $\langle\, \Phi_{\mathrm{c}}(t)\,|\,x\,|\,\Phi_{\mathrm{c}}(t)\,\rangle$ is neglected because this term is relatively small. The first term in the integration, $E(t_1)d_x(\boldsymbol{p}+\boldsymbol{A}(t_1))$, is interpreted as an amplitude for an electron in the ground state to make a transition to the continuum at time t' with the canonical momentum p. After propagation in the continuum from t_1 to t, the electron recombines to the ground state with the transition amplitude $d_x^*(\boldsymbol{p}+\boldsymbol{A}(t))$. When the dipole acceleration is considered, this recombination amplitude is replaced by the complex conjugate of

$$d_{ax}(\boldsymbol{p}+\boldsymbol{A}(t)) = \langle\, \boldsymbol{p}+\boldsymbol{A}(t)\,|\,-\partial_x V\,|\,G\,\rangle, \tag{3.14}$$

where V is the atomic potential, according to Ehrenfest theorem [121].

To evaluate the multiple integral in Eq. 3.13, we must analyze the phase $S(\boldsymbol{p},t,t_1)$ Considering the laser field $E(t) = E_0\cos\omega t$, this phase factor becomes

$$S(\boldsymbol{p},t,t_1) = \left(\frac{1}{2}p^2 + I_p + U_p\right)(t-t_1) + \frac{p\sqrt{U_p}}{\omega}(\cos\omega t - \cos\omega t_1) - \frac{U_p}{2\omega}(\sin 2\omega t - \sin 2\omega t_1). \tag{3.15}$$

For the variable $\boldsymbol{p}$, $S(\boldsymbol{p},t,t_1)$ changes in the scale $p \sim (t-t_1)^{1/2}$ while the dipole matrix element changes in the scale $p \sim I_p^{-1/2}$ due to the term $2I_p + (\boldsymbol{p}+\boldsymbol{A}(t))^2$ in its denominator and will be explained later. For $t-t_1$ of the order of one optical cycle, S changes quicker than the dipole matrix element because of $I_p \gg \omega$. For the variable t_1, S is rapidly oscillating in the limit $U_p \gg \omega$. Therefore, with the use of strong infrared laser field, he dominant contribution of the integration in 3.13 comes from the points where $S(\boldsymbol{p},t,t_1)$ has minimal change. Because only the classical action term $\tilde{S}(\boldsymbol{p},t,t')$ depends on momentum p, the stationary phase equation of $S(\boldsymbol{p},t,t_1)$ equals to the one

of $\tilde{S}(\boldsymbol{p}, t, t_1)$,

$$\frac{\partial}{\partial \boldsymbol{p}} S(\boldsymbol{p}, t, t_1) = \frac{\partial}{\partial \boldsymbol{p}} \tilde{S}(\boldsymbol{p}, t, t_1) = \int_{t_1}^{t} dt' \Big[\boldsymbol{p} + \boldsymbol{A}(t') \Big] = \Delta k = 0. \tag{3.16}$$

This equation is nothing else but equal to the classical collision condition $x(t) = x(t_1)$, and the stationary momentum is

$$\boldsymbol{p}_{(s)} = -\frac{\int_{t_1}^{t} dt' \boldsymbol{A}(t')}{t - t_1}. \tag{3.17}$$

Therefore, the term $\langle \Phi_{\mathrm{G}}(t) | x | \Phi_c(t) \rangle$ with the stationary phase approximation on $\boldsymbol{p}_{(s)}$ can be written as

$$\langle \Phi_{\mathrm{G}}(t) | x | \Phi_c(t) \rangle \approx -i \int_{t_0}^{t} dt_1 \left(\frac{-2\pi i}{t - t_1} \right)^{\frac{n}{2}} \mathrm{d}_x^*(\boldsymbol{p}_{(s)} + \boldsymbol{A}(t)) \mathrm{d}_x(\boldsymbol{p}_{(s)} + \boldsymbol{A}(t_1)) E(t_1) e^{-iS_0(\boldsymbol{p}_{(s)}, t, t_1)} \tag{3.18}$$

This stationary phase approximation to the SFA gives an intuitive classical interpretation shown in the classical action, so this quantum mechanical treatment can be viewed as a semiclassical model. As a matter of fact, this procedure is the concept of Feynman's path integral formulation in quantum mechanics and classical trajectories with canonical momentum $p_{(s)}(t, t_1)$ arise naturally in the classical limit $S \gg \hbar = 1$. The prefactor $[-2\pi i/(t - t_1)]^{n/2}$, which comes from the second derivative of S, is the quantum diffusion of the electronic wave packets and n is the space dimension. This diffusion term suppresses the trajectories with long excursion time such that the trajectories with duration smaller than one optical cycle are dominant.

To get the physical picture of tunneling ionization, further approximation should be performed. On the contrary to p, the stationary phase condition with respect to t_1 depends on not only the classical action $\tilde{S}$ but also the ionization potential I_p:

$$\left. \frac{\partial S}{\partial t_1} \right|_{t_1 = t_{1(s)}} = -\frac{1}{2} [\boldsymbol{p}_{(s)}(t, t_{1(s)}) - \boldsymbol{A}(t_{1(s)})]^2 - I_p = 0 \tag{3.19}$$

If $I_p = 0$, which is the case of the simple man model, this condition has the solution $t_1 = t_i$ satisfying $\boldsymbol{p}_{(s)} + \boldsymbol{A}(t_i) = 0$. However, this condition can never be fulfilled for the real t_1 with any positive I_p, so the stationary point $t_{1(s)}$ is a complex quantity. In other words, the condition Eq. 3.19 converts infinite classical trajectories to several

finite quasiclassical trajectories with complex ionization time $t_{1(s)}$ for a given t. The complex time $t_{1(s)}$ can be calculated by reexpressing $S_1'(t, t_{1(s)}, \boldsymbol{p}) = 0$ using Taylor expansion around the real ionization time $t_1 = t_i$ up to higher order.

$$\begin{aligned}\left.\frac{\partial S}{\partial t_1}\right|_{t_1=t_{1(s)}} &\approx \left.\frac{\partial S}{\partial t_1}\right|_{t_1=t_i} + \left.\frac{\partial^2 S}{\partial t_1^2}\right|_{t_1=t_i}(t_{1(s)}-t_i) + \frac{1}{2}\left.\frac{\partial^3 S}{\partial t_1^3}\right|_{t_1=t_i}(t_{1(s)}-t_i)^2 \\ &= -I_p - \frac{|\boldsymbol{E}(t_i)|^2}{2}(t_{1(s)}-t_i)^2\end{aligned} \tag{3.20}$$

The stationary time $t_{1(s)}$ has a real part t_i and a complex part that is given by

$$t_{1(s)} - t_i \approx \pm i\frac{\sqrt{2I_p}}{|E(t_i)|}. \tag{3.21}$$

The imaginary part of $t_{1(s)}$, referred to as Keldysh tunneling time $\tau_k(t_i) \equiv |\mathrm{Im}(t_{1(s)})|$, can be interpreted as the time of an electron passing through the barrier [62, 63]. It can also be obtained by calculating the time an electron takes to be deaccelerated from velocity $\sqrt{2I_p}$ to zero under a constant deacceleration force $|E(t_i)|$. When the Keldysh tunneling time defined at the leaser peak is short compared with the quarter laser period, the ionization process can be treated as an electron tunneling through a static field. Defining the Keldysh parameter

$$\gamma \equiv \frac{\omega\sqrt{2I_p}}{E_0} = \omega\tau_k(0), \tag{3.22}$$

the quasi-static tunnelling picture is approciate for $\gamma \ll 1$. To determine $t_{1(s)}$ is on the upper or lower complex plane, the second derivative of S_1 at these two points has to be calculated:

$$\left.\frac{\partial^2 S}{\partial t_1^2}\right|_{t_1=t_{1s}} \approx \left.\frac{\partial^2 S}{\partial t_1^2}\right|_{t_1=t_i} + \left.\frac{\partial^3 S_1}{\partial t_1^3}\right|_{t_1=t_i}(t_{1s}-t_i) = \mp i\sqrt{2I_p}|E(t_i)|. \tag{3.23}$$

To ensure e^{-iS} does not diverge, we choose $t_1 = t_i + i\sqrt{2I_p}/|E(t_i)|$ with the integration path parallel to the real time axis and $S''(\boldsymbol{p}_{(s)}, t, t_1)|_{t=t_{1(s)}} = -i\sqrt{2I_p}|E(t_i)|$. By

expanding $S(\boldsymbol{p}_{(s)}, t, t_{1(s)})$ up to third order around $t_{1(s)} = t_i$, we can obtain

$$S(\boldsymbol{p}_{(s)}, t, t_{1(s)}) = S(\boldsymbol{p}_{(s)}, t, t_i) - \frac{i}{3}\frac{(2I_p)^{\frac{3}{2}}}{|E(t_i)|}, \tag{3.24}$$

and the imaginary part is the action $S(\boldsymbol{p}_{(s)}, t, t_{1(s)})$ with the contour time integration from $t_{1(s)}$ to t_i as shown in Fig. 3.1 (b). However, the stationary phase point coincides with the singularity of $d_x(\boldsymbol{p}_{(s)} + \boldsymbol{A}(t_1))$ at $t_{1(s)}$ because of the long range tail $\exp(-\sqrt{2I_p}r)$ of the ground state. This long range tail together with plane wave $\exp(i\boldsymbol{k}\cdot\boldsymbol{r})$ would result in $2I_p + (\boldsymbol{p} + \boldsymbol{A}(t_1))^2$ in the denominator [122]. Here we use the 3D Hydrogen-like 1s state as an example:

$$d_x(\boldsymbol{p} + \boldsymbol{A}(t_1))E(t_1) = \frac{iC(I_p)[p_x + A(t_1)]E(t_1)}{((\boldsymbol{p} + \boldsymbol{A}(t_1))^2 + 2I_p)^3} \approx -\frac{iC(I_p)}{16[S''(\boldsymbol{p}, t, t_{1(s)})]^2(t_1 - t_{1(s)})^3}, \tag{3.25}$$

where

$$C(I_p) = \frac{2^{7/2}(2I_p^{5/4})}{\pi}. \tag{3.26}$$

There is a third-order pole at the stationary phase point. The stationary phase approximation with a contour passing through the saddle point with the nth order pole can be evaluated as [122]

$$F_n \equiv \int_C dx F(x)\frac{e^{-ig(x)}}{(x - x_{(s)})^n} \approx i^n F(x_{(s)})\frac{\Gamma(n/2)}{2\Gamma(n)}\left(\frac{2\pi}{g''(x_{(s)})}\right)^{1/2}(2g''(x_{(s)}))^{n/2}e^{-ig(x_{(s)})} \tag{3.27}$$

The contour of the integration over t_1 evaluated from t_0 to t (thick lines in Fig. 3.1 (a)) can be deformed to go through the saddle point $t_{1(s)}$ (red dashed line in Fig. 3.1 (a)) and the integral can be evaluated:

$$\int_{t_0}^{t} dt_1 \; \mathrm{d}_x(\boldsymbol{p}_{(s)} + A(t_1))E(t_1)e^{-iS(\boldsymbol{p}_{(s)}, t, t_1)} = -\pi i C(I_p)\sum_{t_{1(s)}}\frac{e^{-iS(\boldsymbol{p}_{(s)}, t, t_{1(s)})}}{32S''(\boldsymbol{p}_{(s)}, t, t_{1(s)})}. \tag{3.28}$$

Therefore, together with Eq. 3.18, 3.23 and 3.24, the time dependent dipole moment can be written as [123]

$$d(t) = \sum_{t_i} a_{\mathrm{ion}}(t_i)a_{\mathrm{pr}}(t, t_i)a_{\mathrm{rec}}(t) + \mathrm{c.c.}, \tag{3.29}$$

where

$$
\begin{aligned}
a_{\mathrm{ion}}(t_i) &= \frac{\pi C(I_p)}{32\sqrt{2I_p}|E(t_i)|}\exp\left[-\frac{(2I_p)^{3/2}}{3|E(t_i)|}\right] \\
a_{\mathrm{pr}}(t,t_i) &= \left(\frac{2\pi i}{t-t_i}\right)^{3/2}\exp\left[-\frac{i}{2}\int_{t_i}^{t}[\boldsymbol{p}_{(s)}(t,t_i)+\boldsymbol{A}(t')]^2dt' - iI_p(t-t_i)\right] \\
a_{\mathrm{rec}}(t) &= \mathrm{d}_x^*(\boldsymbol{p}_{(s)}+A(t)).
\end{aligned}
\tag{3.30}
$$

are the transition amplitudes related to ionization, propagation and recombination process. In this expression, the contribution of the propagation of the quasiclassical trajectory is also factorized into two part as shown in Eq. 3.24 and Fig. 3.1 (b). First, the effect of quantum tunneling from $t_{1(s)}$ to t_i is described in the exponential term of $a_{\mathrm{ion}}(t_i)$, resulting in the ADK ionization rate $|a_{\mathrm{ion}}(t_i)|^2$ developed by Ammosov, Delone and Krainov [124]. Second, the propagation of the classical trajectory, which follows classical dynamics, from t_i to t is presented in $a_{\mathrm{pr}}(t,t_i)$. Although the expression in Eq. 3.30 is derived from the Hydrogen-like ground state wavefunction, only the prefactor of $a_{\mathrm{ion}}(t_i)$ changes if we use different ground state wavefunctions.

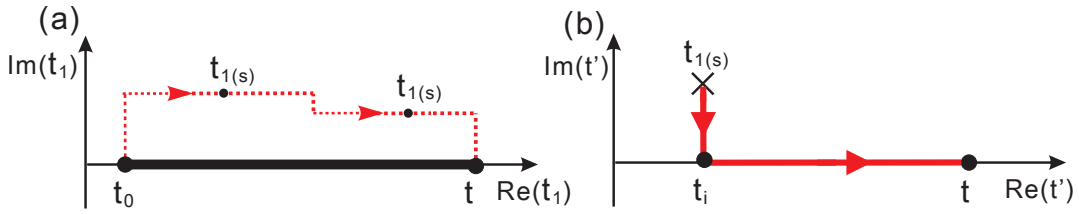

Figure 3.1: (a) The contour of the integration with respect to the ionization time t_1 (Eq. 3.28) is shown as a red dash line, and the original integration path is from t_0 to t along the thick black line on the real axis. (b) The countour of the time integration in the action $S(p_{(s)},t,t_{1(s)})$.

The detailed form of Eq. 3.30 depends on the properties of the chosen system, including the dimension and the initial-state wavefunctions, which is decided by the atomic potential. The dimension only affects the exponent in a_{pr}. When the 1D system is considered, this exponent is 1/2 rather than 3/2. For any kind of effective atomic potential, the bound-continuum transition always presents a singularity at the saddle point $t_1 = t_{(1s)}$ of the action action $S(p_{(s)},t_i,t_1)$ due to the long-range behavior of the

potential [122]. Therefore, the stationary phase analysis still holds. The tunneling time, the exponential factor of tunneling amplitude a_{ion} and the propagation phase of a_{pr} does not explicitly depend on the mathematical form of the potential. For example, we consider a 1D system with the soft potential

$$V(x) = -\frac{Z_{\text{eff}}}{\sqrt{x^2 + a^2}}. \tag{3.31}$$

and two uncorrelated electrons. The electron in the first excited state is treated as the outer most electron, and then the wavefunction has the asymptotic behavior

$$\lim_{|x|\to\infty} \langle x|\Psi_{\text{out}}\rangle \approx x e^{-\sqrt{2I_p}|x|}, \tag{3.32}$$

resulting in the approximated bound-continuum dipole transition matrix element

$$\mathrm{d}_x(p + A(t_1)) \approx \frac{1 - 8(p + A(t_1))^2}{((p + A(t_1))^2 + 2I_p)^2}. \tag{3.33}$$

There is a second-order pole at the saddle point and the integration over t_1 can be evaluated using Eq. 3.27. Finally, the ionization amplitude can be rewritten as

$$a_{\text{ion}}(t, t_i) = \frac{\tilde{C}(I_p, p_{(s)})E(t_i)}{|E(t_i)|^{\frac{3}{2}}} \exp\left[-\frac{(2I_p)^{3/2}}{3|E(t_i)|}\right] \tag{3.34}$$

where $\tilde{C}(I_p, p_{(s)})$ is a constant depending on I_p and the canonical momentum $p_{(s)}$.

To calculate the HHG spectrum, we perform the Fourier transform of the time dependent dipole (or dipole acceleration) moment

$$\tilde{D}(\Omega) = \int dt D(t) e^{i\Omega t} \tag{3.35}$$

The main contribution of this integration can also be extracted by the stationary phase approximation with respect to t from the phase of $\langle \Phi_{\text{G}}(t)|x|\Phi_c(t)\rangle$ and the phase of

the emitted radiation:

$$\begin{aligned}\Omega &= \frac{1}{2}\Big[p_{(s)}(t,t_i)+A(t)\Big]^2 + I_p\left(1+\frac{\partial t_i}{\partial t}\right)\\ &= \frac{1}{2}\Big[p_{(s)}(t,t_i)+A(t)\Big]^2 + I_p\left[1+\frac{A(t)-A(t_i)}{E(t_i)(t-t_i)}\right].\end{aligned} \tag{3.36}$$

This condition shows the energy conservation law in the recombination process in the simple man model except for a correction term. In the strong field limit $U_p \gg I_p$, the cutoff energy is modified to be $\Omega_{cutoff} = 3.17U_p + 1.32I_p$ [13]. The stationary phase condition from the other complex conjugate term $\langle \Phi_c(t)|x|\Phi_{\mathrm{G}}(t)\rangle$ does not contribute to the emitted radiation and can be neglected.

In conclusion, despite some assumptions, the stationary phase approximation with respect to t_1, p, and t for the Lewenstein model provides us a physical connection to the tunneling ionization, propagation along the classical trajectories, and photon-emitted recombination in Corkum's three step model. The direct numerical solution of time-dependent Schrödinger equation and the extended model is needed for more complicated situations, such as the additional use of high frequency laser, many-electron effects, and the population of more than one bound state. In these complicated situations, the stationary phase condition would be different or not able to describe some phenomena as shown in the following chapter.

3.2 TDCIS for wavepacket propagation

In the light-induced dynamics, an electronic hole is produced photoionization or tunneling ionization, and can be transferred to other electronic shells by the lights. The hole transfer process is the result of the rearrangement of electrons. Therefore, the light-induced dynamics involves an inner-outer-shell two-electron effect. We formulate this time-dependent process using a two-electron one-dimensional model system:

$$H(t) = T_1 + T_2 + H_1 + H_2 + H_{ee} + V(t), \tag{3.37}$$

where T_i is the kinetic operator, H_i is an effective atomic potential [125, 126], H_{ee} is the 1D Coulomb interaction between electrons, and the external potential $V(t) = -E(t)(z_1 + z_2)$ is laser-electron interaction in the dipole approximation. Since rare

gases are closed-shell atoms, the electronic ground state is spin singlet. However, in this effective two electron model, the ground state is chosen as a spin-triplet state ($S = 1$) in such a way that the two active electrons do not fill in the same orbital.

A time-dependent configuration interaction singles provides an efficient treatment of different many-body effects and coupled-channel behavior[83]. Configuration-interaction (CI) is a common post-Hartree-Fock method. The wave function is constructed by the Slater determinant basis which contains the Hartree-Fock ground state and the particle-hole configurations generated by exciting electrons from the filled orbitals to virtual ones. Because in the light-induced hole dynamics we consider one ionized electron which may come from different orbitals, TDCI-Singles is the most suitable approach. In our system, we will neglect the laser magnetic field effects and relativistic effects, the total spin and its projection on z direction is a conserved quantity. Without loss of generality, we only consider the case $S_z = 1$ and neglect the spin indices because the electric dipole transition does not change the spin configuration. The ground state and the single excitations can be written as:

$$|\Phi_0\rangle = \hat{c}_2^\dagger \hat{c}_1^\dagger |0\rangle, \tag{3.38}$$

$$|\Phi_i^a\rangle = \hat{c}_a^\dagger \hat{c}_i |\Phi_0\rangle, \tag{3.39}$$

where $|0\rangle$ is the vacuum state with $\hat{c}_p^\dagger$,$\hat{c}_p$ being creation and annihilation operators of the corresponding spin orbitals $|\varphi_p\rangle$. Here and in the following, indices i,j,k,l,... are used for spatial orbitals that are occupied in $|\Phi_0\rangle$. Unoccupied (virtual) orbitals are symbolized by indices a,b,c,..., whereas for general orbitals (occupied or unoccupied) indices p,q,r,s,... are employed.

With the use of Hartree-Fock and the CIS basis, the many-body wave packet is given by the ansatz,

$$|\Psi, t\rangle = \alpha_0(t)|\Phi_0\rangle + \sum_i \sum_a \alpha_i^a(t)|\Phi_i^a\rangle \tag{3.40}$$

with initial conditions $\alpha_0(t_0) = 1$ and $\alpha_i^a(t_0) = 0$. For the atomic system interacting with laser field $E(t)$ linearly polarized along the z axis, the time-dependent many-body Hamiltonian can be written as:

$$\hat{H}(t) = \hat{H}_0 + \hat{H}_1 - E(t)\hat{z}, \tag{3.41}$$

where $\hat{H}_0$ is the one-particle Hamiltonian with orbital energies ε_p,

$$\hat{H}_0 = \sum_p \varepsilon_p \hat{c}_p^\dagger \hat{c}_p. \tag{3.42}$$

Here $\hat{H}_0$ is chosen as the N-electron Fock operator and $\hat{H}_1 = \hat{V}^C - \hat{V}^{(HF)}$, where

$$\hat{V}^C = \frac{1}{2} \sum_{p,q,r,s} v_{p,q,r,s} \hat{c}_p^\dagger \hat{c}_q^\dagger \hat{c}_s \hat{c}_r \tag{3.43}$$

is the Coulomb two-body operator with the matrix element

$$v_{pqrs} = \int \int dx_1 dx_2 \varphi_p^*(x_1) \varphi_q^*(x_2) r_{12}^{-1} \varphi_r(x_1) \varphi_s(x_2), \tag{3.44}$$

and

$$\hat{V}^{(HF)} = \sum_{p,q} \left\{ \sum_i v_{p,i[q,i]} \right\} \hat{c}_p^\dagger \hat{c}_q \tag{3.45}$$

represents the interaction with the Hartree-Fock mean-field. Any one-body operator $\hat{D}$, such as dipole operator $\hat{z}$, with matrix element D_{pq} with respect to orbital p and q in second quantization reads

$$\hat{D} = \sum_{pq} D_{pq} \hat{c}_p^\dagger \hat{c}_q. \tag{3.46}$$

Inserting the ansatz Eq. 3.40 into the time-dependent Schrödinger equation and projecting the resulting expression onto $|\Phi_0\rangle$ and $|\Phi_i^a\rangle$, respectively. The coupled channel equation can be written as [83]:

$$i\dot{\alpha_0} = -E(t) \sum_{i,a} \alpha_i^a z_{ia} \tag{3.47}$$

$$i\dot{\alpha_i^a} = (\varepsilon_a - \varepsilon_i)\alpha_i^a + \sum_{i',a'} \alpha_{i'}^{a'} (v_{ii'aa'} - v_{iai'a'}) - E(t) \left\{ \alpha_0 z_{ai} + \sum_{a'} \alpha_i^{a'} z_{aa'} - \sum_{i'} \alpha_{i'}^a z_{ii'} \right\} \tag{3.48}$$

To understand the hole dynamics and the corresponding wavepacket propagating in the real space, a time-dependent orbital $|\chi_i, t\rangle$ that collects all the single excitations originating from the occupied orbital $|\chi_i, t\rangle = \sum_a \alpha_i^a(t)|\varphi_a\rangle$ is introduced [83]. The equation of motion can be written as:

$$i\dot{\alpha_0} = -E(t) \sum_i \langle \varphi_i | \hat{z} | \chi_i, t \rangle \tag{3.49}$$

$$i\frac{\partial}{\partial t}|\chi_i\rangle = (\hat{H}_0 - \varepsilon_i)|\chi_i\rangle + \sum_{i'} \hat{P}\{\hat{K}_{i'i} - \hat{J}_{i'i}\}|\chi_i'\rangle - E(t)\hat{P}\hat{z}\{\alpha_0|\varphi_i\rangle + |\chi_i\rangle\} + E(t)\sum_{i'} z_{i'i}|\chi_{i'}\rangle, \tag{3.50}$$

where $\hat{J}_{i'i}$ and $\hat{K}_{i'i}$ are, respectively, generalized Coulomb and exchange operators associated with the orbitals $|\varphi_i\rangle$ and $|\varphi_i'\rangle$:

$$v_{ai'a'i} = \langle\, \varphi_a \,|\, \hat{J}_{i'i} \,|\, \varphi_{a'} \,\rangle \tag{3.51}$$

$$v_{ai'ia'} = \langle\, \varphi_a \,|\, \hat{K}_{i'i} \,|\, \varphi_{a'} \,\rangle, \tag{3.52}$$

and $\hat{P}$ is a projection operator defined as $\hat{P} = \sum_a |\varphi_a\rangle\langle\varphi_a| = I - \sum_i |\varphi_i\rangle\langle\varphi_i|$. This establishes a system of a linear, coupled equations for different hole channels. Different kind of coupling can be easily understood and even removed in Eq. 3.50 and Eq. 3.2. For example, the second term in the right hand sides (RHS) of Eq. 3.50 represents the channel-coupling due to electron-electron correlation and the fourth term there represents the laser-driven channel-coupling. The transition between the ground state and the electron-hole wavepacket is shown in the third terms in RHS of Eq. 3.50 as well in Eq. 3.2. All information, including the physical observables, can be obtained by calculating α_0 and $|\chi_i\rangle$. For instance, the expectation value of an arbitrary spin-independent one-body operator, such as the dipole operator and the dipole acceleration operator, $\hat{D} = \sum_{pq} d_{pq}\hat{c}_p^\dagger\hat{c}_q$ can be expressed as

$$\begin{aligned}\langle\Psi,t|\hat{D}|\Psi,t\rangle =& |\alpha_0|^2 \sum_i d_{ii} + \sum_i \langle\chi_i,t|\hat{d}|\chi_i,t\rangle + \sum_i d_{ii}\sum_j \langle\chi_j,t|\chi_j,t\rangle \\ &- \sum_{ii'} d_{ii'}\langle\chi_{i'},t|\chi_i,t\rangle + 2\ \mathrm{Re}\left(\alpha_0 \sum_i \langle\chi_i,t|\hat{d}|\varphi_i\rangle\right).\end{aligned} \tag{3.53}$$

We can obtain the HHG power spectrum by Fourier-transforming the time dependent dipole or dipole acceleration as the same as Eq. 3.35. In order to understand the dynamics of ionic states deeply we can construct the reduced density matrix of the residual ion by tracing all singly excited states with the same ionic hole of the total density matrix $\hat{\rho}(t)$ [83, 71, 127]:

$$\rho_{ii'}^{(\mathrm{ion})}(t) \equiv \sum_a \langle\Psi_i^a|\hat{\rho}(t)|\Psi_{i'}^a\rangle = \langle\chi_i,t|\chi_{i'},t\rangle, \tag{3.54}$$

$$\hat{\rho}(t) = |\Psi, t\rangle\langle\Psi, t|. \tag{3.55}$$

The diagonal term $\rho_{ii}^{(\mathrm{ion})}$ is the probability of forming a hole in orbital $|\varphi_i\rangle$, or in other words, forming an ion from orbital $|\varphi_i\rangle$. Therefore, the conservation of the norm in TDCIS can be expressed as

$$|\alpha_0(t)|^2 + \sum_i \rho_{ii}^{(\mathrm{ion})}(t) = 1. \tag{3.56}$$

The off-diagonal matrix elements $\rho_{ij}^{(\mathrm{ion})}$ can be interpreted as the coherence. To account for the decay of the i-th inner shell vacancy in the TDCIS formalism, we can introduce a phenomenological decay term with decay width Γ_i to Eq. 3.50 [128]:

$$i\frac{\partial}{\partial t}|\chi_i\rangle = (\hat{H}_0 - \varepsilon_i - i\frac{\Gamma_i}{2})|\chi_i\rangle + \sum_{i'} \hat{P}\{\hat{K}_{i'i} - \hat{J}_{i'i}\}|\chi_i'\rangle - E(t)\hat{P}\hat{z}\{\alpha_0|\varphi_i\rangle + |\chi_i\rangle\} + E(t)\sum_{i'} z_{i'i}|\chi_{i'}\rangle. \tag{3.57}$$

When the decay is taken into consideration, Eq. 3.56 fails because the problem we treat becomes an open system.

The numerical results presented in the main text are obtained using an 1D effective central potential and effective electron-electron repulsive potential [125, 126]

$$\begin{aligned} V_{\mathrm{eff}}(z) &= \frac{Z_{\mathrm{eff}}}{\sqrt{z^2 + z_c^2}} \\ V_{\mathrm{ee}}(z_1, z_2) &= \frac{Z_{\mathrm{ee}}}{\sqrt{(z_1 - z_2)^2 + z_e^2}} \end{aligned} \tag{3.58}$$

with parameters Z_{eff},Z_{ee},z_c, and z_e that reproduce the experimental ionization energies and the excitation energies of the selected system. Eq. 3.44 should be rewritten as

$$v_{pqrs} = \int\int dz_1 dz_2 \varphi_p^*(z_1)\varphi_q^*(z_2)V_{\mathrm{ee}}(z_1, z_2)\varphi_r(z_1)\varphi_s(z_2). \tag{3.59}$$

The parameters of the systems we consider are presented in Table 3.1. We consider two kinds of models: the correlated TDCIS model and the independent particle approximation (IPA), which is the special case of the TDCIS model with $Z_{\mathrm{ee}} = 0$. The finite difference method is employed with the boundary at $z = \pm z_{\max}$ with grid points N_g. In the time propagation procedure, the 4th-order Runge-Kutta method is used and masking function is applied in each time step as the absorber of outgoing parts of

the wave packet outside some large distance R_a in order to remove the reflection effect due to numerical boundary condition. Consequently, conservation of the norm (Eq. 3.56) does not hold anymore and instead the ionization probability after the laser field ceases can be obtained :

$$P_{\text{ion,ab}} = 1 - \lim_{t\to\infty}[|\alpha_0(t)|^2 + \sum_i \rho_{ii}^{(\text{ion})}(t)]. \tag{3.60}$$

Although the artificial absorber is applied in the numerical calculation, the physical quantities which are defined in the finite volume, such as time-dependent dipole and the HHG power spectrum, can be directly obtained from the time-dependent wavefunction. However, the quantities such as photoelectron spectrum, which is related to the outgoing wavepackets, are affected by the boundary conditions of the computational box and any kinds of absorber. In the following section, we will introduce the t-SURFF method, in which the asymptotic information of the outgoing wavepackets can be accumulated during the time propagation, to calculate the photoelectron spectrum.

Atom	energy level	Z_{eff}	z_{c}	Z_{ee}	z_{e}	z_{max}	grid point N_g
Ne	2s-2p	1.795	0.7	0	any	200	1500
Ne	2s-2p	2	0.755	1	9	200	1500
Ar	2s-3p	1.965	0.158	2.965	0.113	200	1500
Kr	3d-4p	1.05	0.128	0	any	200	1400
Kr	3d-4p	2	0.288	1	0.4	200	1400

Table 3.1: Parameters in the soft potentials defined in Eq. 3.58 for different systems. $Z_{\text{ee}} = 0$ corresponds to the independent particle approximation.

3.3 t-SURFF for photoionization spectrum

To calculate photoelectron spectra with a particular hole in the ion, we need to evaluate the transition amplitude between a modified Volkov state and the outgoing muti-channel wavepacket, $\langle \chi_{\mathbf{k},i}(t) | \chi_i(t) \rangle$, at a time, t, long after all interactions have ceased. The modified Volkov state in length gauge, $|\chi_{\mathbf{k},i}(t)\rangle$, with momentum $\mathbf{k}$ includes an additional phase-factor for a hole at the orbital $|\varphi_i\rangle$, and it satisfies the equation

$$i\frac{\partial}{\partial t}|\chi_{\mathbf{k},i}(t)\rangle = \left(\frac{1}{2}\hat{\nabla}^2 - \varepsilon_i - E(t)\hat{z}\right)|\chi_{\mathbf{k},i}(t)\rangle \equiv \hat{H}_i(t)|\chi_{\mathbf{k},i}(t)\rangle. \tag{3.61}$$

Here $\hat{H}_i(t)$ represents the modified Volkov Hamiltonian for the electron moving in the external laser field with a hole fixed at the orbital $|\varphi_i\rangle$. As mentioned in the previous section, the photoelectron spectrum cannot be obtained directly from the time-dependent wavefunction because of the absorber. To avoid the problem, one solution is using a large box size so that the outgoing wavepackets are not absorbed after the end of the external interaction. However, the photoelectron wavepacket will propagate far away from the atom during the interaction, so the large box size as well as many grid points are needed and will increase numerical difficulty especially for a long pulse. The distance the photoelectron wavepacket propagates is proportional to the velocity and the pulse duration T, hence the Hamiltonian size needed is proportional to $T^{2n}E_k^n$, where n is the dimension of the system.

To overcome the difficulty of the calculation with a large box and the effect of absorber, we adapt the time-dependent surface flux (t-SURFF) [90, 93] method to the multi-channel TDCIS formalism. The basic idea of the t-SURFF method is to convert the spatial integration into the temporal integration of the flux through a surface [94, 95]. First, we define the overlap from a large distance R_c to infinity between the modified Volkov state and the wavepacket in a given channel, i, by a stepfunction:

$$A_{\mathbf{k},i}(R_c,t) \equiv \langle\, \chi_{\mathbf{k},i}(t) \,|\, \theta(R_c) \,|\, \chi_i(t) \,\rangle = \int_{|\mathbf{r}|>R_c} d^{(3)}r\ \chi^*_{\mathbf{k},i}(r,t)\chi_i(r,t), \tag{3.62}$$

that converges to the transition amplitude $\langle\, \chi_{\mathbf{k},i}(t) \,|\, \chi_i(t) \,\rangle$ for sufficiently large time T_c. Eq. 3.62 can also be written as

$$\begin{aligned} A_{\mathbf{k},i}(R_c,T_c) &= \int_{t_0}^{T_c} dt \frac{d}{dt}\langle\chi_{\mathbf{k},i}(t)|\theta(R_c)|\chi_i(t)\rangle \\ &= \int_{t_0}^{T_c} dt \left[\left(\frac{d}{dt}\langle\chi_{\mathbf{k},i}(t)|\right)\theta(R_c)|\chi_i(t)\rangle + \langle\chi_{\mathbf{k},i}(t)|\theta(R_c)\frac{d}{dt}|\chi_i(t)\rangle\right]. \end{aligned} \tag{3.63}$$

If we neglect correlation effects and the ionic potential outside R_c, then the time-dependent wavepacket $|\chi_i(t)\rangle$ follows the equation of motion

$$i\frac{\partial}{\partial t}|\chi_i(t)\rangle = \hat{H}_i(t)|\chi_i(t)\rangle + E(t)\sum_j z_{ij}|\chi_j(t)\rangle. \tag{3.64}$$

In addition to the modified Volkov Hamiltonian, there is another term which makes different channels coupled to each other by laser field. With Eq. 3.61, 3.63 and 3.64, we

can convert $A_{\mathbf{k},i}(R_c,T_c)$ from the spatial integration at T_c to the temporal integration:

$$\begin{aligned}
&A_{\mathbf{k},i}(R_c,T_c)\\
=&i\int_{t_0}^{T_c}dt\langle\chi_{\mathbf{k},i}(t)|\left[\hat{H}_i(t)\theta(R_c)|\chi_i(t)\rangle-\sum_j\theta(R_c)\left(\hat{H}_i(t)\delta_{ij}+E(t)z_{ij}\right)|\chi_j(t)\rangle\right]\\
=&i\int_{t_0}^{T_c}dt\langle\chi_{\mathbf{k},i}(t)|[\hat{H}_i(t),\theta(R_c)]|\chi_i(t)\rangle-i\sum_j z_{ij}\int_{t_0}^{T_c}dtE(t)\langle\chi_{\mathbf{k},i}(t)|\theta(R_c)|\chi_j(t)\rangle\\
=&-\int_{t_0}^{T_c}dtJ_{\mathbf{k},i}(R_c,t)-\int_{t_0}^{T_c}dtK_{\mathbf{k},i}(R_c,t)
\end{aligned}\tag{3.65}$$

We gain two terms and the first term is the time integration of the flux

$$J_{\mathbf{k},i}(R_c,t)=\frac{1}{2i}\left[-\chi^*_{\mathbf{k},i}(r,t)\partial_r\chi_i(r,t)+\chi_i(r,t)\partial_r\chi^*_{\mathbf{k},i}(r,t)\right]\Big|_{R_c}\tag{3.66}$$

through the boundary R_c from t_0 to T_c as indicated in [90, 129]. Compared with the previous work [129], the second term is new and its integrand

$$K_{\mathbf{k},i}(R_c,t)=i\sum_j z_{ij}\int_{t_0}^{T_c}dtE(t)\langle\,\chi_{\mathbf{k},j}(t)\,|\,\theta(R_c)\,|\,\chi_j(t)\,\rangle e^{-i(\varepsilon_i-\varepsilon_j)t}\tag{3.67}$$

represents the channel-coupling of the TDCIS via laser field after the electronic wavepackets pass though R_c [95]. This contribution is missing in the integration of the flux at R_c. This channel-coupling term can be viewed as an external source from other channels, when the states of the ion makes a transition. In other words, if the field-driven transition between two different ionic states plays the role in the physical process, this channel-coupling term cannot be neglected. In case of the photoelectron spectrum measured in coincidence with parent ions, this term is especially important. Therefore, the schematic of the TDCIS-tSRUFF method can be described in Fig. 3.2. The t-SURFF integral equation

$$A_{\mathbf{k},i}(R_c,T_c)=-\int_{t_0}^{T_c}dtJ_{\mathbf{k},i}(R_c,t)-\int_{t_0}^{T_c}dtK_{\mathbf{k},i}(R_c,t)\tag{3.68}$$

is numerically evaluated with $\chi_i(r,t)$ determined by TDCIS under the initial condition $A_{\mathbf{k},i}(R_c,t_0)=0$. Finally, the momentum spectrum $\sigma_{\mathbf{k},i}(\mathbf{k})$ and energy spectrum $\sigma_{E,i}(E)$

for the channel i are given by

$$\sigma_{\mathbf{k},i}(\mathbf{k}) \equiv |A_{\mathbf{k},i}(R_c, T_c)|^2 \tag{3.69}$$

$$\sigma_{E,i}(E) \equiv \sum_{|\mathbf{k}|=\sqrt{2E}} \frac{\sigma_{\mathbf{k}}(\mathbf{k})}{|\mathbf{k}|}. \tag{3.70}$$

The total ionization probability can be obtained by the integration of the spectrum

$$P_{\text{ion,t-SURFF}} = \sum_i \int dE \sigma_{E,i}(E). \tag{3.71}$$

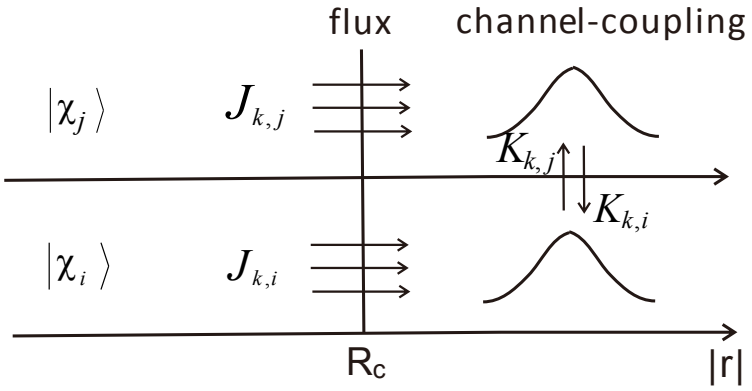

Figure 3.2: Schematic of TDCIS-tsurff method is shown. The transition amplitude is composed of the flux terms, which collects all information about the normal Volkov propagation of wave packets, and the channel-coupling terms, which exist even though the wave packets propagate away from R_c.

Numerically, the procedure of the wavefunction propagation is the same as what we mention in the previous section, and the t-SURFF integral equation is implemented in each time step. The surface R_c for counting flux should be large enough so that the ionic potential and the correlation effect can be neglected, and smaller than the beginning of the absorber R_a. The convergent results should not depend on the choice of R_c and can be double-checked with the comparison of the total ionization probability using $P_{\text{ion,ij}}$ and $P_{\text{ion,t-SURFF}}$.

To understand the importance of the channel-coupling term in the t-SURFF integral

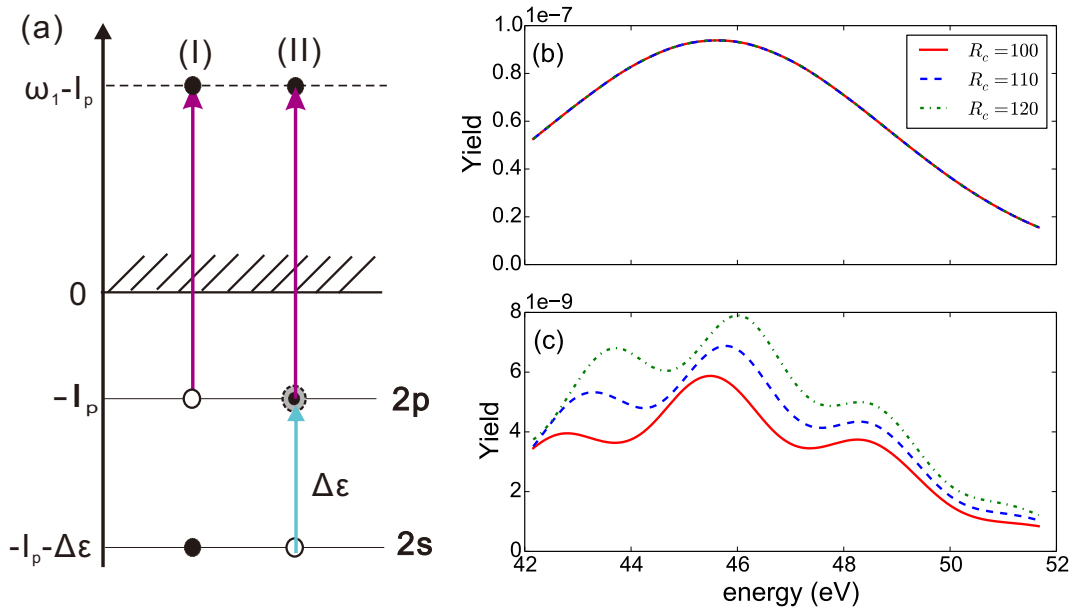

Figure 3.3: (a) Schematic of the photoelectron spectra with additional pulse with 2s-2p resonant frequency of Neon atom. (b) The numerical results from the TDCIS-tsurff integral equation (Eq. 3.68) (c) The numerical results from the TDCIS-tsurff integral equation without channel coupling term.

equation, we perform a calculation of 1D Neon atom interacting with two-color pulse with one frequency closed or equal to the Ne 2s-2p resonant energy. In Fig. 3.3 (a), the schematic of the two color XUV field ionization with one frequency equal to the Ne 2s-2p resonant energy is presented. The first XUV pulse has the frequency ω_1 = 69 eV with bandwidth 7.5 eV and directly ionizes the electron from the outer valence shell (2p), as indicated as the pathway (I). The frequency of the second XUV pulse ω_2 is set to the Ne 2s-2p resonant energy ε = 21.65 with the narrow bandwidth 0.25 eV, and this resonant pulse can transfer the hole from the outer valence shell to the inner valence shell (2s) as indicated as pathway (II). The numerical results of the photoelectron spectrum with the inner hole are presented in Fig. 3.3 (b), in which the spectra shows the peak with central energy $\omega_1 - I_p$ = 45.35 eV and does not depend on R_c. However, if the channel-coupling term is not included in the t-SURFF integral equation, the results are incorrect and strongly depend on R_c as shown in Fig. 3.3 (c). Therefore, the channel-coupling term plays an important role in Eq. 3.68 if there is a resonant field.

A similar schematic is shown but with ω_2 blue detuned away from the resonance in Fig. 3.4 (a). With the energy conservation for the two photon absorption process, the hole is moved from the $2p$ to $2s$ with additional energy transferred to the photoelectron as indicated as pathway (III). In the numerical simulation, the detuning frequency is set to be ω_d = 1 eV, which is four times larger than the bandwidth of the second pulse itself (0.25 eV) so that the resonance contribution is small. The numerical results of the photoelectron spectrum with the inner hole are presented in Fig. 3.4 (b), in which the peak is 1 eV shifted to higher energy compared with the peak in Fig. 3.4 (b). However, the results are incorrect if we remove the channel-coupling term in the t-SURFF integral equation as shown in Fig. 3.4 (c). In conclusion, the channel-coupling term is crucial if different channels are coupled via an external field, no matter this coupling is resonant or non-resonant.

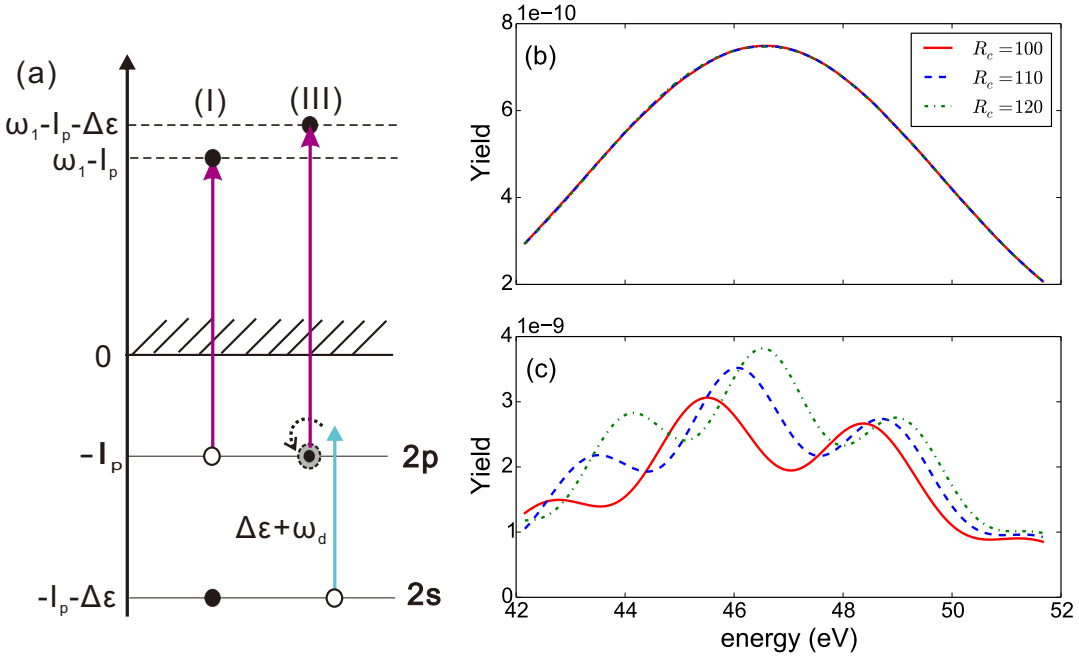

Figure 3.4: (a) Schematic of the photoelectron spectra with additional pulse with frequency blue detuned away from Neon 2s-2p excitation energy. (b) The numerical results from the TDCIS-tsurff integral equation (Eq. 3.68) (c) The numerical results from the TDCIS-tsurff integral equation without channel coupling term.

Chapter 4

XUV-assisted HHG

As discussed in 2.2, there are several ways to manipulate the HHG process from the three step model point of view. For example, using additional low frequency field can alter the classical trajectory, and furthermore break the half-cycle symmetry to enhance the even harmonics in the case of noble gas atoms [104, 105, 130–132]. We can also use additional XUV field to directly ionize the electron to continuum instead of tunneling ionization [103, 133–135]. Here, we study a two-electron scheme for the HHG process manipulated by an assisting resonant XUV pulse [136, 137]. As presented in Fig. 4.1 (a), during the excursion time of the electron from the valence shell moving in the continuum, one can excite the inner-shell electron to the vacancy with the XUV pulse. Then, the returning electron recombines into the inner-shell hole instead of the outer shell hole and leads to an increase of the energy of the emitted HHG photon. This XUV-assisted HHG provides the possibility to produce attosecond pulses at higher energy region than normal HHG as shown in Fig. 4.1 (b). The HHG spectra driven by an intense IR with (red solid line) and without (green dashed line) additional resonant XUV pulse train are compared. A second plateau is shown between about 70th to 110th harmonic, and the sharp peaks in the 67th harmonic, which corresponds to the central frequency of the XUV field, originates from the linear dipole response due to the XUV field. The laser and the atomic parameters are listed in the next paragraph. The detailed structure of the second plateau depends on the time delay between the XUV and IR fields. Unlike normal XUV-IR pump-probe measurements, the roles of each laser field in this scheme are ambiguous. The XUV pulse acts not only as a pump to trigger the hole dynamics, which is probed by the rescattering electron wave packet, but also a probe to detect the electron dynamics in continuum induced by the intense IR field.

We study this XUV-assisted HHG using TDCIS for an effective two-electron system in a 1D model of Krypton. We mimic binding energies in our 1D model of the $3d$ and $4p$ shells of Krypton, which implies an ionization potential I_p = 14.0 eV and resonant excitation energy $\Delta\varepsilon$ = 78.5 eV. In our 1D model system, the radial dipole transition matrix element is 0.354 a.u. for the hole transition, while the real $3d-4p$ transition dipole is 3.9×10^{-2} a.u. in Krypton ions. The optical laser intensity is set to 10^{14} W/cm^2 at a wavelength of 1064 nm. The XUV pulse has a Gaussian shape with a central frequency of 67 times IR-frequency, FWHM = 280 as and a peak intensity of 10^{12} W/cm^2. We study two cases: (A) few-cycle IR field + single XUV pulse and (B) flat-top IR field + XUV pulse train. An extended semiclassical model and stationary phase approximation beyond the strong field approximation (SFA) is presented to interpret the results, where the XUV field is treated as a perturbation to explain the hole dynamics on the sub-cycle time scale [136–138]. Our studies reveal discrepancies between the TDCIS calculation and the SFA model. We propose a modification of the stationary phase approximation in the extended SFA model. In the flat-top IR field + XUV APT case, the effect of the repetition of XUV pulses on the inner shell population is also discussed. The work presented in this chapter is sent for publication submitted in Phys. Rev. A[96].

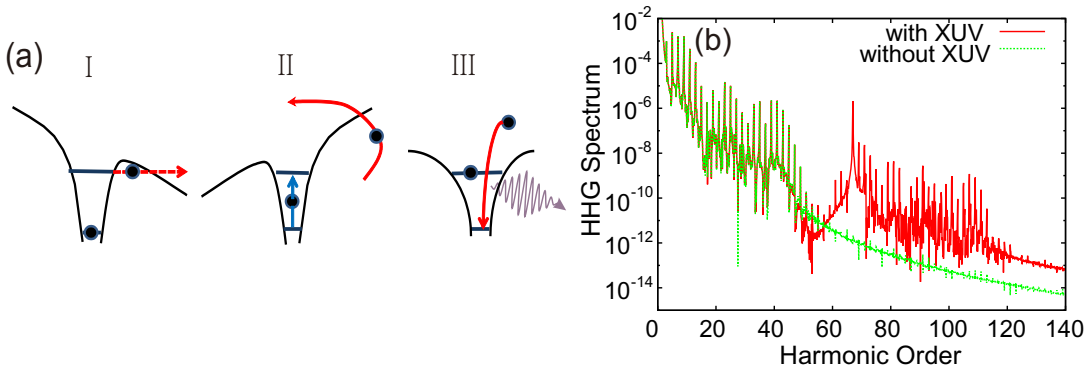

Figure 4.1: **Overview of XUV-assisted HHG scheme:** (a) Schematic of the extended three-step model of XUV-assisted HHG (b) HHG spectrum for the IR laser with (red solid line) and without (green dash line) XUV-PT.

4.1 Extended three step model

To describe the different mechanisms of the HHG photon with additional core-valence excitation, we treat the XUV field ae perturbation theory to the Lewenstein's semi-classical calculation. The strong IR field first interacts with the atom to produce an electron-hole state before the XUV resonant interaction. The other time ordering can be neglected because the IR field is incapable of pulling the highly energetic XUV-ionized electron back to produce HHG. The two-electron Schrödinger equation takes the form:

$$[\hat{H}_0 + \hat{H}_{\mathrm{IR}}(t) + \lambda\hat{H}_{\mathrm{XUV}}(t)]|\Phi(t)\rangle = i\frac{\partial}{\partial t}|\Phi(t)\rangle, \tag{4.1}$$

where $\hat{H}_0 = \hat{h}_0 \otimes \hat{\mathbb{1}} + \hat{\mathbb{1}} \otimes \hat{h}_0$ represents the the atomic electronic structure, $\hat{H}_{\mathrm{IR}} = \hat{h}_{\mathrm{IR}} \otimes \hat{\mathbb{1}} + \hat{\mathbb{1}} \otimes \hat{h}_{\mathrm{IR}} = E_{\mathrm{IR}}(t)\hat{z}_1 + E_{\mathrm{IR}}(t)\hat{z}_2$ is the interaction with the IR laser, and $\hat{H}_{\mathrm{XUV}} = \hat{h}_{\mathrm{XUV}} \otimes \hat{\mathbb{1}} + \hat{\mathbb{1}} \otimes \hat{h}_{\mathrm{XUV}} = E_{\mathrm{XUV}}(t)\hat{z}_1 + E_{\mathrm{XUV}}(t)\hat{z}_2$ is the interaction with the XUV field. Here we use capital letters to represent two-particle operators and small letters to represent one-particle operators. In the semiclassical model, we consider uncorrelated dynamics and represent the wave function as Slater determinant. The one-electron states are represented as the core state $|1\rangle$ with energy ε_1, valence state $|2\rangle$ with energy ε_2 (ionization potential $I_p = -\varepsilon_2$), and the continuum states with canonical momentum p and vector potential $A(t)$ at time t is $|k(t)\rangle = |p + A(t)\rangle$. The related transition matrix element is $\langle 2|z|1\rangle = z_{12}$, $\langle k|z|1\rangle = d_1(k)$, and $\langle k|z|2\rangle = d_2(k)$. The relevant two-particle state can be written as the ground state $|1,2\rangle = 2^{-1/2}[|1\rangle \otimes |2\rangle - |2\rangle \otimes |1\rangle]$ with energy $E_0 = \varepsilon_1 + \varepsilon_2$, the states with one electron in the momentum k and the other one in the inner shell $|1,k\rangle = 2^{-1/2}[|1\rangle \otimes |k\rangle - |k\rangle \otimes |1\rangle]$, and the states with the electron in the momentum k and the other one in the outer shell $|2,k\rangle = 2^{-1/2}[|2\rangle \otimes |k\rangle - |k\rangle \otimes |2\rangle]$.

To calculate the time dependent wavefunction, we treat the XUV interaction as a perturbation and split the wave function in the unperturbed part $|\Phi_{\mathrm{IR}}(t)\rangle$ and the perturbed part $|\Phi_{\mathrm{XUV}}(t)\rangle$:

$$|\Phi(t)\rangle = |\Phi_{\mathrm{IR}}(t)\rangle + \lambda|\Phi_{\mathrm{XUV}}(t)\rangle. \tag{4.2}$$

Here $|\Phi_{\mathrm{IR}}(t)\rangle$ satisfies the equation without the XUV field

$$i\frac{\partial}{\partial t}|\Phi_{\mathrm{IR}}(t)\rangle = [\hat{H}_0 + \hat{H}_{\mathrm{IR}}(t)]|\Phi_{\mathrm{IR}}(t)\rangle. \tag{4.3}$$

Following the derivation in Chapter 3, we can get the solution of this 0th order equation with strong field approximation:

$$|\Phi_{\mathrm{IR}}(t)\rangle \approx e^{-iE_0(t-t_0)}|\ 1,2\rangle + \int a_{1,k}(t)|1,k\rangle dk \equiv |\Phi_G(t)\rangle + |\Phi_c(t)\rangle, \tag{4.4}$$

$$a_{1,k}(t) = -i\int dt_1 e^{-i\tilde{S}_1(t,t_1,p)} \int dp\langle p + A(t)|\hat{h}_{\mathrm{IR}}(t_1)|2\rangle. \tag{4.5}$$

where $\tilde{S}_1(t,t_1,p) = \int_{t_1}^{t} dt' \frac{1}{2}[p + A(t')]^2 + \varepsilon_2(t - t_1) + E_0(t_1 - t_0)$ is the semi-classical action, and $\Phi_G(t)$ is the time dependent ground state wave function and $\Phi_c(t)$ is the time dependent continuum state wave function. To get the HHG spectrum, we need to calculate the time dependent dipole moment, neglecting the contribution from continuum-continuum interaction [13]

$$\begin{aligned}\langle\Phi(t)|z|\Phi(t)\rangle &= \langle\Phi_G(t)|z|\Phi_c(t)\rangle + \text{c.c.}\\ &= -i\int_{t_0}^{t} dt_1 \int dp\langle 2|z|p + A(t)\rangle\langle p + A(t_1)|z|2\rangle E_{\mathrm{IR}}(t_1)e^{-iS_1(t,t_1,p)} + \text{c.c.}\\ &\approx \sum_{t_i}\frac{1}{\sqrt{i}}[a_{\mathrm{ion}}(t_i,I_P)a_{\mathrm{pr}}(t,t_i,I_P)a_{\mathrm{rec}}(t,t_i,I_p)] + \text{c.c.},\end{aligned} \tag{4.6}$$

where $S_1(t,t_1,p) = \tilde{S}_1(t,t_1,p) - E_0(t-t_0) = \int_{t_1}^{t} dt' \left\{[p(t,t') - A(t')]^2/2 + I_p\right\}$ and $I_p = -\epsilon_2$ is the ionization potential. In the last line, we use the saddle point method and do the Taylor expansion near the ionization time $t_1 = t_i$ as show in Chapter 3. The integral can be factorized into several terms according to the three step model [123]. Here a_{ion}, a_{pr}, and a_{rec} represent the amplitudes of the tunneling ionization, the propagation after tunneling and the recombination. The mathematical detail of these three amplitudes were shown in Chapter 3. After the Fourier transform, we can get the unperturbed HHG spectrum.

The the wavefunction of the perturbed part $|\Phi_{\mathrm{X}}(t)\rangle$ satisfies the 1st order equation:

$$i\frac{\partial}{\partial t}|\Phi_{\mathrm{X}}(t)\rangle = [\hat{H}_0 + \hat{H}_{\mathrm{IR}}(t)]|\Phi_{\mathrm{X}}(t)\rangle + \hat{H}_{\mathrm{X}}(t)|\Phi_{\mathrm{IR}}(t)\rangle. \tag{4.7}$$

Solving the inhomogeneous differential equation (4.7) with the initial condition $|\Phi_{\mathrm{XUV}}(t_0)\rangle =$

0 at the time before the laser field, we formally get

$$|\Phi_{\mathrm{X}}(t)\rangle = -i\int_{t_0}^{t} dt' \hat{U}_{\mathrm{IR}}(t,t')\hat{H}_{\mathrm{X}}(t')|\Phi_{\mathrm{IR}}(t')\rangle, \tag{4.8}$$

where $\hat{U}_{\mathrm{IR}}(t,t') = \hat{u}_{\mathrm{IR}}(t,t')\otimes\hat{\mathbb{1}} + \hat{\mathbb{1}}\otimes\hat{u}_{\mathrm{IR}}(t,t')$ is the propagator of the unperturbed system $\hat{H}_0 + \hat{H}_{\mathrm{IR}}(t)$. We assume that the XUV field only makes the resonance transition between $|1\rangle$ and $|2\rangle$, and then the dominant dipole $d_{gx}(t) = \langle\Phi_g(t)|z|\Phi_{\mathrm{X}}(t)\rangle$ term can be approximated by the stationary approximation for $p = p_{(s)}$

$$\begin{aligned} d_{gx}(t) = &-\int_{t_0}^{t} dt_1 \int_{t_1}^{t} dt_2 \int dp \langle 1|z|p + A(t)\rangle\langle p + A(t_1)|\hat{h}_{\mathrm{IR}}(t_1)|2\rangle\langle 2|\hat{h}_{\mathrm{XUV}}(t_2)|1\rangle \\ &\times \exp\{-iS_2(t,t_2,t_1,p)\} \\ \approx &-\int_{t_0}^{t} dt_1 \mathrm{d}_2(p_s + A(t_1))E_{\mathrm{IR}}(t_1)\tilde{a}_{\mathrm{pr}}(t,t_1)\tilde{a}_{\mathrm{rec}}(t,t_1)a_{\mathrm{xuv}}(t_1,t), \end{aligned} \tag{4.9}$$

where $\tilde{S}_2(t,t_2,t_1,p) = S_1(t,t_1,p) + (\varepsilon_2 - \varepsilon_1)(t - t_2)$. Here

$$a_{\mathrm{xuv}}(t_1,t) = \int_{t_1}^{t} dt_2 z_{12} E_{\mathrm{XUV}}(t_2) e^{i\Delta\varepsilon t_2} \tag{4.10}$$

with $\Delta\varepsilon = \varepsilon_2 - \varepsilon_1$, and the propagation and recombination amplitudes are different from Eq. 3.30:

$$\begin{aligned} \tilde{a}_{\mathrm{pr}}(t,t_1) &= \left(\frac{2\pi i}{t - t_1}\right)^{1/2} e^{-iS_2(t,t_1,p_s)} \\ \tilde{a}_{\mathrm{rec}}(t,t_1) &= \mathrm{d}_1^*(p_s + A(t)) \end{aligned} \tag{4.11}$$

with $S_2(t,t_1,p_s) = S_1(t,t_1,p_s) + (\varepsilon_2 - \varepsilon_1)t$. The physical interpretation is that the outer shell electron first ionized at t_1 and then propagates in the continuum. At t_2, the inner shell electron is excited to the outer shell hole such that the electronic hole is transferred from the outer shell to the inner shell. Finally, the electron in the continuum recombines to the inner shell hole at time t. The term $a_{\mathrm{xuv}}(t_1,t)$ can be interpreted as the transition amplitude of the electron transferring from the inner orbital to the outer orbital during the time the ionized electron is in the continuum. The absolute value of a_{xuv} is the possibility of transferring an electron from the inner to the outer shell. Because we will analyze how the time delay τ, or the phase delay

$\delta \equiv 2\pi\tau/T_{\mathrm{IR}}$, between the XUV and IR field affect the HHG spectrum, a_{xuv} can be denoted as $a_{\mathrm{xuv}}(t_1, t, \tau)$ or $a_{\mathrm{xuv}}(t_1, t, \delta)$. The saddle point of S_2 gives the cut-off for the second plateau $3.17U_p + \Delta\varepsilon + 1.32I_p$. The dipole acceleration can be obtained by calculating $\langle\Phi(t)|(-\partial V(z)/\partial z)|\Phi(t)\rangle$ and the derivation does not change except for the recombination matrix element, in which the operator z is replaced by $-\partial V(z)/\partial z$.

To incorporate the XUV evolved transition in the strong-field approximation, we redefine the phase factor S_2 by moving the XUV transition matrix element into the exponent:

$$S_{2,X}(t, t_1, p_{(s)}, \tau) = S_2(t, t_1, p_{(s)}) + S_X(t, t_1, \tau), \tag{4.12}$$

where

$$S_X(t, t_1, \tau) = i \ln a_{\mathrm{xuv}}(t, t_1). \tag{4.13}$$

Then, the stationary phase requirement with respect to the ionization time t_1 yields an additional contribution $\partial S_X(t, t_1, \tau)/\partial t_1 = -i\eta(t_1, \tau)$, so that the condition of stationary phase reads

$$\left.\frac{\partial S_X}{\partial t_1}\right|_{t_{1(s)}} = -\frac{[p + A(t_{1(s)})]^2}{2} - I_p - i\eta(t_{1(s)}, \tau) = 0, \tag{4.14}$$

where

$$\eta(t_1, \tau) = \frac{1}{a_{\mathrm{xuv}}(t, t_1)} \frac{\partial a_{\mathrm{xuv}}(t, t_1)}{\partial t_1}. \tag{4.15}$$

If a_{xuv} changes slowly so that $a_{\mathrm{xuv}}(t, t_{1(s)}) \approx a_{\mathrm{xuv}}(t, t_i)$ and $\eta(t_{1(s)}, \tau) \approx \eta(t_1, \tau) \ll I_p$, the contribution of the XUV fields to the stationary phase equation Eq. 4.14 can be neglected and a_{xuv} can be treated as a constant with respect to t_1 in Eq. 4.9. The assumption of the slowly-varying function a_{xuv} mentioned above can be expressed as

$$\begin{aligned} \left|\frac{\partial a_{\mathrm{xuv}}}{\partial t_1}(t, t_1 = t_i)\right| &\ll \left|\frac{1}{\mathrm{Im}(t_{1(s)})} a_{\mathrm{xuv}}(t, t_i)\right| \\ \left|\frac{\partial a_{\mathrm{xuv}}}{\partial t_1}(t, t_1 = t_i)\right| &\ll |I_p a_{\mathrm{xuv}}(t, t_i)|, \end{aligned} \tag{4.16}$$

which indicates that a_{xuv} has to vary slowly on the time scales of the tunneling time and I_p^{-1}. It is worth noting that $\mathrm{Im}(t_{1(s)}) \approx 250$ as and $I_p^{-1} = 50$ as, and the tunneling time is larger than the period of the XUV photon. Therefore, the mathematical form of this slowly-varying function condition is similar to the slowly varying envelope approximation, in which the envelope of a forward-travelling wave pulse varies slowly

in time compared to a period. For XUV pulses satisfiying Eq. 4.16, the dipole expectation value Eq. 4.9 can then be approximated by applying a series of saddle-point approximations, similar to those that led to Eq. 4.6. In this simplified case we get

$$d_{gx}(t) \approx \sum_{t_i} a_{\mathrm{ion}}(t,t_i)\tilde{a}_{\mathrm{pr}}(t,t_i)\tilde{a}_{\mathrm{rec}}(t,t_i)a_{\mathrm{xuv}}(t,t_i). \tag{4.17}$$

The XUV resonant excitation has two major implications for the semi-classical description: the additional phase in $\tilde{a}_{\mathrm{pr}}$ representing the inner hole propagation; the addition of the transition amplitude a_{xuv}, which is a real quantity in the rotating wave approximation (RWA). If the pulse shape E_X of the XUV field $E_{\mathrm{XUV}}(t) = E_X(t-\tau)\cos[\omega_x(t-\tau)]$ is short, so that Eq. 4.16 is not satisfied, a more detailed analysis is required. For example, if the pulse shape is given by a Gaussian function

$$E_{\mathrm{X}}(t-\tau) = E_x e^{-(t-\tau)^2/\tau_x^2} \tag{4.18}$$

with central frequency $\omega_x = \Delta\varepsilon$, then

$$a_{\mathrm{xuv}}(t,t_1) \approx \frac{z_{12}E_x\tau_x e^{-i\omega_x\tau}}{2}\left[\frac{\sqrt{\pi}}{2} - \mathrm{erf}\left(\frac{t_1-\tau}{\tau_x}\right)\right] \tag{4.19}$$

where erf is the error function. In the above equation, the RWA is applied and only the negative frequency component of the XUV field is considered:

$$E^{(-)}_{XUV}(t) = \frac{1}{2}E_{\mathrm{X}}(t-\tau)\exp[-i\omega_x(t-\tau)]. \tag{4.20}$$

In the case of attosecond pulses, τ_x is small compared to the optical period and the error function grows quickly along the imaginary direction $t_{1(s)}$ when ionization time is close to the center of the XUV pulse $\mathrm{Re}(t_1) \approx \tau$:

$$\mathrm{erf}\left[i\frac{\mathrm{Im}(t_{1(s)})}{\tau_x}\right] \propto \exp\left[\left(\frac{\mathrm{Im}(t_{1(s)})}{\tau_x}\right)^2\right] \tag{4.21}$$

Therefore, a_{xuv} should be considered in the stationary phase requirement for the ionization time t_1. The stationary phase conditions are therefore strongly modified when the attosecond pulse overlaps with the IR induced ionization time. The effect of the pulse-shape of the XUV field on the stationary phase behavior and the HHG

spectrum will be discussed in the next section.

4.2 Few cycle IR field with single resonant XUV pulse

4.2.1 Comparison between TDCIS and semiclassical SFA model

When the few-cycle IR field is applied to an atomic gas, the peaks in the plateau of the HHG spectrum depend on the carrier envelope phase (CEP) of the IR field. These CEP-dependent structures can be explained as the sum of individual half-cycle bursts and were observed in the experiments [139–141]. Here, we consider the HHG spectra with a 4-cycle-pulse in addition with a single resonant XUV pulse as shown in Fig. 4.2. The red dashed line shows the HHG spectrum generated by the driving cos-like IR pulse and an XUV pulse with time delay $\tau = 0$. For comparison, the green dashed line shows the result by the same pulses with time delay $\tau = T_{\mathrm{IR}}/4$, and the blue dash-dot line shows the result for a sin-like IR pulse and an XUV pulse with zero time delay, $\tau = 0$. In addition to the normal HHG plateau, which runs up to approximately 40 harmonic orders and only depends on the CEP of the IR field. There is a second plateau that originates from the XUV resonant hole transition during the HHG process and that depends on the XUV time delay, τ. How the structure of the second plateau changes with respect to the time delay depends on the electron trajectories of the HHG process. In Fig. 4.3 (a) and (b), we show the 2D plot of HHG spectra in the second plateau region with cos-like and sin-like 4-cycle-pulse as a function of time delay, τ. Several plateaus are observed with horizontal-stripe structures. The individual plateaus appear with the brightest intensity at their corresponding lowest delay times (at the left part of each plateau).

For cos-like IR pulse case in Fig. 4.3 (a), the main second plateau (I) extends up to 110 harmonic for τ is between $-0.5T_{\mathrm{IR}}$ and $0.2T_{\mathrm{IR}}$, and up to 100 harmonic for τ is between 0 and $0.7T_{\mathrm{IR}}$. For the sin-like IR pulse case in Fig. 4.3 (b), the second plateau (IV) appears up to harmonic 110 for τ is between $-0.3T_{\mathrm{IR}}$ and $0.5T_{\mathrm{IR}}$, and up to harmonic 100 for τ is between $0.5T_{\mathrm{IR}}$ and $0.9T_{\mathrm{IR}}$. These stripe structures can be understood by analyzing the classical trajectories because the second plateau is only generated when the excursion of the electron moving in the continuum overlaps with the XUV pulse. To explain the structures we analyze the recombination energy as a function of the ionization time and recombination time that result from the unperturbed

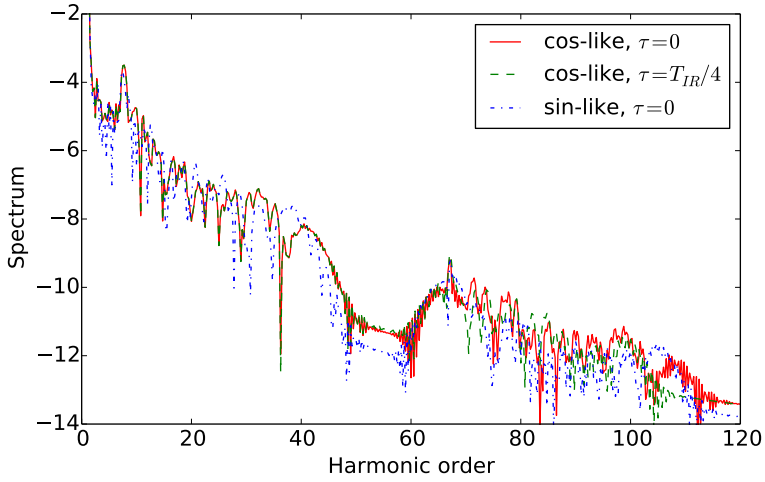

Figure 4.2: Comparison of the XUV assisted HHG spectra in logarithmic scale using different 4-cycle driving IR fields and a single XUV resonant pulse with different time delay τ: cos-like IR field, $\tau = 0$ (red solid curve); cos-like IR field, $\tau = T_{\mathrm{IR}}/4$ (green dashed curve); sin-like IR field, $\tau = 0$ (blue dot-dash curve). This figure is taken from [96]

case of an acting IR field only. Fig. 4.3 (c) and (d) plot the recombination energy as a function of a given ionization time by red dots. Because of the one-to-one mapping of ionization and recombination times as indicated in Chapter 2, the recombination energy as a function of recombination time can be plotted by the green dots in Fig. 4.3 (c) and (d). The horizontal-stripe structures and the corresponding classical trajectories that are mainly allowed are both labelled as I-V. For example, if the time delay of the XUV pulse falls in between the ionization and recombination times for the cutoff trajectories I, the plateau region I in Fig. 4.3 (a) is generated. Likewise the cutoff trajectories of region II are marked in Fig. 4.3 (c). A similar analysis holds for the sin-like IR pulse shown in Fig. 4.3 (b) and (d). Furthermore, the recombination time as function of electron returning energy is shown as the green dashed lines in 4.3 (a) and (b). When the XUV pulse only overlaps with the excursion of long trajectories, the interference between long and short trajectories is closed such that the peak structures disappear in the area indicated as A-C. Therefore, the cutoff energy and the peak structures of the second plateau reveal directly the excursion time of the electron trajectories in the strong laser field. This idea can give us an one-to-one mapping from the HHG spectrum

to the CEP of a few cycle pulse. Our results can give access to the time resolved dynamics and provide us a tool for retrieval of intense few-cycle IR pulse structures by the resonant XUV probe pulse. This kind of XUV-probe HHG spectroscopy can help us to resolve some processes and configurations without the emission of photo- or Auger-electrons [142].

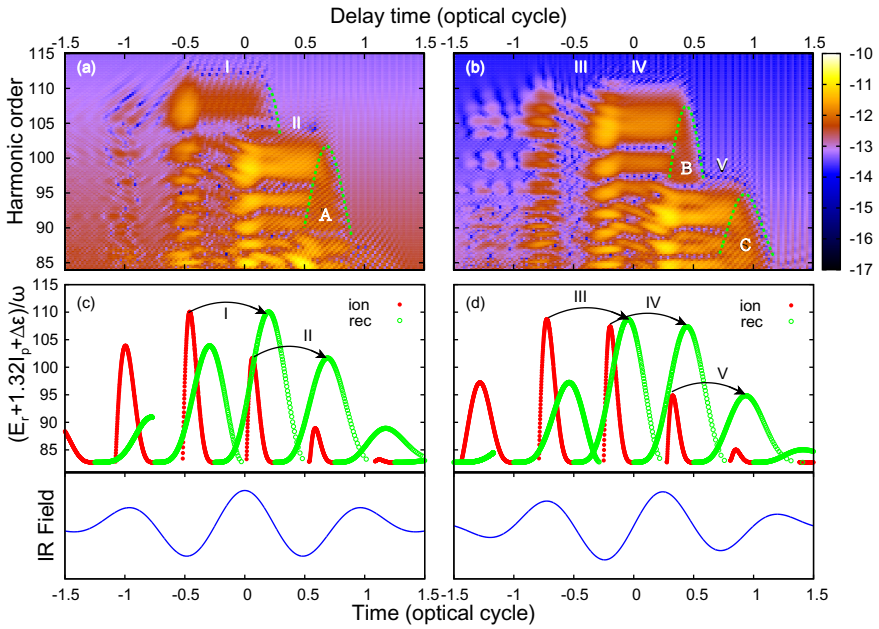

Figure 4.3: The upper panels are HHG power spectra for (a) cos-like and (b) sin-like short IR laser fields with a single XUV pulse. The lower panels are the return energy (in terms of the harmonic order with recombination to the inner shell) plotted as a function of the ionization time (red filled circles) and the recombination time (green open circles). The blue curves in the lower panels are the corresponding IR field: cos-like (left) and sin-like (right). The arrows in (c) and (d) are the classical trajectories mainly allowed and labelled with I-V. This figure is taken from [96]

To understand the structures, we perform the SFA calculation for the cos-like IR field case. The dipole expectation value with approximation according to Eq. 4.9 and Eq. 4.10 for a_{xuv} leads to Fig. Fig. 4.4 (c). The dipole moment calculation with approximation according to Eq. 4.17 and the slowly-varying function approximation in a_{xuv} indicated as Eq. 4.16 leads to Fig. 4.4 (a). Both of these two plots show fast background oscillation as the same as Fig. 4.3 (a) and (b). It is not surprising because

$a_{xuv}(t_1, t, \tau)$ contributes a phase factor $\omega_x \tau$ from the time delay of the XUV pulse. The interference between the $\langle \Phi_G(t)|z|\Phi_{\mathrm{XUV}}(t)\rangle$ and its complex conjugate will introduce the τ-dependent phase $2\omega_x\tau$, which results in signal modulation with respect to τ in the background. This background oscillation can be eliminated with RWA, in which $\langle \Phi_{\mathrm{XUV}}(t)|z|\Phi_G(t)\rangle$ and the positive frequency component $E^{(+)}_{\mathrm{XUV}}$ of E_{XUV} are removed, as shown in Fig. 4.4 (b) and (d).

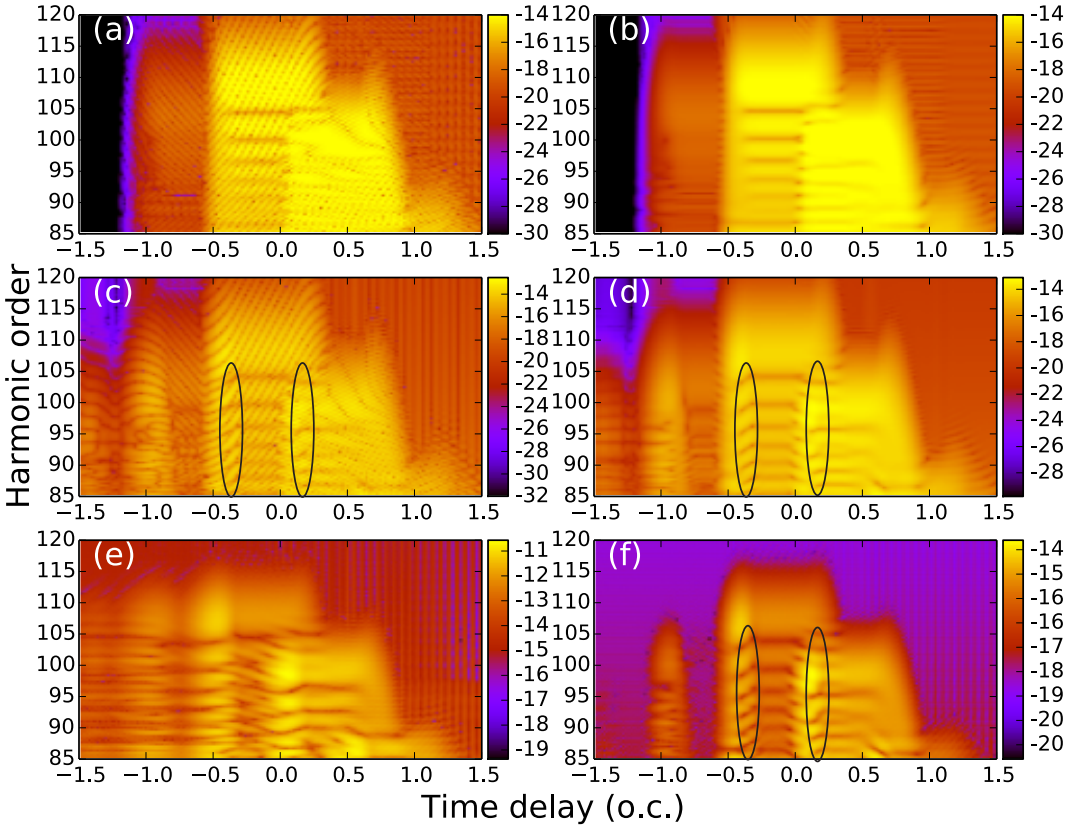

Figure 4.4: The 2D plot of HHG spectra for the cos-like 4 cycle IR laser field with single XUV pulse as a function of time delay in the second plateau region: (a) SFA with SPA for both p and t_1. (b) SFA with SPA for both p and t_1 with rotating wave approximation. (c) SFA with SPA for p (b) SFA with SPA for p with rotating wave approximation on. (e) Independent particle approximation with the use of short range potential with more than two bound states. (f) Independent particle approximation with the use of short range potential with only two bound states. This figure is modified from [96]

Although the horizontal shape of the delay-dependent HHG spectra are well captured by the SFA, the details of the substructures inside the horizontal stripes are different between the TDCIS calculation and the SFA calculation. In the case of SFA with dipole moment according to Eq. 4.9, shown in Fig. 4.4 (c) and (d), the local minima of the second plateau show positive slopes as a function of time delay fo delay times around $\tau = -0.4T_{\mathrm{IR}}$ and $0.1T_{\mathrm{IR}}$ as indicated by the regions marked with the black ellipse. In the TDCIS calculation, shown in Fig. 4.3, there are more complex substructures. To clarify the origin of the discrepancy between TDCIS calculation and SFA calculation, we simplify our TDCIS to the independent particle approximation (IPA) with the use of short range potential to more closely adapt the assumption of the SFA. Here we use two kinds of short range potentials: $V(x) = Ze^{-ax^2}$ with $Z = 5.38$ and $a = 2.03$ resulting in only two bound states [Fig. 4.4 (e)]; $V(x) = Ze^{-ax^2}/\sqrt{x^2+b^2}$ with $Z = 1.07$, $a = 0.01$ and $b = 0.702$ resulting in more than two-bound states. In the IPA with two bound states only, the pattern shown in the black ellipse in Fig. 4.4 (f) is similar to the one in Fig. 4.4 (c) and (d). On the contrary, when the short range potential supporting more than two bound states is used, a more complex interference structure in the plateaus is visible, as shown in Fig. 4.4 (e). Thus, we argue that the complex interferences in the lower energy part of the plateaus in Fig. 4.3 (a) are due to bound excited state population, while the more energetic part of the plateaus are well described by the SFA model and exhibit (i) clear horizontal stripes and (ii) a positive slope on the left side of the plateaus Fig. 4.3 (a) and (b). We have found that the detailed structures in the plateaus are independent of the depletion of the ground state by direct ionization with the XUV field by setting the XUV field equal to zero in the term coupling the ground state to the continuum state of the TDCIS (Eq. 3.2),i.e.,

$$i\dot{\alpha}_0 = -E_{\mathrm{IR}}(t)\sum_i \langle\varphi_i|\hat{z}|\chi_i,t\rangle. \tag{4.22}$$

Moreover, the fine structure in the plateaus is not affected by turning off the XUV interaction term in Eq. 3.50,i.e., solving

$$\begin{aligned} i\frac{\partial}{\partial t}|\chi_i\rangle =& (\hat{H}_0 - \varepsilon_i)|\chi_i\rangle + \sum_{i'}\hat{P}\{\hat{K}_{i'i} - \hat{J}_{i'i}\}|\chi_i'\rangle - E_{\mathrm{IR}}(t)\hat{P}\hat{z}\{\alpha_0|\varphi_i\rangle + |\chi_i\rangle\} \\ &+ [E_{\mathrm{IR}}(t) + (\delta_{i1}\delta_{i'2} + \delta_{i2}\delta_{i'1})E_{\mathrm{XUV}}(t)]\sum_{i'} z_{i'i}|\chi_{i'}\rangle. \end{aligned} \tag{4.23}$$

Here the term $\delta_{i1}\delta_{i'2} + \delta_{i2}\delta_{i'1}$ couples the XUV field to only the core-valence transition. We can conclude that the structure is not resulting by inter-channel couping mediated by the XUV field. Therefore, any bound excited state population is a result of strong field excitation by the IR field rather than the coupling with the XUV field, at least at the considered XUV intensities.

4.2.2 Modified tunneling time in the SFA

If a_{xuv} is assumed to be slowly varying, i.e. if we adopt the approximation for the dipole moment of Eq. 4.17, then the stripes at delay times of around $\tau = -0.45T_{\mathrm{IR}}$ and $-0.35T_{\mathrm{IR}}$ with positive slopes vanish, as shown in Fig. 4.4 (a) and (b). These time delays τ are close to the ionization time t_i of the classical trajectories. Clearly, to fully explain the structure of positive slopes structure of positive slopes marked by the black ellipses in Fig. 4.4 (c), (d) and (f), the phase contribution $S_X(t, t_1, \tau)$ has to be taken in the stationary phase approximation. To solve the stationary phase equation (Eq. 4.14), we expand the equation into Taylor series around t_i:

$$
\begin{aligned}
&\left.\frac{\partial S_{2,X}(t, t_1, p_{(s)})}{\partial t_1}\right|_{t_1 = t_{1(s)}} \\
=&\left.\frac{\partial S_{2,X}}{\partial t_1}\right|_{t_1=t_i} + \left.\frac{\partial^2 S_{2,X}}{\partial t_1^2}\right|_{t_1=t_i}(t_{1(s)} - t_i) + \frac{1}{2}\left.\frac{\partial^3 S_{2,X}}{\partial t_1^3}\right|_{t_1=t_i}(t_{1(s)} - t_i)^2 \\
=&-I_p - i\eta_0 - i2\eta_0^2(t_{1(s)} - t_i) + \left[-\frac{1}{2}|E(t_i)|^2 - i4\eta_0^3 + i\frac{4\eta_0}{\tau_x^2}\right](t_{1(s)} - t_i)^2 \\
=&0.
\end{aligned}
\tag{4.24}
$$

In the above equation, we assume that t_1 is closed to τ, so the $\eta(t_1, \tau)$, its first order, and second order derivative can be approximated by

$$
\eta(t_1, \tau) \approx \eta_0 + \eta_0^2(t_1 - \tau) + \left(\eta_0^3 - \frac{\eta_0}{\tau_x^2}\right)(t_1 - \tau)^2 \tag{4.25}
$$

$$
\frac{\partial \eta}{\partial t_1} \approx \eta_0^2 + 2\left(\eta_0^3 - \frac{\eta_0}{\tau_x^2}\right)(t_1 - \tau) \tag{4.26}
$$

$$
\frac{\partial^2 \eta}{\partial t_1^2} \approx 2\eta_0^3 - 2\frac{\eta_0}{\tau_x^2} \tag{4.27}
$$

where $\eta_0 = \eta(\tau,\tau)$. This constant $\eta_0 \propto \tau_x$ reveals the XUV pulse-duration dependence. With the use of infinite pulse duration, or a cw XUV field, $\eta_0 \approx 0$ so that the stationary equation reduces to that for the normal HHG. By solving the above stationary phase equation, the solution

$$t_{1(s)} = t_i - \frac{i2\eta_0^2 \pm \sqrt{-4\eta_0^4 - 2[|E(t_i)|^2 + i8\eta_0^3 - i8\eta_0/\tau_x^2][I_p + i\eta_0]}}{|E(t_i)|^2 + i8\eta_0^3 - i8\eta_0/\tau_x^2} \tag{4.28}$$

is obtained. The value of the solution determined by the laser parameters we use is $t_{1(s)} - t_i = 1.91 + 15.2i$ or $4.72 - 19.8i$, and the solution in the upper complex plane should be chosen so that the integration can results into a simple Gaussian integral along a suitable contour, which is parallel to real the axis. Compared with the original complex ionization time $t_{1(s)} = t_i + \sqrt{2I_p}/|E(t_i)|$, which leads to $t_{1(s)} - t_i = \pm 24.0i$ at the peak intensity, the new term S_X changes both the real part and imaginary part of the complex ionization time. The modified tunneling time, which is the imaginary part of the complex ionization time, has a calibration of about 250 as from the original tunneling time. Compared to the imaginary part, $\mathrm{Re}(t_{1(s)})$ does not deviate from t_i much, so we can assume $\mathrm{Re}(t_{1(s)}) = t_i$. Then the time integration of hole transfer amplitude

$$a_{xuv}(t_r, t_{1(s)}, \tau) \approx \frac{e^{i\omega_x \tau}}{2} \int_{t_{1(s)}}^{t_r} dt_2 E_X(t_2 - \tau) \tag{4.29}$$

inside $S_X(t_r, t_{1(s)}, \tau)$ can be split into two parts $a_{xuv}(t_r, t_i, \tau) + a_{xuv}(t_i, t_i + i\mathrm{Im}(t_{1(s)}), \tau)$: the resonant hole transfer during the electron in the continuum

$$\begin{aligned} a_{xuv}(t_r, t_i, \tau) &\approx \frac{e^{i\omega_x \tau}}{2}\left[\int_{\tau}^{t_r} dt_2 E_X(t_2 - \tau) - E_X(0)(t_i - \tau)\right] \\ &= \frac{e^{i\omega_x \tau}}{2}\left[\frac{\tau_x\sqrt{\pi}}{2} - (t_i - \tau)\right], \end{aligned} \tag{4.30}$$

in which the integration is dealt with the first-order Taylor series for t_i around $t_i = \tau$; and the resonant excitation during the tunneling process

$$\begin{aligned} & a_{xuv}(t_i, t_i + i\mathrm{Im}(t_{1(s)}), \tau) \\ \approx & \frac{e^{i\omega_x \tau}}{2}\left[\int_{t_{1(s)}}^{t_i} dt_2 E_X(t_2 - t_i) + \int_{t_{1(s)}}^{t_i} dt_2 \frac{\partial E_X(t_2 - \tau')}{\partial \tau'}\bigg|_{\tau'=t_i} (\tau - t_i)\right] \\ = & \frac{e^{i\omega_x \tau}}{2}\left[-i\int_0^{\mathrm{Im}(t_{1(s)})} dt_1' \exp\left(\frac{t_1'^2}{\tau_x^2}\right) + \left\{\exp\left[\frac{(\mathrm{Im}(t_{1(s)}))^2}{\tau_x^2}\right] - 1\right\}(\tau - t_i)\right], \end{aligned} \tag{4.31}$$

in which the second line is the result of the first-order Taylor series for τ around $\tau = t_i$. Here the XUV pulse is assumed to be a Gaussian shape (Eq. 4.18) and τ_x is assumed to be much smaller than the duration of the trajectory so that the interval of integration in Eq. (4.30) can be replaced by $[\tau, \infty]$. With the above expression, this complex transition amplitude can be approximated by $a_{xuv}(t_r, t_{1(s)}, \tau) \approx e^{i\omega_x \tau}(R + iI)/2$, where

$$R = \frac{\tau_x\sqrt{\pi}}{2} + \exp\left[\frac{(\mathrm{Im}(t_{1(s)}))^2}{\tau_x^2}\right](\tau - t_i) \tag{4.32}$$

and

$$I = -i\int_0^{\mathrm{Im}(t_{1(s)})} dt_1' \exp\left(\frac{t_1'^2}{\tau_x^2}\right). \tag{4.33}$$

With the above expression, Eq. 4.13 can be written as

$$S_X(t_r, t_{1(s)}, \tau) = i\left[\ln z + \frac{\pi}{2}i + \ln\sqrt{R^2 + I^2} - i\arctan\frac{R}{I} + i\omega_x\tau\right]. \tag{4.34}$$

It is worth noting that the transition amplitude of the hole transfer by the XUV field during the quantum tunneling makes the phase $\mathrm{Re}(S_X(t_r, t_{1(s)}, \tau))$ different from $\mathrm{Re}(S_X(t_r, t_i, \tau)) = -\omega_x\tau$. In the case $\tau = t_i$, $R \approx 10.4$ is smaller than the absolute value of the I, which is about 30.5, so we can apply the approximation $\arctan(R/I) \approx R/I$ and the additional dipole phase contributed from the hole transfer during the tunneling is

$$\mathrm{Re}(S_X(t_r, t_{1(s)}, \tau)) - \mathrm{Re}(S_X(t_r, t_i, \tau)) \approx -\frac{\pi}{2} + \frac{R}{I} = -A - B(\tau - t_i), \tag{4.35}$$

where

$$A = \frac{\pi}{2} + \frac{\tau_x\sqrt{\pi}}{2\int_0^{\mathrm{Im}(t_{1(s)})} dt_1' \exp\left(\frac{t_1'^2}{\tau_x^2}\right)} \tag{4.36}$$

and

$$B = \frac{\exp\left[\frac{(\mathrm{Im}(t_{1(s)}))^2}{\tau_x^2}\right]}{\int_0^{\mathrm{Im}(t_{1(s)})} dt_1' \exp\left(\frac{t_1'^2}{\tau_x^2}\right)}. \tag{4.37}$$

Therefore, when the XUV pulse sets in the vicinity of the start of the classical trajectory, there is an additional phase which is linear to the time delay τ. When the XUV pulse is far away from the ionization, $\eta(t_1, \tau)$ is close to zero so that the stationary phase behavior is independent of τ. The interference pattern in the second plateau originates from the interference between short and long trajectories. In this case the additional τ-dependent phase in Eq. 4.35 can be resolved as shown in Fig. 4.5 showing a zoomed-in region of Fig. 4.4 (d). In Fig. 4.5, the black dotted curve shows the energy of the emitted harmonics as a function of ionization time. When τ is close to t_i^s, the ionization time of the short trajectories, the phase of the HHG interference pattern is

$$-\Omega(t_r^l - t_r^s) + S_2(t_r^l, t_i^l, p_{(s)}) - S_2(t_r^s, t_i^s, p_{(s)}) + A + B(\tau - t_i^s), \tag{4.38}$$

where the superscript l and s label the long and short trajectories respectively. Here the resonant excitation does not happen for the long trajectory due to the non-overlapping between the XUV field and t_i^l, so

$$\mathrm{Re}(S_X(t_r^l, t_{1(s)}^l, \tau)) = \mathrm{Re}(S_X(t_r^l, t_i^l, \tau)) = -\omega_x \tau. \tag{4.39}$$

Therefore, the valleys of the HHG signal show linear drift with positive slopes $B/(t_r^l - t_r^s)$ indicated by green dashed lines in Fig. 4.5 and these lines fit well with local minima of the data shown in darker color. However, when τ is close to t_i^l, the interference pattern disappears because the XUV pulse comes before the production of the short trajectory.

How the complex ionization time changes according to Eq. 4.28 is shown in Fig. 4.6. The electric field is chosen to be at the peak of the IR field in our calculation. The unmodified ionization time $t_{1(s)} = t_i + \sqrt{2I_p}/|E(t_i)|$, which corresponds to $\eta_0 = 0$ and the use of a cw XUV field, is shown as blue triangle. As η_0 increases, the tunneling time (imaginary part of η_0) approaches 0 and $t_{1(s)}$ converges to the ionization time t_i predicted by three step model t_i. The green diamond indicates the value with $\eta_0 = 0.095$, which is the condition used in our calculation, and we assume that $\mathrm{Re}(t_{1(s)}) \approx 0$ in the analysis for $a_{xuv}(tr, t_{t_{1s}}, \tau)$ to get a good agreement for the explanation of the structures in Fig. 4.5. However, this assumption is not always valid because $\mathrm{Re}(t_{1(s)}) - t_i$ can be as

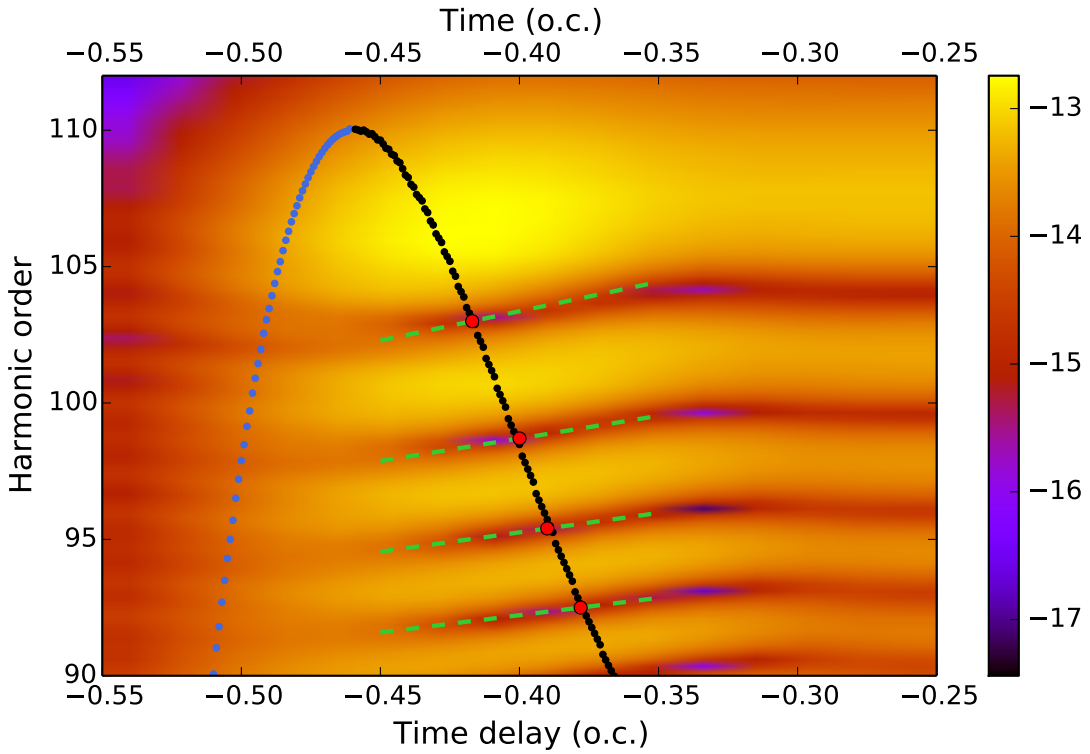

Figure 4.5: A zoom-in region of Fig. 4.4 (d) shown for $\tau \approx -0.4$, where the stripe structure shows a positive slope. The dotted curve shows the emitted photon energy in the second plateau as a function of ionization time. Long trajectories, with ionization times earlier than the cut-off trajectories are marked in blue, and short trajectories are marked in black. The green dashed lines are the interference pattern predicted by Eq. 4.38 around $\tau \approx t_i$. This figure is taken from [96]

large as half of the imaginary part. In this case, a modified real ionization time as well as a modified tunneling time should be considered and the analysis for $a_{xuv}(tr, t_{t_{1s}}, \tau)$ would be more complicated.

It is worth noting that if a cw XUV pulse is used, the XUV resonant excitation mainly happens during the electron excursion. In this case the slowly varying XUV amplitude approximation is certainly valid. However, if the XUV pulse is short and if it overlaps with the start of an electron trajectory, the effective tunneling time may change and the laser-assisted HHG is enhanced, c.f. Fig. 4.3 (a) and (b), where the plateaus are brighter on the left side. This effect and the positive slopes of the interference between short

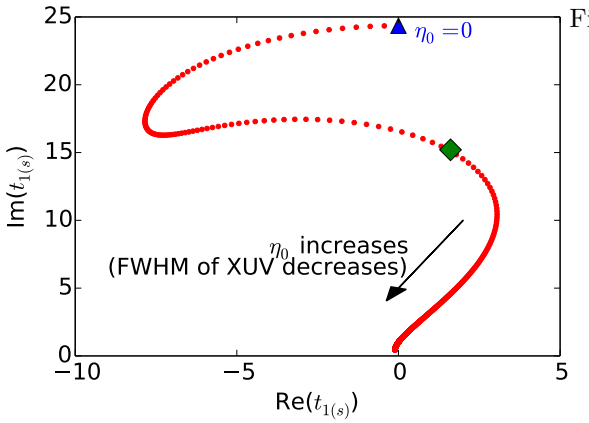

Figure 4.6: The complex ionization time $t_{1(s)}$ changes when η_0 increases. The electric field is chosen to be the peak amplitude of IR field in our TDCIS calculation. The blue triangle is the unmodified value of $t_{1(s)}$ (in the case $\eta_0 = 0$). The green diamond is the value in our case $\eta_0 = 0.095$.

and long trajectories demonstrate the *invalidity of the slowly-varying approximation* of a_{xuv} and it presents a complication to probe the exact tunneling and return times of electrons in situ in a strong laser field by a single attosecond pulse. The situation is quite similar to other cases where classical pictures are used as a starting point for perturbative expansions of the SFA. For example, the one-color SFA was perturbed by a weak second harmonics field for the purpose of in situ characterization of attosecond pulses. If one assumes classical trajectories, the second harmonic contributes only a phase correction in the action [143]. However, using more refined quasi-classical trajectories shows that also the tunneling processes is modified by the second harmonic field and that the behavior of the high-order even harmonics is not well suited for pulse characterization [144].

4.3 Long IR pulse with resonant XUV pulse train

When an XUV-PT is applied in addition to a driving IR field for the HHG, the repetition of the XUV pulse can coherently increase the inner shell hole population. Consecutive individual bursts of the XUV-PT produced via HHG are separated by half cycles $T_{\mathrm{IR}}/2$ of the driving laser field as shown in Fig. 4.7 and have a relative carrier envelope offset (CEO) $\Delta\phi_c = \pi$:

$$E_{\mathrm{XUV}}(t) = \sum_m E_{\mathrm{X}}(t-\tau_m)\cos[\omega_x(t-\tau_m) - m\Delta\phi_c], \tag{4.40}$$

where $\tau_m = \tau + mT_{\mathrm{IR}}/2$ and m is an integer.

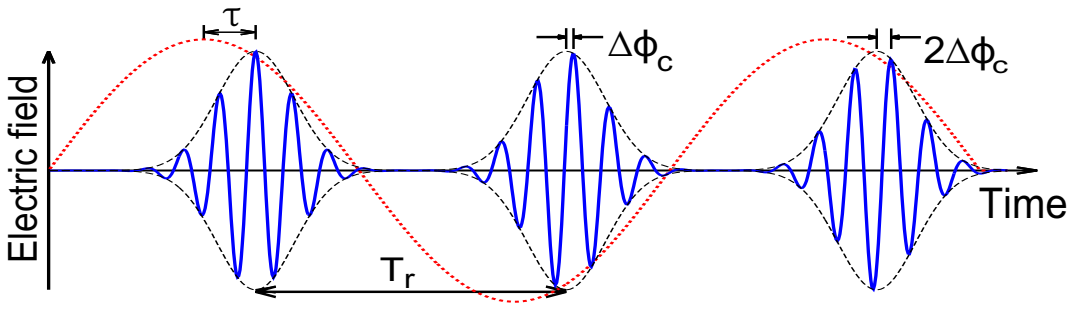

Figure 4.7: Electric field of the IR field (red dash-dotted line) and an XUV pulse train (blue solid line). If the XUV pulse train is generated via HHG in atomic gas, then $\Delta\phi_c = \pi$ and the the repetition period is equal to half cycles of IR field, $T_r = T_{\mathrm{IR}}/2$. This figure is taken from [96]

The resulting second plateau of the HHG spectrum is shown in Fig. 4.8 (a). Here on the x-axis, we define the phase delay $\delta \equiv 2\pi\tau/T_{\mathrm{IR}}$, which is directly linked to the time delay of the IR peak intensity to the envelope of the as pulse. Like the first plateau, the second plateau also contains only odd harmonic orders. There is a π phase shift of the same classical trajectories with the opposite kinetic momentum in adjacent half cycles due to the sign-change of the monochromatic driving IR field

$$E_{\mathrm{IR}}(t + \frac{T_{\mathrm{IR}}}{2}) = -E_{\mathrm{IR}}(t). \tag{4.41}$$

Here, both the dipole transition with the pulse train

$$z_{12}E^{(-)}_{\mathrm{XUV}}(t + \frac{T_{\mathrm{IR}}}{2}) = z_{12}E^{(-)}_{\mathrm{XUV}}(t)e^{i\Delta\phi_c} \tag{4.42}$$

and the opposite parity between the inner and the outer shell

$$d_1^*(-k')d_2(-k) = -d_1^*(k')d_2(k) \tag{4.43}$$

induce additional π phase shifts in the trajectories giving rise to the second plateau in the next half cycle. Therefore, the net phase difference between the pathway from two adjacent half cycles is π, which results in destructive interference in the even harmonics. Moreover, the HHG spectrum exhibits a phase-delay dependence. When the peak of the XUV pulse is in the second and fourth quarter cycle ($\delta > 0$), the spectrum shows

higher intensity. The inner shell hole population $\rho_1(t)$ in Fig. 4.8 (c) also shows higher population in the same region. This can be understood by analyzing $|a_{\mathrm{xuv}}(t, t_i, \tau)|^2$, the transition probability of the hole from the outer shell to the inner shell for each trajectory for $t \in [t_i, t_r]$. Here we take $\delta = 0.15\pi$ and -0.15π, which are indicated as white line in Fig. 4.8, and the cutoff trajectory, $[t_{i,\mathrm{cutoff}} = 0.29T_{\mathrm{IR}}, t_{r,\mathrm{cutoff}} = 0.958T_{\mathrm{IR}}]$, as an example in Fig. 4.9 (a) and (b). The blue straight lines indicate the start and the end of the cutoff trajectory. The green fast oscillating curves are the XUV pulses in the time domain for the case $\delta = 0.15\pi$ in (a) and $\delta = -0.15\pi$ in (b). For $\delta = 0.15\pi$, there is only one XUV pulse in the time interval $[t_{i,\mathrm{cutoff}}, t_{r,\mathrm{cutoff}}]$, so the transition probability increases during the XUV field as indicated by the red increasing curve in Fig. 4.9 (a) and $|a_{\mathrm{xuv}}(t_{r,\mathrm{cutoff}}, t_{i,\mathrm{cutoff}}, \tau)|^2 \approx \gamma$, where

$$\gamma = \frac{1}{4}\left| z_{12} \int_{-\infty}^{\infty} dt' E_{\mathrm{X}}(t' - \tau) \right|^2 \tag{4.44}$$

For $\delta = -0.15\pi$, there are two XUV pulses in the time interval $[t_{i,\mathrm{cutoff}}, t_{r,\mathrm{cutoff}}]$. We assume that the pulse duration is short enough so that both of these two pulses are limited in this time interval. The final transition probability is the coherent sum of the transition amplitudes of the contribution from each of the XUV pulses and can be written as

$$\begin{aligned} |a_{\mathrm{xuv}}(t_{r,\mathrm{cutoff}}, t_{i,\mathrm{cutoff}}, \tau)|^2 &\approx \gamma |1 + e^{i(\Delta\phi_c + \Delta\varepsilon T_{\mathrm{IR}}/2)}|^2 \\ &= \gamma |1 + e^{i(\Delta\phi_c + \pi)}|^2. \end{aligned} \tag{4.45}$$

Here π in the second line is derived from the phase difference between the two levels due to the free propagation, and can be canceled out by $\Delta\phi_c = \pi$. Therefore, the transition amplitudes contributing from the two adjacent XUV pulses are constructively added so that the time dependent transition probability doubles as indicated by the red increasing curve in Fig. 4.9 (b). To confirm this argument, we choose the other case $\Delta\phi_c = 0$ so that π phase difference due to the free propagation cannot be canceled out. In this case, we will get the results with the opposite tendency. When $\delta = 0.15\pi$, there is only one XUV pulse in the time interval $[t_{i,\mathrm{cutoff}}, t_{r,\mathrm{cutoff}}]$ as shown in Fig. 4.9 (c), so the behavior of the transition probability indicated by the red increasing curve is the same as the $\Delta\phi_c = \pi$ case. When $\delta = -0.15\pi$, the transition probability increases during

the first XUV pulse and then decreases during the second XUV pulse as shown in Fig. 4.9 (d). Therefore, this destructive mechanism reflects lower yields at $\delta = -0.15\pi$ than at $\delta = 0.15\pi$ on both HHG spectra and inner shell hole population $\rho_1(t)$ shown in Fig. 4.8 (b) and (d). In addition, the second plateau shows even harmonics instead of odd harmonics as shown in Fig. 4.8 (b) because $\exp(i\Delta\phi_c)$ in Eq. 4.42 turns out to be 1 rather than −1. Consequently, changing the time delay of the XUV pulse means the control of hole transfer during the HHG process and the electron-ion rescattering event can probe by this hole dynamics. The concept of coherent population transfer in a two-level system with a train of ultrashort laser pulses has already been studied for long time in different systems [145] and gives a good explanation here for our results.

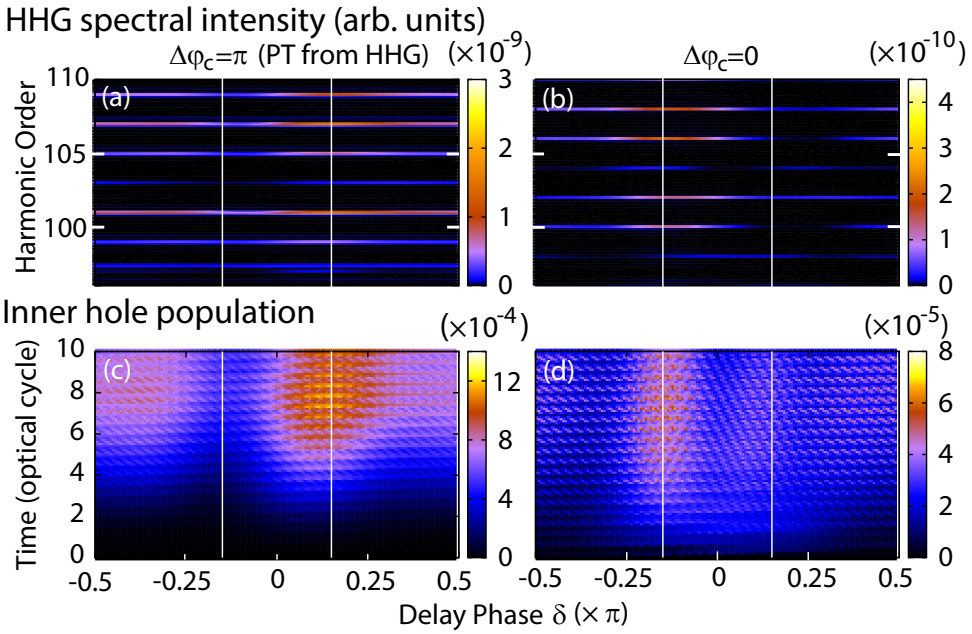

Figure 4.8: The HHG in the second plateau region with two different kinds of XUV pulse train, $\Delta\phi_c$ is $\pi/2$ (left) and 0 (right), as a function of delay phase δ. (a)(b) are HHG power spectra in acceleration form. (c)(d) are inner shell population $\rho_{3d}(t)$ as the function of delay phase δ. The white lines on $\delta = -0.15\pi$ and $\delta = 0.15\pi$ indicate the local maximum and minimal area of the HHG spectrum. This figure is taken from [96]

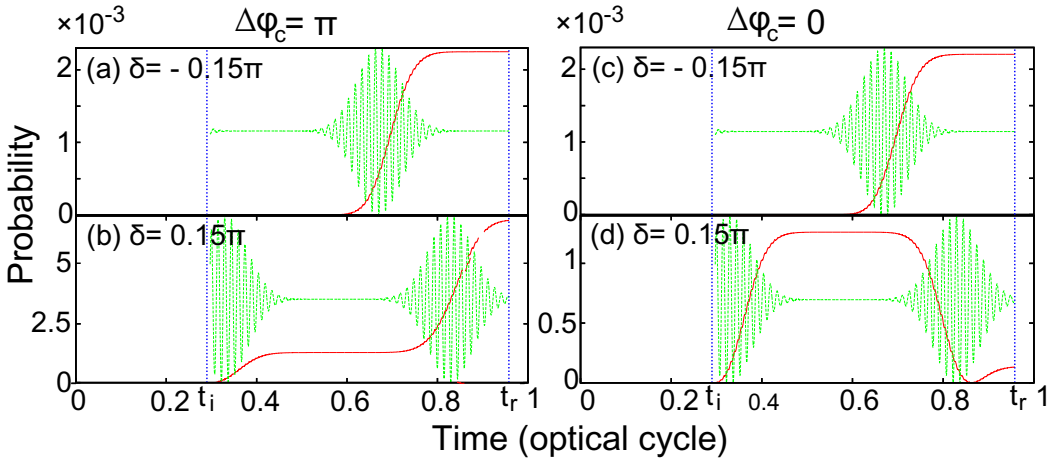

Figure 4.9: $|a_{\mathrm{xuv}}(t_i, t, \delta)|^2$ curve (red lines) from $t = t_i$ to t_r (blue dash line) for XUV pulse trains (green curves) with $\Delta\phi_c = \pi$ (left) and $\Delta\phi_c = 0$ (right). The δ is chosen -0.15π and 0.15π (white lines in Fig. 4.8). When $\delta = -0.15\pi$, the parent ion interacts with the XUV-PT once and both of these two cases show the same curve in (a) and (c). When $\delta = 0.15\pi$, the parent ion interacts with the XUV-PT twice and different CEO show different features on the curves in (b) and (d). This figure is taken from [96]

Chapter 5

Characterizing attosecond pulses with the electron hole transitions

As we mentioned in Chapter 2, the attosecond streaking and other similar XUV-pump-IR-probe method are powerful tools for characterization of XUV attosecond pulses by analyzing photoelectrons by a phase-locked IR laser field. In this scheme, the photoelectron is treated as a replica of the XUV attosecond pulses and controlled by the IR field. However, in this kind of scheme based on above-threshold ionization (ATI), the IR field coupling with the ionic potential induces some additional phase shifts, or response times [38, 55, 57]. In the small kinetic energy region of the wavepacket, this response time can even reach hundreds of attoseconds and affect the accuracy of the measurement. To overcome this obstacle, we propose a scheme which is called Stimulation of Two Resonant and Instantaneously Detuned Electron Replicas (STRIDER). Most of the work in this chapter is published in [95].

5.1 Theory of STRIDER method

In STRIDER, we spectrally shear the photoelectrons using two coherent XUV fields that stimulate hole dynamics in the residual ion, following photoionization with the XUV attosecond pulse, as shown in Fig. 5.1 (a). The pump pulse $E_1(t)$ is broadband with central frequency ω_1 and unknown spectral phase $\phi_1(\omega)$ (or group delay $d\phi_1/d\omega$):

$$E_1(t) = \frac{1}{2\pi}\int d\omega |\tilde{E}_1(\omega)| e^{i[\phi_1(\omega)-\omega t]}. \tag{5.1}$$

The goal of the STRIDER method is to reconstruct the unknown spectral phase of the attosecond pulse. The probe fields

$$E_{2,3}(\omega) = \tilde{E}^{(0)}_{2,3}\delta(\omega - \omega_{2,3}) \tag{5.2}$$

with $\tilde{E}^{(0)}_{2,3} = |\tilde{E}^{(0)}_{2,3}|\exp[i\phi_{2,3}]$, and frequencies $\omega_{2,3}$ are symmetrically red and blue detuned by $\delta\omega$ from the hole transition in order to introduce spectral shearing of the photoelectrons to lower and higher kinetic energies, respectively. Due to the interference of the two pathways by the two probe fields, shown in Fig. 5.1 (a), the signal of the photoelectron spectra with an inner shell hole changes with the relative phase between the two probe pulses. In this scheme, the detuning energy here plays a similar role as the IR frequency in the streaking measurement, and the continuum-continuum dipole transition induced by the IR field is replaced by the bound state transition. It is important to note that we consider photoelectron spectra from particular ionic channels and assume that the state of the ion is measured in coincidence with the photoelectron.

The perturbation theory for light-atom interactions for one-electron systems is introduced in Chapter 2. In order to derive the equations for the STRIDER method, which is based on both the ionized electron and the ionic state, many-body wavefunctions are needed to describe the different ionic channels. We consider a 3-level many-electron system consisting of the HF ground state $|\,\alpha\,\rangle$ and two CI-singles states

$$\begin{aligned} |\,\alpha\,\rangle &= a_a^\dagger a_b^\dagger a_c^\dagger \cdots |\,0\,\rangle \\ |\,\beta\,\rangle &= a_p^\dagger a_a \cdots |\,\alpha\,\rangle \\ |\,\gamma\,\rangle &= a_p^\dagger a_b \cdots |\,\alpha\,\rangle \end{aligned} \tag{5.3}$$

with single-electron energies ϵ_a, ϵ_b, and ϵ_c...and many-body energies ϵ_α, ϵ_β and ϵ_γ. In the case of neon atom, we have $a = 2p$, $b = 2s$ and $p = kd$. To obtain the photoelectron spectra, we must calculate the final probability amplitude $S_\xi = \lim_{t\to\infty} c_\xi(t)$ to singly-excited states $\xi = \alpha$ or β after the interaction. The total photoelectron spectrum $|S_\alpha|^2 + |S_\beta|^2$ is the incoherent sum of the ionic channel resolved spectra. The n-photon process can be treated with the nth-order perturbation amplitude.

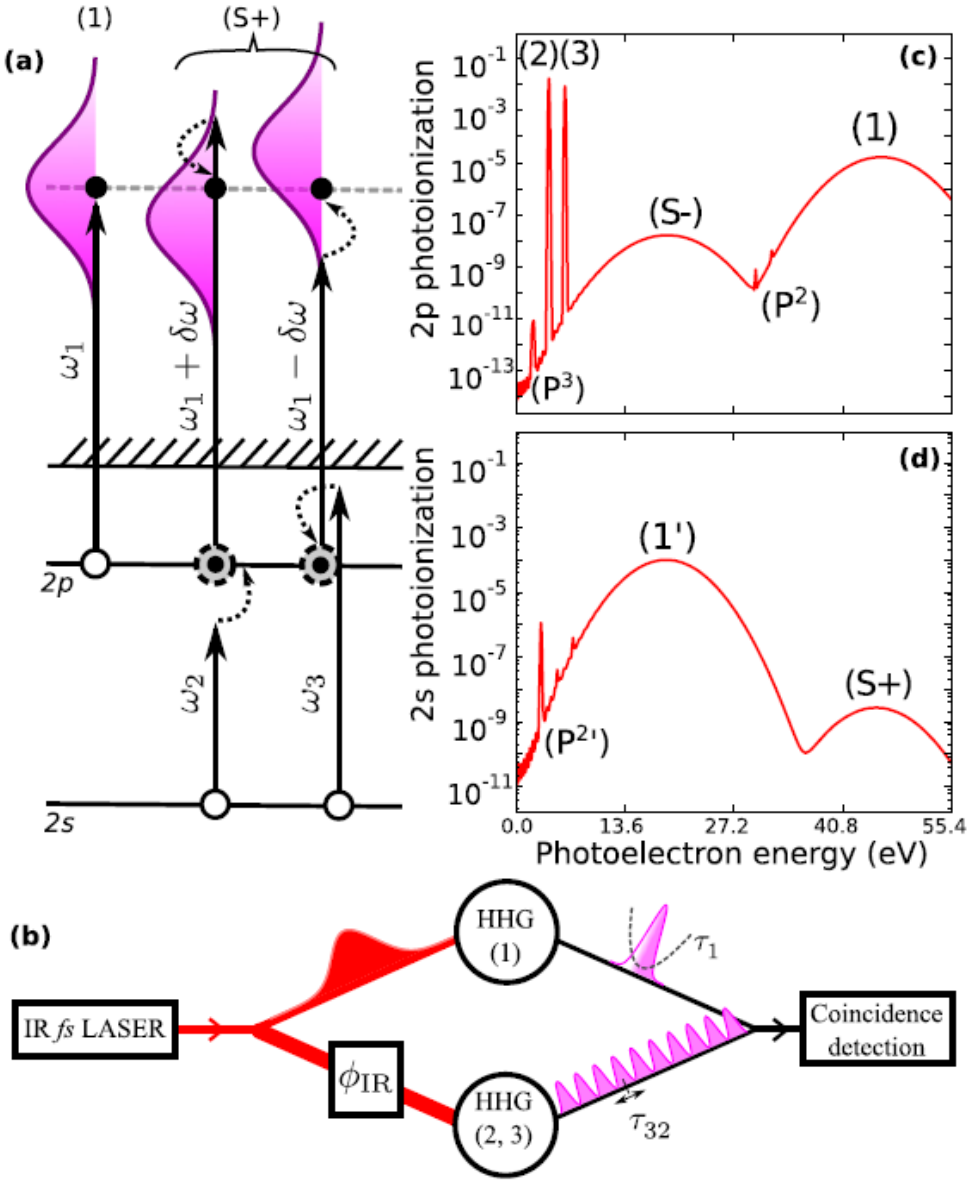

Figure 5.1: Overview of STRIDER scheme: (a) Photoionization process in neon: photoelectron replica of attosecond pulse by one-photon absorption from $2p$ state; (S+) nonsequential two-photon processes generating spectrally sheared replicas by stimulated ionic transitions with a final hole in the $2s$ state. (b) Sketch of the proposed experiment where an IR laser field is split into two parts for generation of XUV pump (1) and XUV probe (2,3) fields by HHG. Photoionization of neon atoms is then studied with electron-ion coincidence detection. (c) Photoelectron spectrum with residual hole in $2p$ state and (d) photoelectron spectrum with residual hole in $2s$ state, both computed by 1D TDCIS (within an independent-particle model). This figure is taken from [95]. See main text for the labeled spectroscopic structures.

5.1.1 Second-order perturbation Theory

The first order perturbation amplitude for excitation from α to β by the external field is given by

$$c_{\beta}^{(1)}(t) = \frac{1}{i}\int_{t_0}^{t} dt' \langle\, \beta \,|\, V(t') \,|\, \alpha \,\rangle \exp[i\omega_{\beta\alpha}t'] \tag{5.4}$$

with $\omega_{\beta\alpha} = \epsilon_\beta - \epsilon_\alpha$. In the following, $c_{\beta(1)}(t)$ is the amplitude to the state β by absorption of one pump photon from the field, $E_1(\omega)$ within first order perturbation theory. The perturbation amplitude for absorption of one pump photon, 1, and one probe photon, $f = 2$ or 3, is

$$c_{\beta}^{(2)}(t) = -\frac{1}{i}\sum_{\beta'}\int_{-\infty}^{t} dt' \langle\, \gamma \,|\, \sum_{f=2}^{3} V_f(t') \,|\, \beta' \,\rangle \exp[i\omega_{\gamma\beta'}t'] c_{\beta'(1)}^{(1)}(t'). \tag{5.5}$$

The many-body matrix element has two single-particle terms

$$Z_{\gamma\beta'} = -z_{ab}\delta_{pp'} + z_{pp'}\delta_{b,a}, \tag{5.6}$$

in which the probe photon interacts with the hole, a or the electron p'. In each case the other particle remains in the original state. In the following, we will neglect the second term for which the electron is first pumped from inner orbital, c, and then makes a continuum-continuum transition, p to p'. This is a good approximation because ATI processes are known to be weak for XUV fields. In the last part of this chapter, we will quantitatively discuss the ATI effect. In addition, we will focus on the dominant time ordering, the pump-probe sequence. The perturbation amplitude for $|\,\alpha\,\rangle \Rightarrow |\,\beta\,\rangle \Rightarrow |\,\gamma\,\rangle$ by absorption of one photon, 1, and one of the probe photons, $f = 2$ or 3, becomes

$$\begin{aligned} c_{\gamma}^{(2)}(t) \approx & -\sum_{f=2}^{3}(\frac{1}{i})^2 z_{pa}z_{ab}(\frac{-1}{2\pi})\tilde{E}_f^{(0)}\int_{\omega_{\min}}^{\omega_{\max}} d\omega_1' \tilde{E}_1(\omega_1') \\ & \times \int_{-\infty}^{t} dt' \exp[i(\omega_{\gamma\beta}-\omega_f)t'] \lim_{\xi\to 0^+}\int_{-\infty}^{t'} dt'' \exp[i(\omega_{\beta\alpha}-\omega_1-i\xi)t''] \end{aligned} \tag{5.7}$$

The second line of Eq. 5.7 is evaluated, using Sokhotski-Plemelj theorem and the definition of the delta function, for the limit of $t \to \infty$ as

$$2\pi i\delta(\omega_{\gamma\alpha}-\omega_f-\omega_1') \times \left[\text{p.v.}\frac{1}{\omega_1'-\omega_{\beta\alpha}} - i\pi\delta(\omega_1'-\omega_{\beta\alpha})\right], \tag{5.8}$$

where total energy conservation for the two-photon process is ensured by the left-most delta function, $\omega_{\gamma\alpha} = \epsilon_p - \epsilon_b = \omega_1' + \omega_f$. The second factor in Eq. 5.8 contains a real non-resonant contribution (principal value term) and an imaginary resonant contribution (delta function term) for the initial excitation step, α to β. The final perturbation amplitude becomes

$$S_\gamma^{(2)} = \lim_{t\to\infty} c_\gamma^{(2)}(t) = \frac{1}{2\pi i}\sum_{f=2}^{3} M_{pb,f}^{(hole)}\tilde{E}_1(\omega_{\gamma\alpha}-\omega_f)\tilde{E}_f^{(0)}, \tag{5.9}$$

where

$$M_{pb,f}^{(\mathrm{hole})} = \frac{z_{pa}z_{ab}}{\omega_f - \epsilon_c + \epsilon_b} \tag{5.10}$$

is the two-photon matrix element and "(hole)" in the subscript represents only the hole transition, the first term in Eq. 5.6, is considered. Assuming that $\omega_2 = \omega_{\gamma\beta} - \delta\omega$ and $\omega_2 = \omega_{\gamma\beta} + \delta\omega$, then the yield for the final state, $|\,\gamma\,\rangle$, is a standard interference pattern between two signals corresponding to the two quantum pathways,

$$\begin{aligned} W_\gamma &= |S_\gamma^{(2)}|^2 = |\sum_{f=2}^{3} S_{\gamma(f,1)}^{(2)}|^2 = |S_{\gamma(2,1)}^{(2)}|^2 + |S_{\gamma(3,1)}^{(2)}|^2 + 2\mathrm{Re}[S_{\gamma(3,1)}^{(2*)}S_{\gamma(2,1)}^{(2)}] \\ &= A_\gamma - B_\gamma\cos[\phi_1(\omega_{\gamma\alpha}-\omega_2) - \phi_1(\omega_{\gamma\alpha}-\omega_3) - \phi_{32}] \end{aligned} \tag{5.11}$$

where the subscript $(f,1)$ denotes absorption of one photon from the pump field 1 followed by absorption of probe photon f, and $\phi_{32} = \phi_3 - \phi_2$. Here

$$A_\gamma = \frac{|z_{pa}|^2|z_{ab}|^2}{4\pi^2\delta\omega^2}\left[|\tilde{E}_1(\omega_{\beta\alpha}+\delta\omega)|^2|\tilde{E}_2^{(0)}|^2 + |\tilde{E}_1(\omega_{\beta\alpha}-\delta\omega)|^2|\tilde{E}_3^{(0)}|^2\right] \tag{5.12}$$

comes from the direct sum of the pathways and

$$B_\gamma = \frac{|z_{pa}|^2|z_{ab}|^2}{2\pi^2\delta\omega^2}|E_1(\omega_{\beta\alpha}+\delta\omega)||\tilde{E}_1(\omega_{\beta\alpha}-\delta\omega)||\tilde{E}_2^{(0)}||\tilde{E}_3^{(0)}| \tag{5.13}$$

comes from the cross term. The term inside the cosine function can be expressed as the group delay of the pump pulse and the probe pulse such that Eq. 5.11 can be written as

$$W_\gamma = A_\gamma - B_\gamma\cos[2\delta\omega(\tau_1^{(\mathrm{GD})}(\omega_{\beta\alpha}) - \tau_{32}^{(\mathrm{GD})})], \tag{5.14}$$

where $\tau_{32}^{(\mathrm{GD})} = \phi_{32}/(2\delta\omega)$ and $\tau_1^{(\mathrm{GD})}$ is the group delay of the pump pulse. The desired group delay

$$\tau_1^{(\mathrm{GD})}(\omega_{\beta\alpha}) \approx \frac{\phi_1(\omega_{\beta\alpha}+\delta\omega)-\phi_1(\omega_{\beta\alpha}-\delta\omega)}{2\delta\omega} = \frac{\phi_1(\omega_{\gamma\alpha}-\omega_2)-\phi_1(\omega_{\gamma\alpha}-\omega_3)}{2\delta\omega} \tag{5.15}$$

can be reconstructed by measuring the signal modulation as a function of $\tau_{23}^{(\mathrm{GD})}$. The above finite difference approximation is valid if the detuning frequency is much smaller than the bandwidth of the pump pulse $\delta\omega \ll \Delta\omega_1$.

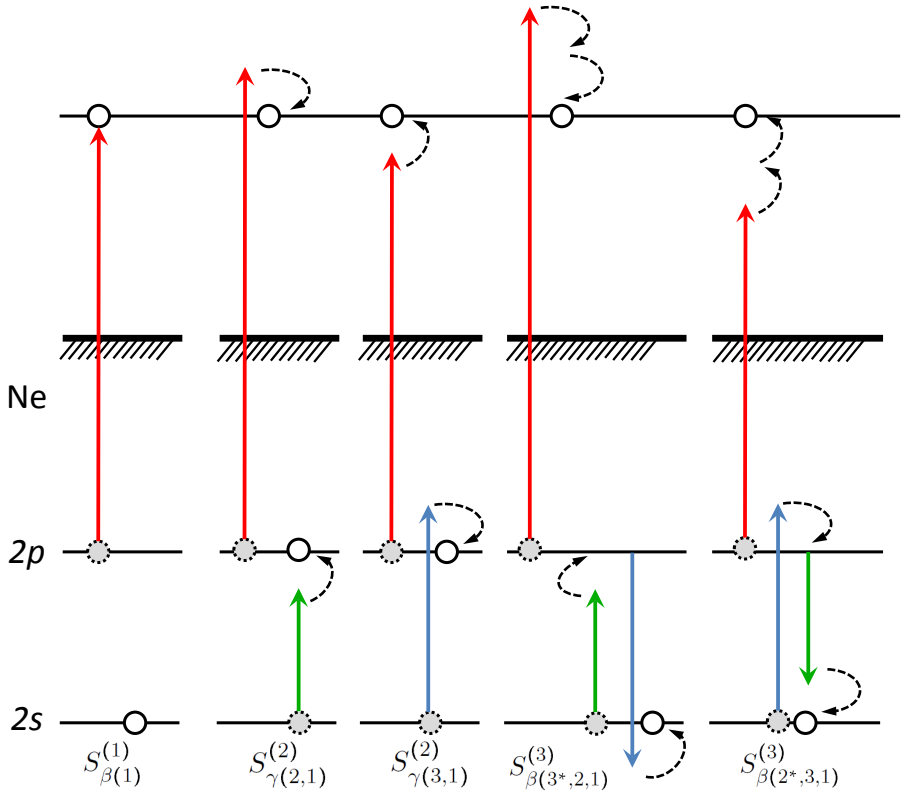

Figure 5.2: The schematic diagram of the pathway corresponding to the 1st, 2nd, and 3rd order perturbative amplitudes. The solid circles represent electrons and and the dashed circle represent electronic holes left in the shells after an electron absorb a photon.

5.1.2 Third-order perturbation

In addition to the signal modulation on the channel γ, the third order perturbation amplitude $|\,\alpha\,\rangle \Rightarrow |\,\beta\,\rangle \Rightarrow |\,\gamma\,\rangle \Rightarrow |\,\beta\,\rangle$ comprises processes which imply absorption of a pump photon, 1 and a probe photon, f, followed by (re-)emission of a probe photon, g. The perturbation amplitudes read

$$c^{(3)}_{\beta(g*,f,1)}(t) = \frac{1}{i}\int_{-\infty}^{t} dt' \langle\,\beta\,|\,V_g(t')\,|\,\alpha\,\rangle \exp[i\omega_{\beta\gamma}] c^{(2)}_{\gamma(f,1)}(t'), \tag{5.16}$$

where the conjugation in subscript $(g^*, f, 1)$ denotes emission of the probe photon, g. We again approximate the N-body matrix elements with the single-particle hole-hole transitions so that the final perturbation amplitude becomes

$$\begin{aligned} S^{(3)}_{\beta(g*,f,1)} =& \frac{i}{(2\pi)^3} z_{ba} z_{ab} z_{pa} \tilde{E}^{(0)*}_g \tilde{E}^{(0)}_f \int_{\omega_{min}}^{\omega_{max}} d\omega_1' \tilde{E}_1(\omega_1') \times 2\pi\delta(\omega_{\beta\alpha} - \omega_1' - \omega_f + \omega_g) \\ &\times \left\{ \text{p.v.} \frac{1}{\omega_1' + \omega_f - \omega_{\gamma\alpha}} - i\pi\delta(\omega_1' + \omega_f - \omega_{\gamma\alpha}) \right\} \left\{ \text{p.v.} \frac{1}{\omega_1' - \omega_{\beta\alpha}} - i\pi\delta(\omega_1' - \omega_{\beta\alpha}) \right\}, \end{aligned} \tag{5.17}$$

In the case $\omega_f = \omega_{\gamma\beta} \pm \delta\omega$ and $\omega_g = \omega_{\gamma\beta} \mp \delta\omega$, we obtain

$$S^{(3)}_{\beta(g*,f,1)} = \frac{i}{(2\pi)^3} \frac{z_{ba} z_{ab} z_{pa}}{2\delta\omega^2} \tilde{E}^{(0)*}_g \tilde{E}^{(0)}_f \tilde{E}_1(\omega_{\beta\alpha} \mp 2\delta\omega). \tag{5.18}$$

The quantum pathways of the 1st to 3rd order perturbative amplitudes corresponding to the same photoelectron energy are shown in Fig. 5.2. The red, green, and blue arrows represents the photon with frequency ω_1', ω_2, and ω_3 respectively. The third order effects, which result from in the two spectral shearing effect, originate from the absorption of a red (blue) detuned photon and the emission of a blue (red) detuned probe photon. Summation of both quantum paths ($S^{(3)}_{\beta(3*,2,1)}, S^{(3)}_{\beta(2*,3,1)}$) yields the final perturbation amplitude,

$$\begin{aligned} S^{(3)}_{\beta} =& \frac{i}{(2\pi)^3} \frac{z_{ba} z_{ab} z_{pa}}{2\delta\omega^2} |\tilde{E}^{(0)}_2| |\tilde{E}^{(0)}_3| \\ &\times \left\{ |\tilde{E}_1(\omega_{\beta\alpha} + 2\delta\omega)| e^{i\phi_1(\omega_{\beta\alpha}+2\delta\omega) - i\phi_{32}} + |\tilde{E}_1(\omega_{\beta\alpha} - 2\delta\omega)| e^{i\phi_1(\omega_{\beta\alpha}-2\delta\omega) + i\phi_{32}} \right\} \end{aligned} \tag{5.19}$$

The interference between this third order processes and the first order process is comparable with the second order effect.

$$2\mathrm{Re}\left\{S_\beta^{(1)*}S_\beta^{(3)}\right\} = \frac{1}{(2\pi)^2}|\tilde{E}_2^{(0)}||\tilde{E}_3^{(0)}||\tilde{E}_1(\omega_{\beta\alpha})|\frac{z_{pa}^2 z_{ba}^2}{\delta\omega^2}\mathrm{Re}\Bigg\{\exp[-i\phi_1(\omega_{\beta\alpha})] \times\left(|\tilde{E}_1(\omega_{\beta\alpha}+2\delta\omega)|\exp[i\phi_1(\omega_{\beta\alpha}+2\delta\omega)-i\phi_{32}]+|\tilde{E}_1(\omega_{\beta\alpha}-2\delta\omega)|\exp[i\phi_1(\omega_{\beta\alpha}-2\delta\omega)+i\phi_{32}]\right)\Bigg\} \tag{5.20}$$

By expansion of $\phi_1(\omega)$ and $E_1(\omega)$ around $\omega = \omega_{\beta\alpha}$ in a Taylor series and using the relationship

$$\lim_{(B/A)\to 0} A\cos\theta + B\sin\theta = A\cos\left(\theta - \frac{B}{A}\right), \tag{5.21}$$

the yield for the final state, $|\beta\rangle$, can be written as

$$W_\beta = A_\beta - B_\beta\cos[2\delta\omega(\tau_1^{(\mathrm{GD})}(\omega_{\beta\alpha}) - \tau_{32}^{(\mathrm{GD})}) + \mathcal{O}(\delta\omega^3)], \tag{5.22}$$

where

$$B_\beta = -\frac{|z_{pa}|^2|z_{ab}|^2}{2\pi^2\delta\omega^2}|\tilde{E}_1(\omega_{\beta\alpha})|^2|\tilde{E}_2^{(0)}||\tilde{E}_3^{(0)}|. \tag{5.23}$$

If the total photoelectron spectrum, unresolved for the residual ionic state, is considered, the signal modulation from the $|\beta\rangle$ and $|\gamma\rangle$ is comparable. Moreover, B_γ and B_β cancel each other in the leading order of $\delta\omega$ and there is only some small higher order signals. Therefore, the total photoelectron spectrum $W_\gamma + W_\beta$ is not able to show clear ϕ_{23} dependence. To resolve the signal from the particular ionic state, the detection of the electron spectrum together with the ion-resolved spectrum, which is called coincidence detection, is needed.

5.2 Attosecond pulse characterization

Our theoretical calculations are performed within 1D TDCIS for the wavepacket propagation [83] and the t-SURFF method for calculating the photoelectron spectra [90] as introduced in 3.3. Here, we take the long lived 2s–2p transition of neon atom (26.9 eV) as an example for both SAP and APT cases. The peak intensity of the pump pulse is set to be $I_1 = 7\times10^{12}$ W/cm^2 with central frequency 68 eV (0.276 a.u.) and

the bandwidth $\Delta\omega_1 = 7.5$ eV (2.5 a.u. and Fourier-limited pulse duration of 244 as). The pair of probe fields are symmetrically red- and blue-shifted relative to the 2s–2p transition of neon with detuning $\delta\omega = 1$ eV and the bandwidth $\Delta\omega_{2,3} = 0.125$ eV, which is chosen to satisfied $\Delta_{2,3} \ll \delta\omega$ so that the delta function distribution of the probe field frequency is a good approximation.

5.2.1 Single attosecond pulse

We consider the pump pulse for characterization is a Gaussian function

$$\tilde{E}_1(\omega) = \tilde{E}_1^{(0)} \exp[-2(\ln 2)(\omega - \omega_1)^2/\Delta\omega_1^2 + i\phi_1(\omega)]. \tag{5.24}$$

With the numerical calculation in the case $\phi_1(\omega) = 0$, Fig. 5.1 (b) and (c) show the photoelectron spectra with outer (2p) and inner (2s) hole in the residual ion. The two narrow peaks (2,3) in Fig. 5.1 (b) are due to the absorption of the pair of probe fields with photon energy $\omega_{2/3} = 26.9 \pm 1$ eV by the outer-valence electron and the broad peaks (1,1') are due to the absorption of the XUV attosecond pulse with central energy $\omega_1 = 68$ eV. Other peaks $(2, 3, \mathrm{S}+, \mathrm{S}-, \mathrm{P}^2, \mathrm{P}^{2\prime}, \mathrm{P}^3)$ are due to high-order interactions. In the following analysis, we only focus on the peak (S+), that originates from the pathway of photoionization from the 2p orbital by the XUV attosecond pulse, followed by absorption of a probe photon which induces a transfer of the hole to the 2s orbital.

The photoelectron spectra with an inner shell (2s) hole in the residual ion as a function of the kinetic energy and the relative phase $\phi_{23} = \phi_2 - \phi_3$ of the probe pulses is shown in Fig. 5.3 for (a) a Fourier limited pulse, $\phi_1(\omega) = 0$; (b, c) a quadratic phase dependence $\phi_1(\omega) = \alpha(\omega - \omega_1)^2$ with $\alpha = 10$ and 100; and (d) a cubic phase dependence $\phi_1(\omega) = \beta(\omega - \omega_1)^3$ with $\beta = 100$. In Fig. 5.3 (a), the (S+) peak vanishes for $\phi_{32} \approx 0$, while the peak is maximized for $\phi_{32} \approx \pi$. As derived in Eq. 5.9-5.14, the position of the extreme values of the peak is due to the relative π shift between the two-photon pathways that have positive and negative detuning with respect to the hole response, respectively. To reveal the probe-phase dependent modulation, the spectra are normalized along the vertical axis by their maximal value (Fig. 5.3 (e)-(h)). The evolution of the maximum for a given kinetic energy is represented by a dashed line and follows the equation $\phi_{23} = 2\delta\omega\tau_1^{\mathrm{GD}}(\omega) + \pi$. The group delay τ_1^{GD} can therefore be directly extracted by fitting the dashed line by the equation. We get the retrieved parameters $\alpha = 0.01$, 9.95, 99.4 and $\beta = 99.1$, in excellent agreement with the actual

values.

Furthermore, our simulation show that the (S-) peak has a similar ϕ_{32} dependence as (S+) in Fig.. The one-photon peaks (1) and (1') also modulate with ϕ_{32}, but the variation is opposite to that of (S+) and (S-). The modulation can be explained by the third-order perturbation theory in Section 5.1.2 and, physically, this is because the probe fields are effectively shifting the ionic channel of the photoelectron, e.g., by redistribution of the population from peak (1) to peak (S+) via the pathway $|\,\alpha\,\rangle \Rightarrow |\,\beta\,\rangle \Rightarrow |\,\gamma\,\rangle \Rightarrow |\,\beta\,\rangle$. The total photoelectron spectrum, unresolved for the residual ionic state, does not show clear ϕ_{32} dependence. Unfortunately, this makes the experimental measurement of the (S+) challenging, because it must rely on coincidence detection.

5.2.2 Attosecond pulse train

For the single attosecond pulse characterization, this idea is more challenging to implement experimentally than the conventional attosecond streak camera because the coincidence measurement is needed. However, if we want to characterize the attosecond pulse train, this experimental challenge decreases. In this case the (S+) signal then resides on peaks in between the comb-like peaks of the pump field, which means that the ϕ_{32} dependence can also be studied without coincidence detection, but only at discrete energy intervals determined by the comb structure.

Because the APT is generated via HHG process, the frequency domain of the APT consists of the frequency comb of odd harmonics $\omega_q = (2q+1)\omega_{\mathrm{IR}}$. The pump APT can be written as

$$\tilde{E}_1(\omega) = \tilde{E}_{\mathrm{env}}(\omega) \sum_q \tilde{E}_q[\omega - (2q+1)\omega_{\mathrm{IR}}], \tag{5.25}$$

where the envelope of the pump amplitude $\tilde{E}_{\mathrm{env}}(\omega) = |\tilde{E}_{\mathrm{env}}(\omega)| \exp(i\phi_1(\omega))$ with central frequency ω_1, the spectral bandwidth $\Delta\omega_1$ and the spectral phase

$$\phi_1(\omega) = \alpha(\omega - \omega_1)^2 + \beta(\omega - \omega_1)^3 + \ldots \tag{5.26}$$

In addition, $\tilde{E}_q(\omega - (2q+1)\omega_{\mathrm{IR}}) \in \mathbb{R}$ is the line shape of each harmonics. The group delay defined as $\tau_1^{(\mathrm{GD})}(\omega) = d\phi_1/d\omega$ can be interpreted as the time when the frequency ω dominates in the oscillation. If the pulse is generated by HHG, $\tau_1^{(\mathrm{GD})}(\omega)$ also represents the relative emission time of the frequency components in the HHG process.

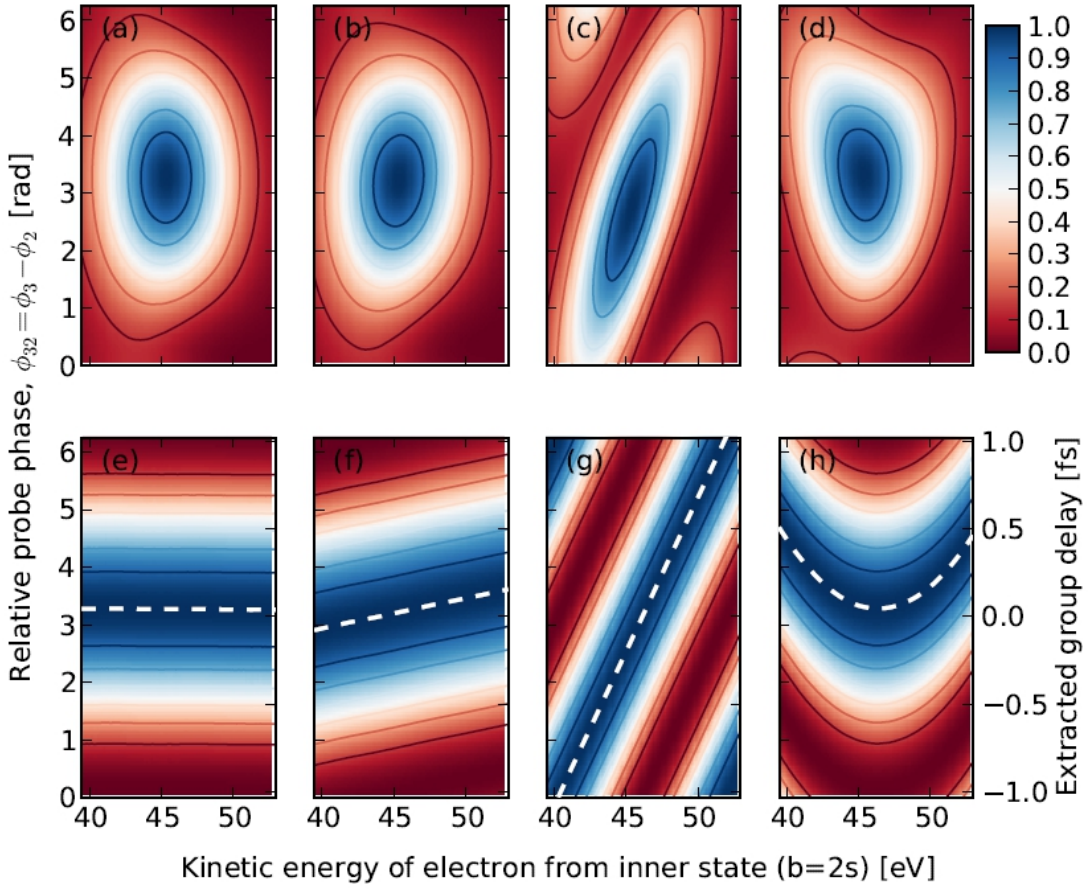

Figure 5.3: Delay-dependent modulations of the (S+) peak: (a)-(d) normalized photoelectron peak [see (S+) in Fig. 5.1 (d)] as a function of the phase difference between probe fields for (a) unchirped pulse; (b, c) increasing linear chirp; and (d) quadratic chirp. (e)-(h) same as (a)-(d) but with normalization along the vertical axis to reveal the modulation over delay at each kinetic energy. The dashed white curve shows the sub-femtosecond group delay of the pump pulse with extracted (actual) phase parameters $\alpha = 0.01(0)$, $9.95(10)$, $99.4(100)$ and $\beta = 99.1(100)$. This figure is taken and modified from [95].

In STRIDER, we spectrally shear the photoelectron spectrum using two coherent XUV fields that stimulate interfering hole dynamics. The basic principle of our scheme is shown in Fig. 5.4 (b) compared with RABBIT as shown in Fig. 5.4 (a). We ionize neon from the 2p shell using an ATP. The wavepackets can be viewed as the replica of the ATP, which consists in the odd harmonics so that the separation between two peaks is equal to the fundamental frequency ω_{IR}. The detuning of the probe field set to be ω_{IR} induces the formation of the sideband peaks due to the spectral shearing including both positive and negative shifts away from the main peaks. Two interference pathways involving consecutive harmonics ($2q-1$ and $2q+1$) lead to the same sideband corresponding to the even harmonics $2q$. The transition amplitude from the ground state to the final state with photoelectron energy ϵ_p within the sideband $2q$ is denoted as $S_{2q}(\epsilon_p)$, which is the combination of the two pathway $S_{2q(2/3)}(\epsilon_p)$ induced by the XUV probe field $\tilde{E}_{(2/3)}(\omega) = E_{(2/3)}\delta(\omega-\omega_{(2/3)})$. Here we assume that the probe fields are monochromatic but in practice it is sufficient that the bandwidth is much smaller than the basis frequency, $\Delta\omega_{2,3} << \omega_{\mathrm{IR}}$. From the second order perturbation theory, the two-photon transition amplitude corresponding the pathway indicated in Fig. 5.4 (b) can be expressed as

$$S_{2q(2,3)}(\epsilon_p) = \frac{-z_{pb}z_{ab}}{2\pi i(\Delta\epsilon-\omega_{(2/3)})}|\tilde{E}_{\mathrm{env}}(\epsilon_p-\omega_{(2,3)})|\tilde{E}^{(0)}_{(2,3)}e^{i\phi_1(\epsilon_p-\omega_{(2,3)})}\sum_{q'}\delta(\epsilon_p-(2q'+1)\omega_{\mathrm{IR}}). \tag{5.27}$$

Then the photoelectron spectrum of the sideband depends on the phase difference between the two quantum pathways

$$\begin{aligned}|S_{2q}(\epsilon_p)|^2 &= |S_{2q(2)}(\epsilon_p)+S_{2q(3)}(\epsilon_p)|^2 \\ &= |S_{2q(2)}(\epsilon_p)|^2+|S_{2q(3)}(\epsilon_p)|^2+2|S_{2q(2)}(\epsilon_p)||S_{2q(3)}(\epsilon_p)|\cos[\arg(S^*_{2q(2)}(\epsilon_p)S_{2q(3)}(\epsilon_p))].\end{aligned} \tag{5.28}$$

Unlike the RABBIT scheme, this phase difference only depends on the phase of the laser field and does not depend on the atomic structure

$$\begin{aligned}\arg(S^*_{2q(2)}(\epsilon_p)S_{2q(3)}(\epsilon_p)) &= \phi_1(\omega_{2q+1})-\phi_1(\omega_{2q-1})+\phi_2-\phi_3 \\ &\approx 2\omega_{\mathrm{IR}}(\tau_1^{\mathrm{GD}}(\omega_{2q})-\tau_{32}),\end{aligned} \tag{5.29}$$

where $\tau_{32} \equiv (\phi_3-\phi_2)/(2\omega_{\mathrm{IR}})$ and τ_{2q} calculated here is the finite difference approximation

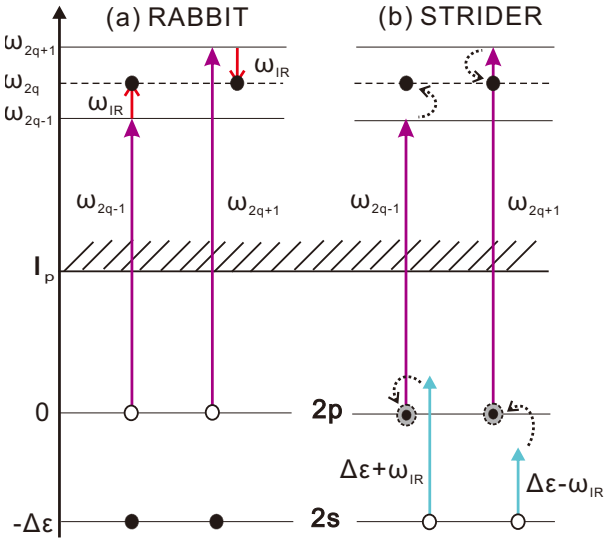

Figure 5.4: Photon diagrams associated with the two characterization methods. (a) RABBIT: Sidebands are created through the absorption and emission of an additional IR probe photon by the photoelectron replica of APT from outer valence, 2p. (b) STRIDER: Sidebands are created through the spectrally sheared replicas by stimulated ionic transitions leading to a hole in the inner valence, 2s.

to the group delay. The measured intensity of the sideband as the function of phase delay ϕ_{32} is

$$I_{2q}(\phi_{32}) = \int_{\omega_{2q}-\delta}^{\omega_{2q}+\delta} |S_{2q}(\epsilon_p)|^2 d\epsilon_p = A_{2q} - B_{2q}\cos[2\omega_{\mathrm{IR}}\tau_{2q} - \phi_{32}], \tag{5.30}$$

where the integration is performed within small range of energy closed to the sideband peak. In Eq. 5.30, A_{2q} is the incoherent sum of the transition strength, while B_{2q} relates to the cross term of the amplitudes, both are independent of the delay of the fields. The desired group delay τ_1^{GD} can be directly reconstructed by measuring the I_{2q} as the function of ϕ_{32}.

The numerical calculation is performed with the same pulse intensity, central frequency and the bandwidth as the case of SAP. The fundamental frequency of the pulse train is chosen to be 1 eV and the bandwidth of each harmonics is 0.125 eV. The results of the inner hole structures are presented in Fig. 5.5 as a function of relative probe phase ϕ_{23}, for (a) a Fourier limited pump pulse, $\phi_1(\omega) = 0$; (b,c) a quadratic phase dependence, $\phi_1(\omega) = \alpha(\omega - \omega_1)^2$ with $\alpha = 10$ and 100, respectively; and (d) a cubic phase dependence, $\phi_1(\omega) = \beta(\omega - \omega_1)^3$. Fig. 5.6 compares the photoelectron spectrum between the spectrum with and the spectrum with outer-hole. The inner-hole photoelectron spectra of Fig. 5.5 (b) for $\phi_{32} = 0$ (red solid line), $\phi_{32} = \pi$ (green dash line) are plotted together with the outer-hole photoelectron spectrum for $\phi_{32} = 0$ (blue

dash-dot line). Unlike the SAP case shown in Fig. 5.1, both the main signal of the spectra with inner hole and their signal difference between them are several orders larger than the spectra with outer hole at the position of side bands. In other words, the inner-hole spectrum dominates the total spectrum not only in the yield but also in the signal variation at the discrete energy intervals. Therefore, the attosecond pulse train characterization can be studied without coincidence detection.

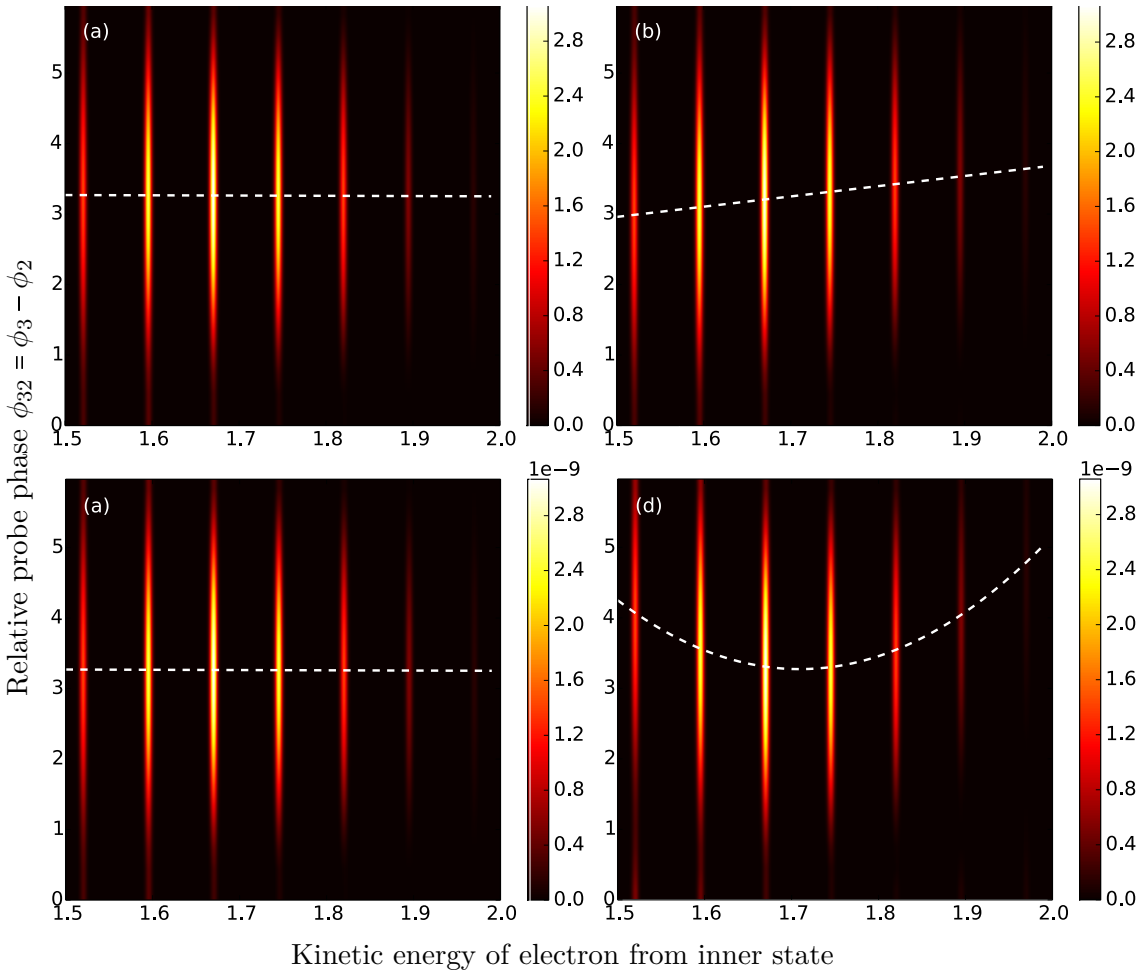

Figure 5.5: Photoelectron spectra as a function of the phase different between probe fields, for (a) a Fourier limited pump pulse ($\alpha = 0$); (b,c) linear chirp ($\alpha = 10, 100$); and (d) quadratic chirp ($\alpha = 0, \beta = 100$) of pump pulse. The dashed curve shows the extracted group delay of the pump pulse.

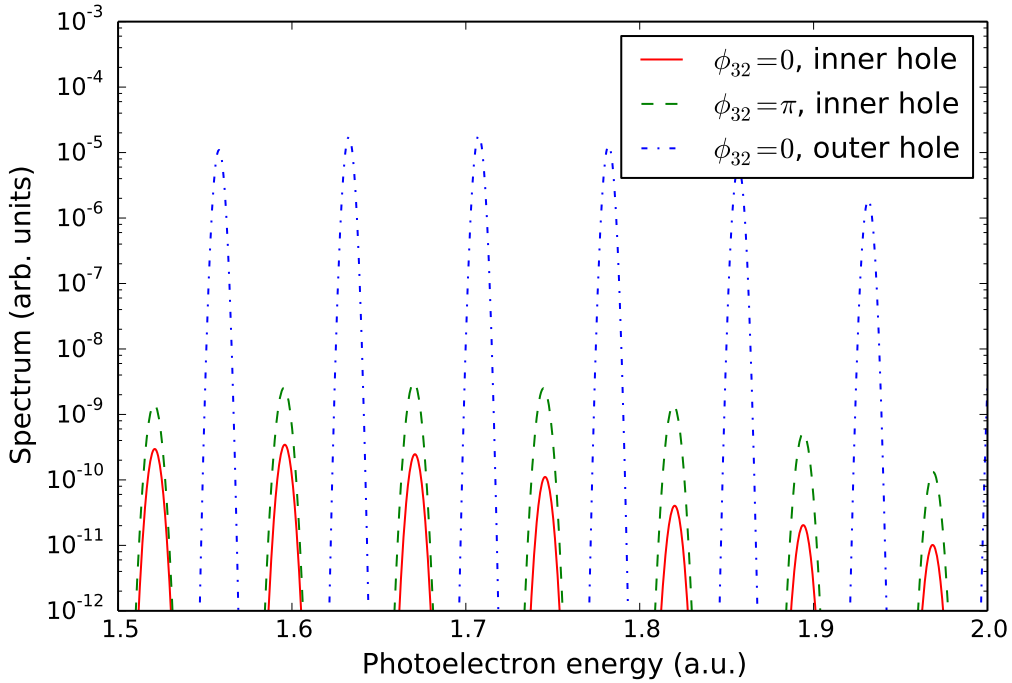

Figure 5.6: The inner-hole photoelectron spectra of Fig. 5.5 (b) for $\phi_{32} = 0$ (red solid line), $\phi_{32} = \pi$ (green dash line), and the outer-hole photoelectron spectrum for $\phi_{32} = 0$ (blue dash-dot line)

5.3 Atomic response time

In the expression of $S_\gamma^{(2)}$ in Eq. 5.9, only the hole transition in the total dipole transition $Z_{\gamma\beta'}$ is considered as shown in Fig. 5.8 (a). If the electron continuum-continuum transition is also taken into account as shown in Fig. 5.8 (b), where the inner shell electron is directly ionized by the pump pulse and then absorbs a probe photon inducing an above-threshold ionization (ATI) pathway, the total two-photon matrix element can be written as

$$M_{pb,f} = M_{pb,f}^{(\text{hole})} + M_{pb,f}^{(\text{elec.})}. \tag{5.31}$$

Here the stimulated electron term is

$$M_{pb,f}^{(\text{elec.})} = \lim_{\xi\to 0} \sum\!\!\!\!\!\!\int_{p'} \frac{z_{pp'} z_{p'b}}{\omega_1' - \epsilon_{p'} + \epsilon_b + i\xi} = \text{p.v.} \sum\!\!\!\!\!\!\int_{p'} \frac{z_{pp'} z_{p'b}}{\omega_1' - \epsilon_{p'} + \epsilon_b} - i[h(\epsilon_r) + (\Delta\epsilon - \omega_f)h'(\epsilon_r)], \tag{5.32}$$

where $h(\epsilon_r) = \pi z_{pr} z_{rb}$ with $\epsilon_r = \epsilon_p - \Delta\epsilon$. In Eq. 5.32 we write the matrix element as real nonresonant contributions and an imaginary resonant contribution via the intermediate with energy $\epsilon_p - \omega_f$. If the probe fields are in the IR range such as streaking camera or RABBIT, the stimulated electron transition is a good approximation $M_{pb,f} \approx M_{pb,f}^{(\mathrm{elec.})}$ because the frequency of IR fields are far away from resonance. However, in this case with nearly resonant XUV transitions, we show that stimulated electron contributions $M_{pb,f}^{(\mathrm{elec.})}$ are 2-3 orders of magnitude smaller than the total contributions $M_{pb,f}$ that are dominated by the strong resonant coupling in the residual ion as shown Fig. 5.7 (a). Therefore, the total matrix element is better approximated as a hole transition, which is real, plus a small imaginary electron transition

$$M_{pb,f} \approx M_{pb,f}^{(\mathrm{hole})} + i\mathrm{Im}M_{pb,f}^{(\mathrm{elec.})}. \tag{5.33}$$

As a result, there is an additional time delay

$$\tau_{pb}(\omega_{\beta\alpha}) \equiv \frac{\mathrm{Arg}(M_{pb,2}M_{pb,3}^{*} - \pi)}{2\delta\omega}, \tag{5.34}$$

the so-called response time introduced in Chapter 2, so that the equation can be rewritten as

$$W_\gamma = A_\gamma - B_\gamma \cos[2\delta\omega(\tau_1^{(\mathrm{GD})}(\omega_{\beta\alpha}) - \tau_{32} - \tau_{pb}(\omega_{\beta\alpha}))]. \tag{5.35}$$

If the electron transition is not considered, $M_{pb,2}M_{pb,3}^{*} = M_{pb,2}^{(\mathrm{hole})}M_{pb,3}^{(\mathrm{hole})*}$ is a pure negative number so that $\tau_{pb} = 0$. When the electron transition is included,

$$M_{pb,2}M_{pb,3}^{*} = -\left(\frac{z_{ab}z_{pa}}{\delta\omega}\right)^2\left[1 + 2i\left(\frac{\delta\omega}{z_{ab}z_{pa}}\right)h(\epsilon_r)\right] \tag{5.36}$$

contains an imaginary part so that

$$\tau_{pb} \approx \frac{1}{2\delta\omega}\arctan\left[2\left(\frac{\delta\omega}{z_{ab}z_{pa}}\right)h(\epsilon_r)\right] \approx \frac{1}{\delta\omega}\arctan\left[\frac{\pi z_{pr}z_{rb}}{z_{ab}z_{pa}}\right] \approx \frac{\pi z_{pr}z_{rb}}{z_{ab}z_{pa}}. \tag{5.37}$$

Eq. 5.37 shows that τ_{pb} does not depend strongly on $\delta\omega$ but rather gives direct information about the ratio between dipole matrix elements of the stimulated electron and hole transitions.

In Fig. 5.7 (b), we present τ_{pb} from Eq. 5.34 using the 3D independent-particle model with the matrix elements given Eq. 5.33. A positive linear drift is found on both final partial waves, ks and kd, which we attribute to an increasing relative contribution from the resonant electron path, ie, the numerator on the right hand side of Eq. 5.37. We also show τ_{pb} for photoelectrons with momentum $\mathbf{k} = \mathbf{k}\hat{\mathbf{z}}$ along the polarization axis, computed by the complex final state defined by Eq. 2.26. The angle-resolved emissions has a linear drift of 0.634 as/eV, quite close to the dominant d-wave. Over a large energy range, from 65 to 120 eV, the deviation from this linear fit is less than 1 as.

In the time-dependent calculation, we show the response time for the case of an unchirped pump pulse, i.e., by zooming in on the dashed curve in Fig. 5.3(d), for three different symmetric detuning of the probe fields, $\delta\omega = 1, 1.5,$ and 2eV in Fig. 5.9. All values of detunings show qualitatively the same result with a response time in the range 40–55 as. All curves exhibit a negative slope with extracted α values for detuning 1, 1.5, and 2 eV equal to -0.288, -0.239, and -0.160, respectively. To understand the electron transition due to the probe fields, this coupling can be removed by assuming that the probe fields only couples with different ionic channel, and the TDCIS equation becomes

$$i\dot{\alpha_0} = -E_{\text{pump}}(t)\sum_i \langle\varphi_i|\hat{z}|\chi_i, t\rangle \tag{5.38}$$

and

$$\begin{aligned} i\frac{\partial}{\partial t}|\chi_i\rangle = (\hat{H}_0 - \varepsilon_i)|\chi_i\rangle + \sum_{i'}\hat{P}\{\hat{K}_{i'i} - \hat{J}_{i'i}\}|\chi_i'\rangle - E_{\text{pump}}(t)\hat{P}\hat{z}\{\alpha_0|\varphi_i\rangle + |\chi_i\rangle\} \\ + (E_{\text{pump}}(t) + E_{\text{probe}}(t))\sum_{i'} z_{i'i}|\chi_{i'}\rangle, \end{aligned} \tag{5.39}$$

where $E_{\text{pump}} = E_1$ and $E_{\text{probe}} = E_2 + E_3$. In the tsurff formalism, the vector potential of the pump field should be used rather than the total laser field in the Volkov state. In Fig. 5.9, we label this result as "no ATI" (no above-threshold ionization) because the electron cannot absorb probe photons after it has been ejected. The extracted α parameter is –0.00294, which is much closer to the expected zero value. This shows that XUV-driven electron continuum dynamics must be responsible for the finite response time.

For $\alpha \neq 0$, the results with different laser parameters are listed in Table 5.1. We note that the difference between the case with ATI and without ATI (rightmost column)

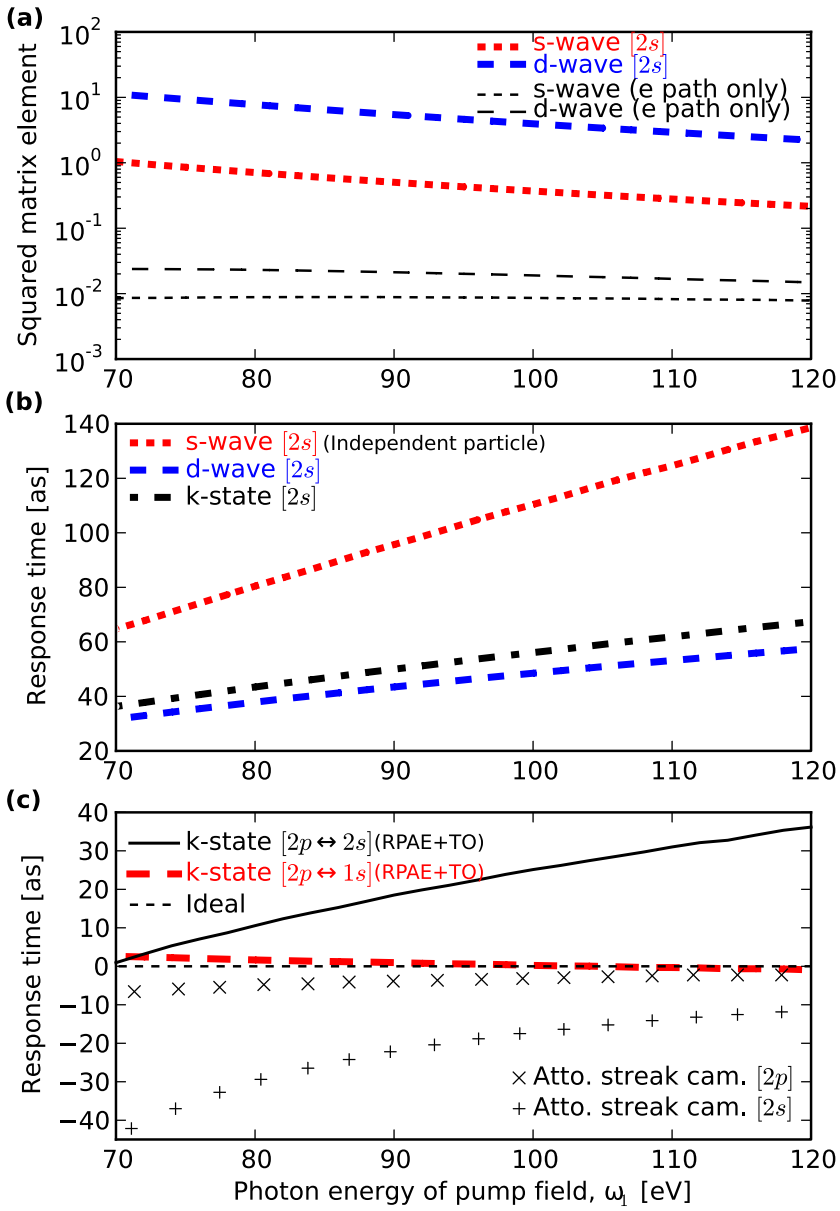

Figure 5.7: (a) Squared matrix elements, $|M_{pb,f}|^2$, for the s-wave (dotted) and d-wave (dashed), including both stimulated hole and electron pathways in the bold lines and only electron pathways in the thin lines. (b) Response time for photoemission along the polarization axis, s-wave and d-wave. Data presented in (a) and (b) are computed by a 3D independent-particle model for neon. (c) Response time for photoemission along the polarization axis (within a correlated model including both time orderings) for the stimulated valence hole ($2p \to 2s$) and core hole ($2p \to 1s$) transitions. The streak-camera delay from the initial $2p$ ($2s$) state is shown [58] for reference. This figure is taken from [95].

with $\delta\omega$ = 1 eV is approximately -0.3, in agreement with the result for the α = 0 case. This indicates that the electron transition due to probe fields does not strongly depend on the chirp of the pump pulse. However, we found that the deviation becomes larger when the chirp is larger as shown in Table 5.1. However, unlike the α = 0 case, the extracted parameters are always smaller than the expected original values and the deviation is larger than 0.1. This deviation is found to be related to the bandwidth of the probe fields, or the finite duration, and will be discussed in the next section.

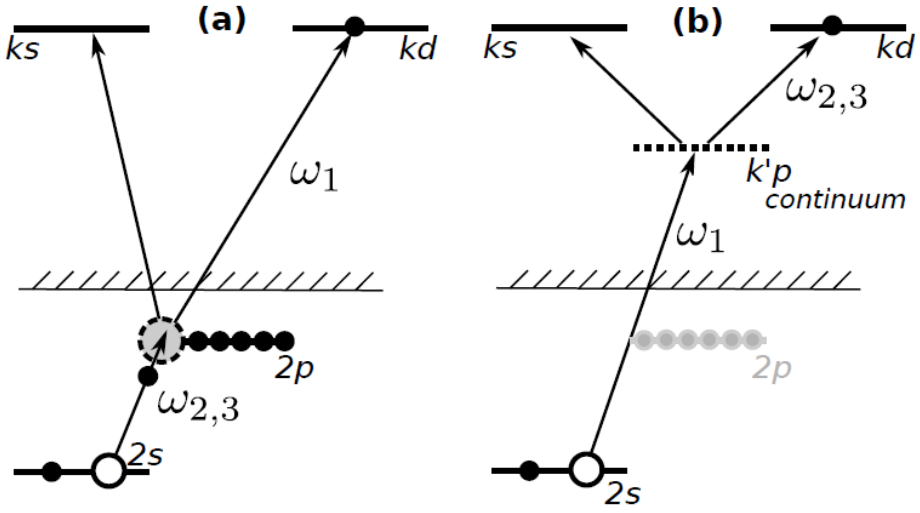

Figure 5.8: (a) Two-photon diagram for stimulated hole transition, 2p → 2s, after photoemission from outer state, 2p → ks,kd. (b) Two-photon diagram for stimulated electron continuum transition from an inner valence state, 2s → kp → ks,kd. This figure is taken from [95].

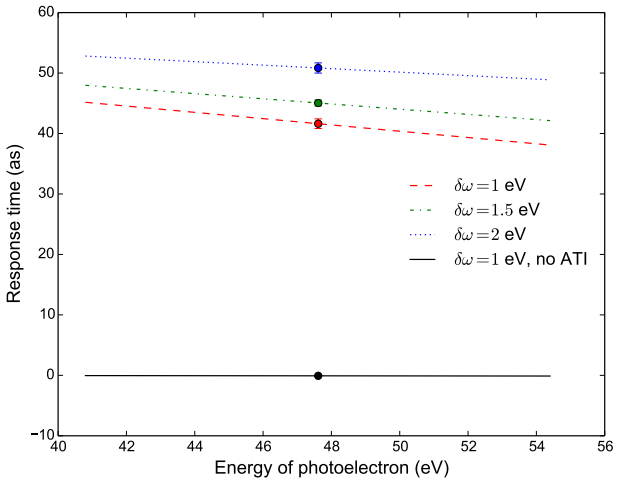

Figure 5.9: Detailed study of the "response time" of the (S+) peak for three different values of detuning of the probe field gives an unchirped pump pulse (α = β = 0). In accordance with Eq. 5.35, the response time, τ_{pb}, is extracted by making a cosine fit to the phase-dependent oscillations of the photoelectron probability, e.g., the modulations shown in Fig. 2(e) (where $\delta\omega$ = 1 eV). The raw data (not shown) has been fitted to a line in order to extract the α parameter of the pump pulse. Standard deviation of the linear fit is indicated by the error bars. This figure is taken from [95].

α	$\delta\omega$ (eV)	$\Delta\omega_1$ (eV)	$\Delta\omega_f$ (eV)	$\tilde{\alpha}$	Numerical		
					with ATI	Without ATI	difference
-100	1	7.5	0.0625	-99.79	-100.127	-99.85	-0.277
100	1	7.5	0.0625	99.79	99.55	99.86	-0.31
100	1	7.5	0.125	99.5	99.058	99.39	-0.332
100	0.5	7.5	0.125	97.69	97.149	97.57	-0.297
10	1	7.5	0.125	9.953	9.646	9.943	-0.421

Table 5.1: Comparison of the Retrieved α between analytical and numerical calculation

5.4 Convolution effect

In the derivation in Section 5.1.1, we argued that the bandwidth of probe fields are narrow so that the frequency distribution of the fields is assumed to be a delta function.

If the non-zero bandwidth of the probe field is considered, the convolution effect will smear out the signal. In order to discuss the pulse convolution effects that occur due to the finite bandwidth of the probe field, we assume these two fields are described with Gaussian function with additional phase

$$\tilde{E}_f(\omega) = |E_f| \exp[-(\omega - \omega_f)^2/\sigma_f^2 + i\phi_f] \tag{5.40}$$

The perturbation amplitude by absorption of one pump photon, 1, and one of the probe photons becomes

$$\begin{aligned} c_\gamma^{(2)}(t) = \sum_{f=2}^{3} \left(\frac{1}{2\pi i}\right)^2 z_{pa} z_{ab} \int d\omega_1' \tilde{E}_1(\omega_1') \int d\omega_f' \tilde{E}_f(\omega_f') \\ \times \int_{-\infty}^{t} dt' e^{i(\omega_{\gamma\beta} - \omega_f')t'} \int_{-\infty}^{t'} dt'' \lim_{\epsilon_1 \to 0^+} e^{i(\omega_{\beta\alpha} - \omega_1' - i\epsilon_1)t''} \end{aligned} \tag{5.41}$$

For the limit of $t \to \infty$, the final perturbation amplitude shown in Eq. 5.9 becomes

$$\begin{aligned} S_\gamma^{(2)}(t) = \sum_{f=2}^{3} \frac{-z_{pa} z_{ab}}{2\pi i} \int d\omega_f' \tilde{E}_1(\omega_{\gamma\alpha} - \omega_f') \tilde{E}_f(\omega_f') \left[\text{p.v.} \frac{1}{\omega_{\gamma\beta} - \omega_f'}\right] \\ + \sum_{f=2}^{3} 2\pi^2 \tilde{E}_1(\omega_{\beta\alpha}) \tilde{E}_f(\omega_{\gamma\beta}) \end{aligned} \tag{5.42}$$

Instead of the delta function shown in Eq. 5.8 due to the Fourier transform of the monochromatic waves, the first term in the right hand side of Eq. 5.42 is a convolution integral. We consider the pump pulse with quadratic phase (linear chirp):

$$\tilde{E}_1(\omega) = \tilde{E}_1^{(0)} \exp[-(\omega - \omega_1)^2/\sigma_1^2 + i\alpha(\omega - \omega_1)^2], \tag{5.43}$$

where $\sigma_1 = \Delta\omega_1/\sqrt{2\ln 2}$. The second term in the right hand side of Eq. 5.42 becomes

$$\exp[-(\omega_{\beta\alpha} - \omega_1)^2/\sigma_1^2 - (\delta\omega)^2/\sigma_f^2 + i\alpha(\omega_{\beta\alpha} - \omega_1)^2] \tag{5.44}$$

and decays to 0 quickly in the limit $\delta\omega >> \sigma_f$. Therefore, we only need to consider the first term, which becomes

$$\sum_{f=2}^{3} \frac{-z_{pa}z_{ab}}{2\pi i} \int d\omega'_f |\tilde{E}_1^{(0)}||\tilde{E}_f^{(0)}| e^{-g(\omega'_f)+i\phi_f} \left[\text{p.v.} \frac{1}{\omega_{\gamma\beta} - \omega'_f} \right], \tag{5.45}$$

where

$$g(\omega'_f) = \frac{(\omega_{\gamma\alpha} - \omega_1 - \omega'_f)^2}{\sigma_1^2} + \frac{(\omega'_f - \omega_f)^2}{\sigma_f^2} - i\alpha(\omega_{\gamma\alpha} - \omega_1 - \omega'_f)^2. \tag{5.46}$$

To deal with the convolution effect, we should take all terms of the function g into consideration when calculating the stationary point. The complex stationary point is

$$\omega'_{fs} = \frac{-\frac{(\omega_1 - \omega_{\gamma\alpha})}{\sigma_1^2} + \frac{\omega_f}{\sigma_f^2} + i\alpha(\omega_1 - \omega_{\gamma\alpha})}{\frac{1}{\sigma_1^2} + \frac{1}{\sigma_f^2} - i\alpha} \approx \omega_f - \frac{\sigma_f^2}{\sigma_1^2}(\delta\omega_{\gamma f}) + i\sigma_f^2\alpha(\delta\omega_{\gamma f}), \tag{5.47}$$

where $\delta\omega_{\gamma f} \equiv \omega_f + \omega_1 - \omega_{\gamma\alpha}$. Here we assume that $(\sigma_f/\sigma_1)^2 \ll 1$ as well as $\sigma_f^2\alpha \ll 1$, and neglect the higher orders. We can change the integral path from $\int_{-\infty}^{\infty}$ to $\int_{-\infty+Im(\omega'_{fs})}^{\infty+Im(\omega'_{fs})}$ in Eq. 5.45 because the imaginary part of ω'_{fs} is small and the pole can be avoided. For the stationary phase approximation, we must know the value and the second derivative of g on the stationary point:

$$g''(\omega'_{fs}) = \frac{2}{\sigma_1^2} + \frac{2}{\sigma_f^2} - 2i\alpha \tag{5.48}$$

$$g(\omega'_{fs}) \approx \frac{1}{\sigma_1^2}\left(1 - \frac{\sigma_f^2}{\sigma_1^2}\right)(\delta\omega_{\gamma f})^2 - i\alpha(\delta\omega_{\gamma f})^2\left(1 - \frac{2\sigma_f^2}{\sigma_1^2}\right). \tag{5.49}$$

Then Eq. 5.47 can be written as

$$\sum_{f=2}^{3} \frac{-z_{pa}z_{ab}}{2\pi i} |\tilde{E}_1^{(0)}||\tilde{E}_f^{(0)}| e^{i\phi_f} \times \underbrace{\sqrt{\frac{2\pi}{g''(\omega'_{fs})}}}_{①} \underbrace{\exp\left[-g(\omega'_{fs})\right]}_{②} \underbrace{\left[\text{p.v.} \frac{1}{\omega_{\gamma\beta} - \omega'_{fs}}\right]}_{③}, \tag{5.50}$$

where

$$
\begin{aligned}
① &= \sqrt{\pi}\sigma_f \left(1 + \frac{\sigma_f^2}{\sigma_1^2} - i\alpha\sigma_f^2\right)^{-\frac{1}{2}} \approx \sqrt{\pi}\sigma_f \left(1 - \frac{1}{2}\frac{\sigma_f^2}{\sigma_1^2} + \frac{i}{2}\alpha\sigma_f^2\right) \\
② &\approx \exp\left[-\frac{1}{\sigma_1^2}\left(1 - \frac{\sigma_f^2}{\sigma_1^2}\right)(\delta\omega_{\gamma f})^2 + i\alpha(\delta\omega_{\gamma f})^2\left(1 - \frac{2\sigma_f^2}{\sigma_1^2}\right)\right] \\
③ &\approx -\frac{1}{\delta\omega_f}\left[1 + \left(\frac{\sigma_f^2}{\sigma_1^2} - i\sigma_f^2\alpha\right)\frac{\delta\omega_{\gamma f}}{\delta\omega_f}\right],
\end{aligned}
\tag{5.51}
$$

with detuning $\delta\omega_f \equiv \omega_f - \omega_{\gamma\beta}$. The multiplication of these three terms is

$$
\begin{aligned}
① \times ② \times ③ &\approx -\frac{\sqrt{\pi}\sigma_f}{\delta\omega_f}\left[1 + \left(\frac{\delta\omega_{\gamma f}}{\delta\omega_f} - \frac{1}{2}\right)\left(\frac{\sigma_f^2}{\sigma_1^2} - i\alpha\sigma_f^2\right)\right] \\
&\quad \times \exp\left[-\frac{1}{\sigma_1^2}\left(1 - \frac{\sigma_f^2}{\sigma_1^2}\right)(\delta\omega_{\gamma f})^2 + i\alpha(\delta\omega_{\gamma f})^2\left(1 - \frac{2\sigma_f^2}{\sigma_1^2}\right)\right] \\
&\approx -\frac{\sqrt{\pi}\sigma_f}{\delta\omega_f}\left(1 + \frac{1}{2}\frac{\sigma_f^2}{\sigma_1^2}\right)\exp\left[-\frac{1}{\sigma_1^2}\left(1 - \frac{\sigma_f^2}{\sigma_1^2}\right)(\delta\omega_{\gamma f})^2\right] \\
&\quad \times \exp\left[i\alpha(\delta\omega_{\gamma f})^2\left(1 - \frac{2\sigma_f^2}{\sigma_1^2}\right) - i\alpha\sigma_f^2\left(\frac{\delta\omega_{\gamma f}}{\delta\omega_f} - \frac{1}{2}\right)\right]
\end{aligned}
\tag{5.52}
$$

Here the imaginary part in the prefactor in the first line is assumed to be small to be absorbed into the exponential term in order to discuss the phase correction. Here we only consider the correction in the phase term in the last line because the correction in the amplitude part does not change the interference pattern. Therefore, Eq. 5.42 with the use of a Gaussian pump field and a quadratic phase can be rewritten as

$$
\begin{aligned}
S_\gamma^{(2)}(t) &= \sum_{f=2}^{3} \frac{z_{pa}z_{ab}}{2\pi i}\frac{\sqrt{\pi}\sigma_f}{\delta\omega_f}|\tilde{E}_1(\omega_{\gamma\alpha} - \omega_f)||\tilde{E}_f(\omega_f)|e^{i\phi_f} \\
&\quad \times \exp\left[i\alpha(\delta\omega_{\gamma f})^2\left(1 - \frac{2\sigma_f^2}{\sigma_1^2}\right) - i\alpha\sigma_f^2\left(\frac{\delta\omega_{\gamma f}}{\delta\omega_f} - \frac{1}{2}\right)\right]
\end{aligned}
\tag{5.53}
$$

As we apply the symmetric detunning $\delta\omega_2 = -\delta\omega$ and $\delta\omega_3 = \delta\omega$, the interference pattern is proportional to

$$\mathrm{Re}[S^{(2)*}_{\gamma(3,1)} S^{(2)}_{\gamma(2,1)}] \sim \cos\left[4\tilde{\alpha}(\delta\omega)(\omega_{\beta\alpha} - \omega_1) - \phi_{32}\right], \tag{5.54}$$

where the retrieved parameter $\tilde{\alpha}$ including the convolution effect can be written as

$$\tilde{\alpha} \approx \alpha\left(1 - \frac{2\sigma_f^2}{\sigma_1^2} - \frac{\sigma_f^2}{2(\delta\omega)^2}\right) \tag{5.55}$$

with the condition

$$\frac{1}{\sigma_f^2} \gg \frac{1}{(\delta\omega)^2} \gg \alpha, \frac{1}{\sigma_1^2}. \tag{5.56}$$

Eq. 5.55 indicates that $\tilde{\alpha}$ does not change if the unchirped pump pulse is used. It is not surprising because there is no energy-dependence in the convolution integral when the spectral phase is constant. Furthermore, if the pump pulse is chirped, the convolution integral smears out the phase information and the deviation of the retrieved parameter $\tilde{\alpha}$ is proportional to α itself. In the Table 5.1, we list some $\tilde{\alpha}$ and numerical results with several laser parameters. Here $\Delta\omega_1$ and $\Delta\omega_f$ are bandwidth of the pump and probe field such that $\sigma_1 = \Delta\omega_1/\sqrt{(2\ln 2)}$ and $\sigma_f = \Delta\omega_f/\sqrt{(2\ln 2)}$. In addition to removing the probe-induced ATI effect, the accuracy of the retrieved parameters α can be 1 order improved when the convolution effect is considered. The convolution effect can contribute the energy-dependent response time

$$\tau^c_{pb} = \alpha\left(\frac{2\sigma_f^2}{\sigma_1^2} - \frac{\sigma_f^2}{2(\delta\omega)^2}\right)(\omega_{pb} - \omega_1). \tag{5.57}$$

When only the stimulated hole transition is taken into consideration, the effect of τ^c_{pb} compared to $\tau^{(h)}_{pb}$ is presented in Fig. 5.10. Larger α will result in larger linear deviation in $\tau^{(h)}_{pb}$ away from 0 shown in Fig. 5.10 (a). When τ^c_{pb} is subtracted from $\tau^{(h)}_{pb}$, the deviation becomes about 1 order smaller as indicated in Fig. 5.10 (b).

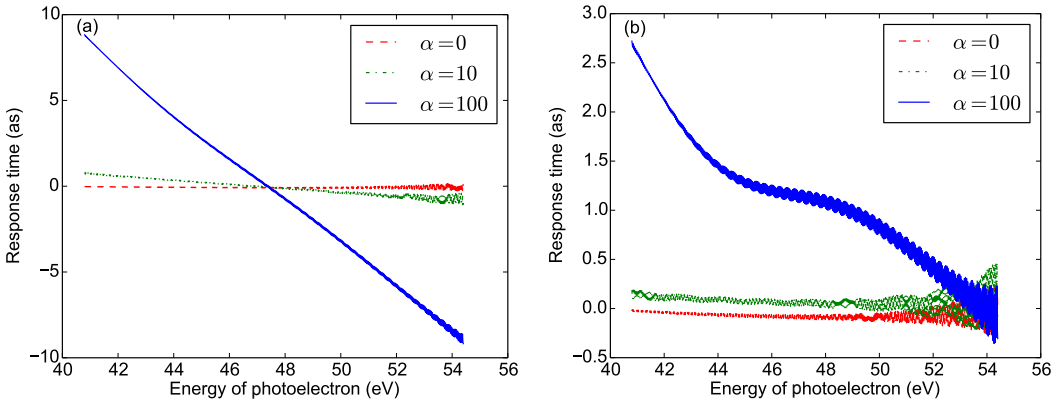

Figure 5.10: (a) The response time $\tau_{pb}^{(h)}$ considering only the hole transition (without ATI effect) for the calculation with $\delta\omega$ = 1eV, $\Delta\omega_1$ = 7.5eV, and $\Delta\omega_f$ = 0.125eV for $\alpha = 1, 10, 100$. (b) The same calculation but subtracting the convolution effect: $\tau_{pb}^{(h)}$-τ_{pb}^{c}.

5.5 The use of inner-core hole and the decay effect

In 5.3, it is indicated that the chosen 2s-2p transition induces the direct ATI transition of the 2s electron by the absorption of both pump and probe pulse. This ATI effect can be closed by adopting a deep core state such as 1s rather than 2p in a neon atom so that the inner electron can not be ionized directly. In Fig. 5.7 (c), we compare τ_{pb}, including the random phase approximation with exchange (RPAE) correlation and both time orders (RPAE + TO). Evidently, the core transition has a much shorter response time. This can be explained by the fact that the (main) electron path no longer goes through the continuum, but instead on a virtual bound excitation,

$$M_{pb,f}^{(\text{elec.})} = \sum_{n'} \frac{z_{pn'} z_{n'p}}{\omega_1' - \epsilon_{n'} + \epsilon_b}, \tag{5.58}$$

where $\omega_1' + \epsilon_b < 0$ for b=1s, as illustrated in Fig. 5.11. In the present calculation we use the real HF energy for the 1s orbital $\epsilon_{1s}^{(\text{HF})}$ = –891.70 eV, which should be valid provided that the pump pulse is sufficiently short compared with the decay lifetime.

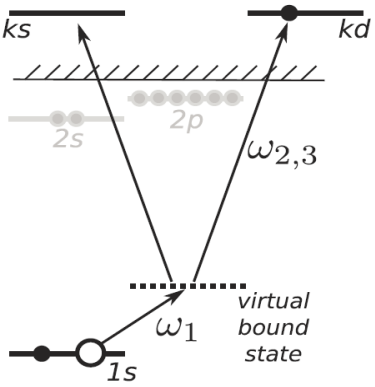

Figure 5.11: Two-photon diagram for stimulated virtual electron transition from a core state, $1s \to n'p \to ks, kd$ in neon atom.

If we want to rake the Auger decay effect into consideration, the CI-doubles should be taken into consideration. Assuming the CI-doubles can be described with a phenomenological decay width Γ, the energy of the many-body state γ can be written as

$$\epsilon_\gamma = \epsilon_\alpha + \epsilon_p - \epsilon_b - i\frac{\Gamma}{2}. \tag{5.59}$$

The second order perturbative amplitude for absorption of one pump photon, 1, and one probe photon, $f = 2$ or 3, in the interaction picture is

$$\begin{aligned} c_\gamma^{(2)}(t) \approx & -\sum_{f=2}^{3}(\frac{1}{i})^2 z_{pb} z_{bc}\left(\frac{-1}{2\pi}\right)^2 \tilde{E}_f \int_{\omega_{\min}}^{\omega_{\max}} d\omega_1' \tilde{E}_1(\omega_1') \\ & \times \int_{-\infty}^{t} dt' \exp\left[i\left(\omega_{\gamma\beta} - \omega_f - i\frac{\Gamma}{2}\right)t'\right] \lim_{\varepsilon\to 0^+} \int_{-\infty}^{t'} dt'' \exp[i(\omega_{\beta\alpha} - \omega_1' + i\varepsilon_1 \mathrm{sgn}(t''))t''] \end{aligned} \tag{5.60}$$

This perturbation amplitude here is defined in the interaction picture and the physically probability should be calculated in the Schrödinger picture. The final expression of the above equation becomes

$$c_\gamma^{(2)}(t) = \sum_{f=2}^{3} \frac{1}{2\pi i} \frac{z_{pb} z_{bc}}{\omega_{\gamma\beta} - \omega_f - i\Gamma/2} \tilde{E}_1(\omega_{\gamma\alpha} - \omega_f - i\Gamma/2)\tilde{E}_f^{(0)}. \tag{5.61}$$

The electric field at the complex frequency results in the distortion of the spectral phase

$$\begin{aligned}\tilde{E}_1(\omega_1 - i\Gamma/2) \approx & \tilde{E}_0 \exp\left[-\mu(\omega_1) + i\frac{\Gamma}{2}\mu'(\omega_1) + i\phi_1(\omega_1) + \frac{\Gamma}{2}\phi_1'(\omega_1)\right] \\ = & |\tilde{E}_1(\omega_1 - i\Gamma/2)| \exp\left[i\left(\phi_1(\omega_1) + \frac{\Gamma}{2}\mu'(\omega_1)\right)\right].\end{aligned} \tag{5.62}$$

The prefactor $1/(\omega_{\gamma\beta} - \omega_f - i\Gamma/2)$ also contributes additional phase $\Theta_\Gamma = \arctan(\Gamma/(2\delta\omega))$. The yield for the final state, $W_\gamma = \lim_{t\to\infty} |c_\gamma^{(2)}(t)e^{-i\epsilon_\gamma t}|^2$, can be written as

$$\begin{aligned}W_\gamma = & \left\{|c^{(2)}_{\gamma,(2,1)}(t)|^2 + |c^{(2)}_{\gamma,(3,1)}(t)|^2 + 2\mathrm{Re}[c^{(2)*}_{\gamma,(3,1)}(t)c^{(2)}_{\gamma,(2,1)}(t)]\right\}\left(\lim_{t\to\infty} e^{-\Gamma t}\right) \\ = & \frac{1}{4\pi^2}\frac{|z_{pb}|^2|z_{bc}|^2}{\delta\omega^2 + (\Gamma/2)^2}\Big\{|\tilde{E}_1(\omega_{\gamma\alpha} - \omega_2 - i\Gamma/2)|^2|\tilde{E}_2^{(0)}|^2 + |\tilde{E}_1(\omega_{\gamma\alpha} - \omega_3 - i\Gamma/2)|^2|\tilde{E}_3^{(0)}|^2 \\ & - 2|E_1(\omega_{\gamma\alpha} - \omega_2 - i\Gamma/2)||\tilde{E}_1(\omega_{\gamma\alpha} - \omega_3 - i\Gamma/2)||\tilde{E}_2^{(0)}||\tilde{E}_3^{(0)}|\cos\theta\Big\}\left(\lim_{t\to\infty} e^{-\Gamma t}\right),\end{aligned} \tag{5.63}$$

where the subscript $(f,1)$ denotes absorption of one photon from the pump field 1 followed by absorption of probe photon f, and $\theta = \phi_1(\omega_{\gamma\alpha} - \omega_2) - \phi_1(\omega_{\gamma\alpha} - \omega_3) + \Gamma(\mu'(\omega_{\gamma\alpha} - \omega_2) - \mu'(\omega_{\gamma\alpha} - \omega_3))/2 + 2\Theta_\Gamma + \phi_2 - \phi_3$ which gives rise to modulations of the yield. The interference pattern can be expressed as the difference in GDs of the pulses and the correction terms due to the decay effect

$$W_\gamma = A_\gamma + B_\gamma \cos\left[2\delta\omega\left(\tau_1^{(\mathrm{GD})}(\omega_{\beta\alpha}) + \frac{\Gamma}{2}\mu''(\omega_{\beta\alpha}) + \frac{\Theta_\Gamma}{\delta\omega} - \tau_{32}^{(\mathrm{GD})}(\omega_{\beta\alpha})\right)\right]. \tag{5.64}$$

It is worth noting that Θ_Γ is a constant and $\mu''(\omega_{\beta\alpha})$ is independent of $\omega_{\beta\alpha}$ if the pulse envelope is a Gaussian. Therefore, the response time has a constant shift

$$\tau_\Gamma = \Gamma\frac{2\ln 2}{(\Delta\omega_1)^2} + \frac{1}{\delta\omega}\arctan\left(\frac{\Gamma}{2\delta\omega}\right). \tag{5.65}$$

In TDCIS, We still use the Neon $2s$ and $2p$ state, but the phenomenological decay term is added in the $2p$ hole configuration. To purely discuss the effect of the decay, the probe field only makes the hole transition in the TDCIS calculation. Fig. 5.12 shows the

response time shift is constant with respect to the energy of photoelectron in the use of a Gaussian-shaped pulse. The results of the response time shift for different parameters is shown in Table 5.2. The decay rate is chosen as 0.27 eV, which is the decay rate of neon 1s hole, and half and quarter of it. The constant shift of the group delay only shifts the pulse in the time domain rather than varying the retrieved temporal structure of the pulse. Therefore, the decay effect of the hole only makes tiny influence on the pulse characterization if it can be treated as a phenomenological decay term in the CI point of view. However, theoretical description based on a phenomenological decay term relies on the time scale of the decay shorter than all other dynamics in the problem [146–148]. For the attosecond pulse charaterization, the time scale of the light-driven dynamics is comparable to or shorter than the decay lifetime. Therefore, more rigorous theory for treating the CI doubles should be considered.

α	$\delta\omega$ (eV)	$\Delta\omega_1$ (eV)	$\Delta\omega_f$ (eV)	Γ (eV)	Response time shift	
					Numerical	Eq. 5.65
0	1	7.5	0.625	0.27	93.5	92.67
0	1	7.5	0.625	0.135	47.05	46.53
0	1	7.5	0.625	0.0675	23.55	23.29
100	1	7.5	0.625	0.27	93.7	92.67

Table 5.2: The Comparison of the response time shift between analytical and numerical calculation with the $2s$ and $2p$ with the different decay rate for $2s$ hole.

In conclusion, with the help of the deep core hole, the error can be reduced to about 1 order smaller compared to the attosecond streak camera as shown in Fig. 5.7 (c). However, in order to extract the desired signal for a single attosecond pulse characterization, we still need to study channel-resolved photoelectrons. More precisely, we need to distinguish between electrons from the unexcited ion (with a 2p hole) and the excited ion (with a 1s or 2s hole). In practice, this is a major drawback of the method because the streak camera does not require any form of coincidence detection. The first coincidence detection schemes combined with attosecond pulses have been reported recently [149–151], but so far no experiments have been reported where the state of the ion has been determined separately from the electron.

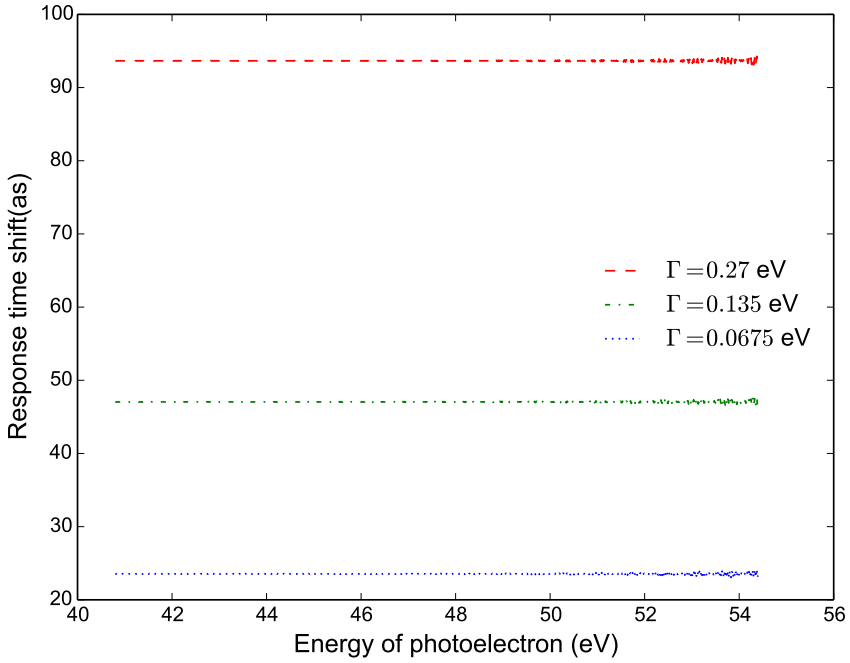

Figure 5.12: (a) The response time shift for different decay rate in the case $\alpha = 0$, $\delta\omega_1 = 1$ eV, $\Delta\omega_1 = 7.5$ eV, $\delta\omega_1 = 1$ eV, $\delta\omega_f = 0.625$ eV and a Gaussian pump pulse.

Chapter 6

Summery and outlook

This thesis covers the topics related to the light induced core-valance dynamics, including the detection of the HHG recombination wavepacket dynamics using inner shell hole, the hole transfer during the tunneling process along the imaginary time, spectral shearing due to the detuning of the resonant transition, and the comparison between the two-photon trnasition matrix element in the photoionization induced by the hole transition and the electron ATI effect.

For the studied HHG spectra produced by a driving IR field combined with XUV pulses, our numerical method – a 1D-model atom usning TDCIS calculation – shows good agreement with the semiclassical SFA model on the production of a second plateau region that maps out the excursion times of electron trajectories driven by the intense laser field. This extended plateau originates from the recombination of a continuum electron with an inner shell hole that is generated by XUV-excitation after tunneling process. The time delay between the XUV pulse and the IR field makes the control of population transfer between the different ionic states. In the case of a single XUV attopulse and a few cycle IR pulse, the single resonant XUV pulse can help us to extract the temporal information of HHG dynamics in the subcycle time-scale, such as ionization rate (intensity of the interference stripes), and ionization and recombination time of the classical trajectory (the start and end of the plateaus). In the region of overlapping attosecond pulse and tunnel ionization time, the plateau as a function of time delay shows a positive slope that was attributed to modified tunneling time due to the XUV field. The XUV-interaction can propagate in imaginary time, which is interpreted as the tunneling process, and induce an additional delay-dependent phase. We stress that when a perturbative field is added based on the SFA model, how this field acts on the quantum tunneling region should be investigated. Moreover, in the

case of using an XUV-APT combined with a flat-top IR field, the second plateau can be increased. The increase of the plateau reveals out of a coherent accumulation of the inner-hole occupation in consequent half cycles. We have shown the robustness of this statement using different phase between successive pulses, and by calculating the time-dependent population on a two-level system driven by resonant short pulse train. Our prediction provides an candidate of HHG spectroscopy for resolving both XUV-driven hole dynamics in attosecond time scale with the use of on table-top HHG sources and at FEL facilities.

We have proposed a new type of pump-probe scheme that relies on stimulated core-valence transitions by two narrow-band detuned XUV or x-ray probe fields and a short XUV pump pulse. To obtain photoelectron spectra, we adopt t-SURFF method to the multichannel 1D-TDCIS formalism. We emphasize that the channel-coupling term cannot be neglected in Chapter 3. Here we applied the method to the characterization of isolated attosecond pulses and we demonstrated the existence of an atomic response time that gives insight into the nature of the stimulated core-valence transitions. In particular, for the stimulated $2p \rightarrow 2s$ hole transition in neon, we found that the response time can be approximated by a ratio between electron continuum transitions and the stimulated hole transition. In practice, the method relies on coincidence detection of electron and ion, which makes it less efficient than existing techniques based on IR sources for pulse characterization. Nonetheless, the method is a natural candidate for future XUV-XUV experiments on table top HHG sources and at FEL facilities, as it presents away to study XUV-XUV/x-ray processes with short pump pulse probed by the sharp frequency bandwidth of the probe fields.

Outlook

This XUV-assisted HHG could be applied to detect the hole dynamics driven by electron correlation. If this core-hole has decayed, the recombination to into the ground state will not happen and the HHG signal of the second plateau is suppressed. Therefore, with the variation of the time delay between the XUV and the IR field, survival probability of the core-hole can be mapped to the intensity of the second plateau. This HHG spectroscopy is applicable to normal Auger decay as well as other decay processes without electron emission such as two-hole one-electron configuration [152] or charge migration in molecules. This scheme is similar to the proposed HHG spectroscopy

[153] based on XUV-initiated high harmonic generation (XIHHG) [133, 154, 155], in which the electron is ionized by XUV pulse rather than the strong field tunneling. Unlike XIHHG, the XUV-assisted HHG presents more theoretical challenge owing to the quantum tunneling process. The correlation driven dynamics occurs since the core-hole is generated and should be included into the stationary phase equation, so this complicates the stationary phase approximation and changes the effective tunneling time. We can speculate that this correlation effect not only make core-hole depletion during the valence electron moving in the continuum but also works complicatedly during the tunneling process.

The proposed scheme STRIDER relies on coincidence detection of electron and the state of ion. The experiment could be performed with the reaction microscopes [156], which are used to separate the photoelectron and the ion in space. Then for the first case with short-lived core-hole such as the 1s hole in neon, the emission of high-energy Auger electron occurs on a femtosecond scale and converts the singly charged ion to the doubly charged ion. And then the ions with different charge can be separated by accelerating them in an electric field. With this proposed experimental scheme, the discussion about the response time due to the Auger decay effect is no longer important because we need the singly charged ion with core-hole decays to final doubly charged ion rather than separate them. For the case of with long-lived hole such as 2s hole in neon, the decay is dominated by the fluorescence on a nanosecond time scale. The use of photoelectron-fluorescence coincidence detection [157] can be applied to resolve different ionic state by comparing the number of fluorescence photon and the singly charged ion.

Besides atoms, the work we study can be also extended to molecules and solids with the additional consideration of potential energy surface or band structure. For example, the HHG phenomena was also discovered in solids [158] using driving IR or terahertz fields. The spectrum was shown to be different in solid and atomic gases, and the microscopic understanding for the difference is still ambiguous. The direct comparison between the HHG from the rare-gas solids, which is considered to a three dimensional atomic array with only weak bonding, and rare gases were presented recently [159]. The experiment shows that the HHG from rare-gas solids exhibit multiple plateaus extending well beyond the atomic limit of the corresponding gas-phase harmonics measured under similar conditions and these structures indicates strong interband

couplings involving multiple single-particle bands. These interband couplings play similar rules to the XUV light coupling in atomic case and both of them results in additional plateau beyond the original cutoff. Our work can provide the potential control scheme in the solid-state HHG and the theoretical description on the SFA model in the solid state version.

Bibliography

[1] H. A. Haus, "Mode-locking of lasers," IEEE J. Sel. Top. Quantum Electron. **6**, 1173 (2000).

[2] D. Strickland and G. Mourou, "Compression of amplified chirped optical pulses," Opt. Commun. **55**, 447 (1985).

[3] P. M. Paul, E. S. Toma, P. Breger, G. Mullot, F. Augé, P. Balcou, H. G. Muller, and P. Agostini, "Observation of a Train of Attosecond Pulses from High Harmonic Generation," Science **292**, 1689 (2001).

[4] M. Drescher, M. Hentschel, R. Kienberger, G. Tempea, C. Spielmann, G. A. Reider, P. B. Corkum, and F. Krausz, "X-ray Pulses Approaching the Attosecond Frontier," Science **291**, 1923 (2001).

[5] O. Tcherbakoff, E. Mével, D. Descamps, J. Plumridge, and E. Constant, "Time-gated high-order harmonic generation," Phys. Rev. A **68**, 043804 (2003).

[6] G. Sansone, E. Benedetti, F. Calegari, C. Vozzi, L. Avaldi, R. Flammini, L. Poletto, P. Villoresi, C. Altucci, R. Velotta, S. Stagira, S. D. Silvestri, and M. Nisoli, "Isolated Single-Cycle Attosecond Pulses," Science **314**, 443 (2006).

[7] J. Mauritsson, P. Johnsson, E. Gustafsson, A. L'Huillier, K. J. Schafer, and M. B. Gaarde, "Attosecond pulse trains generated using two color laser fields," Phys. Rev. Lett. **97**, 013001 (2006).

[8] Z. Chang, "Controlling attosecond pulse generation with a double optical gating," Phys. Rev. A **76**, 051403 (2007).

[9] G. Sansone, L. Poletto, and M. Nisoli, "High-energy attosecond light sources," Nature Photonics **5**, 655 (2011).

[10] K. Zhao, Q. Zhang, M. Chini, Y. Wu, X. Wang, and Z. Chang, "Tailoring a 67 attosecond pulse through advantageous phase mismatch," Opt. Lett. **37**, 3891 (2012).

[11] M. Chini, K. Zhao, and Z. Chang, "The generation, characterization and applications of broadband isolated attosecond pulses," Nat. Photonics **8**, 178 (2014).

[12] P. Corkum, "Plasma perspective on strong field multiphoton ionization," Phys. Rev. Lett. **71**, 1994 (1993).

[13] M. Lewenstein, P. Balcou, M. Y. Ivanov, A. L'Huillier, and P. B. Corkum, "Theory of high-harmonic generation by low-frequency laser fields," Phys. Rev. A **49**, 2117 (1994).

[14] M. Lein, N. Hay, R. Velotta, J. P. Marangos, and P. L. Knight, "Role of the intramolecular phase in high-harmonic generation." Phys. Rev. Lett. **88**, 183903 (2002).

[15] T. Kanai, S. Minemoto, and H. Sakai, "Quantum interference during high-order harmonic generation from aligned molecules." Nature **435**, 470 (2005).

[16] O. Smirnova, Y. Mairesse, S. Patchkovskii, N. Dudovich, D. Villeneuve, P. Corkum, and M. Y. Ivanov, "High harmonic interferometry of multi-electron dynamics in molecules," Nature **460**, 972 (2009).

[17] J. Tate, T. Auguste, H. G. Muller, P. Salières, P. Agostini, and L. F. DiMauro, "Scaling of Wave-Packet Dynamics in an Intense Midinfrared Field," Phys. Rev. Lett. **98**, 013901 (2007).

[18] K. Schiessl, K. L. Ishikawa, E. Persson, and J. Burgdörfer, "Quantum Path Interference in the Wavelength Dependence of High-Harmonic Generation," Phys. Rev. Lett. **99**, 253903 (2007).

[19] P. Colosimo, G. Doumy, C. I. Blaga, J. Wheeler, C. Hauri, F. Catoire, J. Tate, R. Chirla, A. M. March, G. G. Paulus, H. G. Muller, P. Agostini, and L. F. DiMauro, "Scaling strong-field interactions towards the classical limit," Nature Physics **4**, 386 (2008).

[20] M. V. Frolov, N. L. Manakov, and A. F. Starace, "Wavelength Scaling of High-Harmonic Yield: Threshold Phenomena and Bound State Symmetry Dependence," Phys. Rev. Lett. **100**, 173001 (2008).

[21] A. D. Shiner, C. Trallero-Herrero, N. Kajumba, H.-C. Bandulet, D. Comtois, F. Légaré, M. Giguère, J.-C. Kieffer, P. B. Corkum, and D. M. Villeneuve, "Wavelength Scaling of High Harmonic Generation Efficiency," Phys. Rev. Lett. **103**, 073902 (2009).

[22] A.-T. Le, H. Wei, C. Jin, V. N. Tuoc, T. Morishita, and C. Lin, "Universality of Returning Electron Wave Packet in High-Order Harmonic Generation with Midinfrared Laser Pulses," Phys. Rev. Lett. **113**, 033001 (2014).

[23] D. A. G. Deacon, L. R. Elias, J. M. J. Madey, G. J. Ramian, H. A. Schwettman, and T. I. Smith, "First Operation of a Free-Electron Laser," Phys. Rev. Lett. **38**, 892 (1977).

[24] C. Weninger, M. Purvis, D. Ryan, R. A. London, J. D. Bozek, C. Bostedt, A. Graf, G. Brown, J. J. Rocca, and N. Rohringer, "Stimulated Electronic X-Ray Raman Scattering," Phys. Rev. Lett. **111**, 233902 (2013).

[25] L. H. Yu, "Generation of intense uv radiation by subharmonically seeded single-pass free-electron lasers," Phys. Rev. A **44**, 5178 (1991).

[26] Z. T., WangD., C. H., C. H., D. X., D. G., FengC., GuQ., H. M., L. H., L. B., L. G., L. Q., LiuB., PratE., W. T., W. S., Y. R., Y. Y., Z. O., Z. Q., ZhangMe., ZhangMi., ZhangT., Z. P., and Z. G., "First lasing of an echo-enabled harmonic generation free-electron laser," Nature Photonics **6**, 360 (2012).

[27] S. Ackermann, A. Azima, S. Bajt, J. Bödewadt, F. Curbis, H. Dachraoui, H. Delsim-Hashemi, M. Drescher, S. Düsterer, B. Faatz, M. Felber, J. Feldhaus, E. Hass, U. Hipp, K. Honkavaara, R. Ischebeck, S. Khan, T. Laarmann, C. Lechner, T. Maltezopoulos, V. Miltchev, M. Mittenzwey, M. Rehders, J. Rönsch-Schulenburg, J. Rossbach, H. Schlarb, S. Schreiber, L. Schroedter, M. Schulz, S. Schulz, R. Tarkeshian, M. Tischer, V. Wacker, and M. Wieland, "Generation of Coherent 19- and 38-nm Radiation at a Free-Electron Laser Directly Seeded at 38 nm," Phys. Rev. Lett. **111**, 114801 (2013).

[28] I. Jovanovic, "Chirped-Pulse Amplification," Opt. Photonik **5**, 30 (2010).

[29] W. Eberhardt, E. W. Plummer, I. W. Lyo, R. Carr, and W. K. Ford, "Auger-electron ion coincidence studies of soft-x-ray-induced fragmentation of N_2," Phys. Rev. Lett. **58**, 207 (1987).

[30] K. Boyer, T. S. Luk, J. C. Solem, and C. K. Rhodes, "Kinetic energy distributions of ionic fragments produced by subpicosecond multiphoton ionization of N_2," Phys. Rev. A **39**, 1186 (1989).

[31] F. Calegari, D. Ayuso, A. Trabattoni, L. Belshaw, S. De Camillis, S. Anumula, F. Frassetto, L. Poletto, A. Palacios, P. Decleva, J. B. Greenwood, F. Martín, and M. Nisoli, "Ultrafast electron dynamics in phenylalanine initiated by attosecond pulses," Science **346**, 336 (2014).

[32] Z. H. Loh, M. Khalil, R. E. Correa, R. Santra, C. Buth, and S. R. Leone, "Quantum state-resolved probing of strong-field-ionized Xenon atoms using femtosecond high-order harmonic transient absorption spectroscopy," Phys. Rev. Lett. **98**, 143601 (2007).

[33] E. Goulielmakis, Z.-H. Loh, A. Wirth, R. Santra, N. Rohringer, V. S. Yakovlev, S. Zherebtsov, T. Pfeifer, A. M. Azzeer, M. F. Kling, S. R. Leone, and F. Krausz, "Real-time observation of valence electron motion." Nature **466**, 739 (2010).

[34] C. Ott, A. Kaldun, L. Argenti, P. Raith, K. Meyer, M. Laux, Y. Zhang, A. Blättermann, S. Hagstotz, T. Ding, R. Heck, J. Madroñero, F. Martín, and T. Pfeifer, "Reconstruction and control of a time-dependent two-electron wave packet." Nature **516**, 374 (2014).

[35] M. Hentschel, R. Kienberger, C. Spielmann, G. A. Reider, N. Milosevic, T. Brabec, P. Corkum, U. Heinzmann, M. Drescher, and F. Krausz, "Attosecond metrology," Nature **414**, 509 (2001).

[36] J. Itatani, F. Quéré, G. L. Yudin, M. Y. Ivanov, F. Krausz, and P. B. Corkum, "Attosecond Streak Camera," Phys. Rev. Lett. **88**, 173903 (2002).

[37] R. Kienberger, E. Goulielmakis, M. Uiberacker, A. Baltuska, V. Yakovlev, F. Bammer, A. Scrinzi, T. Westerwalbesloh, U. Kleineberg, U. Heinzmann, M. Drescher, and F. Krausz, "Atomic transient recorder," Nature **427**, 817 (2004).

[38] M. Schultze, M. Fieß, N. Karpowicz, J. Gagnon, M. Korbman, M. Hofstetter, S. Neppl, A. L. Cavalieri, Y. Komninos, T. Mercouris, C. A. Nicolaides, R. Pazourek, S. Nagele, J. Feist, J. Burgdörfer, A. M. Azzeer, R. Ernstorfer, R. Kienberger, U. Kleineberg, E. Goulielmakis, F. Krausz, and V. S. Yakovlev, "Delay in Photoemission," Science **328**, 1658 (2010).

[39] M. Drescher, M. Hentschel, R. Kienberger, M. Uiberacker, V. Yakovlev, A. Scrinzi, T. Westerwalbesloh, U. Kleineberg, U. Heinzmann, and F. Krausz, "Time-resolved atomic inner-shell spectroscopy," Nature **419**, 803 (2002).

[40] J. D. Sadler, R. Nathvani, P. Oleśkiewicz, L. A. Ceurvorst, N. Ratan, M. F. Kasim, R. M. G. M. Trines, R. Bingham, and P. A. Norreys, "Compression of X-ray Free Electron Laser Pulses to Attosecond Duration," Sci. Rep. **5**, 16755 (2015).

[41] E. Prat and S. Reiche, "Simple Method to Generate Terawatt-Attosecond X-Ray Free-Electron-Laser Pulses," Phys. Rev. Lett. **114**, 244801 (2015).

[42] HarmandM., CoffeeR., B. R., CholletM., FrenchD., ZhuD., F. M., L. T., MedvedevN., ZiajaB., ToleikisS., and CammarataM., "Achieving few-femtosecond time-sorting at hard X-ray free-electron lasers," Nature Photonics **7**, 215 (2013).

[43] S. Schulz, I. Grguraš, C. Behrens, H. Bromberger, J. T. Costello, M. K. Czwalinna, M. Felber, M. C. Hoffmann, M. Ilchen, H. Y. Liu, T. Mazza, M. Meyer, S. Pfeiffer, P. Prędki, S. Schefer, C. Schmidt, U. Wegner, H. Schlarb, and A. L. Cavalieri, "Femtosecond all-optical synchronization of an X-ray free-electron laser," Nature Communication **6** (2015).

[44] GrgurasI., M. R., BehrensC., MazzaT., K. J., RadcliffeP., DustererS., K. K., K. M., TschentscherTh., C. T., MeyerM., H. C., SchlarbH., and C. L., "Ultrafast X-ray pulse characterization at free-electron lasers," Nature Photonics **6**, 852 (2012).

[45] B. Erk, R. Boll, S. Trippel, D. Anielski, L. Foucar, B. Rudek, S. W. Epp, R. Coffee, S. Carron, S. Schorb, K. R. Ferguson, M. Swiggers, J. D. Bozek, M. Simon, T. Marchenko, J. Küpper, I. Schlichting, J. Ullrich, C. Bostedt,

D. Rolles, and A. Rudenko, "Imaging charge transfer in iodomethane upon x-ray photoabsorption," Science **345**, 288 (2014).

[46] B. K. McFarland, J. P. Farrell, S. Miyabe, F. Tarantelli, A. Aguilar, N. Berrah, C. Bostedt, J. D. Bozek, P. H. Bucksbaum, J. C. Castagna, R. N. Coffee, J. P. Cryan, L. Fang, R. Feifel, K. J. Gaffney, J. M. Glownia, T. J. Martinez, M. Mucke, B. Murphy, A. Natan, T. Osipov, V. S. Petrović, S. Schorb, T. Schultz, L. S. Spector, M. Swiggers, I. Tenney, S. Wang, J. L. White, W. White, and M. Gühr, "Ultrafast X-ray Auger probing of photoexcited molecular dynamics," Nature Communication **5** (2014).

[47] T. R. M. Barends, L. Foucar, A. Ardevol, K. Nass, A. Aquila, S. Botha, R. B. Doak, K. Falahati, E. Hartmann, M. Hilpert, M. Heinz, M. C. Hoffmann, J. Köfinger, J. E. Koglin, G. Kovacsova, M. Liang, D. Milathianaki, H. T. Lemke, J. Reinstein, C. M. Roome, R. L. Shoeman, G. J. Williams, I. Burghardt, G. Hummer, S. Boutet, and I. Schlichting, "Direct observation of ultrafast collective motions in CO myoglobin upon ligand dissociation," Science **350**, 445 (2015).

[48] P. Wernet, K. Kunnus, I. Josefsson, I. Rajkovic, W. Quevedo, M. Beye, S. Schreck, S. Grubel, M. Scholz, D. Nordlund, W. Zhang, R. W. Hartsock, W. F. Schlotter, J. J. Turner, B. Kennedy, F. Hennies, F. M. F. de Groot, K. J. Gaffney, S. Techert, M. Odelius, and A. Fohlisch, "Orbital-specific mapping of the ligand exchange dynamics of Fe(CO)5 in solution," Nature **520**, 78 (2015).

[49] A. A. Lutman, R. Coffee, Y. Ding, Z. Huang, J. Krzywinski, T. Maxwell, M. Messerschmidt, and H.-D. Nuhn, "Experimental Demonstration of Femtosecond Two-Color X-Ray Free-Electron Lasers," Phys. Rev. Lett. **110**, 134801 (2013).

[50] E. Allaria, F. Bencivenga, R. Borghes, F. Capotondi, D. Castronovo, P. Charalambous, P. Cinquegrana, M. B. Danailov, G. De Ninno, A. Demidovich, S. Di Mitri, B. Diviacco, D. Fausti, W. M. Fawley, E. Ferrari, L. Froehlich, D. Gauthier, A. Gessini, L. Giannessi, R. Ivanov, M. Kiskinova, G. Kurdi, B. Mahieu, N. Mahne, I. Nikolov, C. Masciovecchio, E. Pedersoli, G. Penco, L. Raimondi, C. Serpico, P. Sigalotti, S. Spampinati, C. Spezzani, C. Svetina, M. Trovò, and

M. Zangrando, "Two-colour pump–probe experiments with a twin-pulse-seed extreme ultraviolet free-electron laser," Nature Communication **4** (2013).

[51] A. Lutman, F.-J. Decker, J. Arthur, M. Chollet, Y. Feng, J. Hastings, Z. Huang, H. Lemke, H.-D. Nuhn, A. Marinelli, J. Turner, S. Wakatsuki, J. Welch, and D. Zhu, "Demonstration of Single-Crystal Self-Seeded Two-Color X-Ray Free-Electron Lasers," Phys. Rev. Lett. **113**, 254801 (2014).

[52] A. Picon, C. S. Lehmann, C. Bostedt, A. Rudenko, A. Marinelli, T. Osipov, D. Rolles, N. Berrah, C. Bomme, M. Bucher, G. Doumy, B. Erk, K. R. Ferguson, T. Gorkhover, P. J. Ho, E. P. Kanter, B. Krassig, J. Krzywinski, A. A. Lutman, A. M. March, D. Moonshiram, D. Ray, L. Young, S. T. Pratt, and S. H. Southworth, "Hetero-site-specific X-ray pump-probe spectroscopy for femtosecond intramolecular dynamics," Nature Communication **7** (2016).

[53] "Single-Shot Spectroscopy from Keith Nelson Group @MIT," `https://nelson.mit.edu/blog/single-shot-spectroscopy`, accessed: 2016-06-30.

[54] R. Pazourek, S. Nagele, and J. Burgdörfer, "Attosecond chronoscopy of photoemission," Rev. Mod. Phys. **87**, 765 (2015).

[55] K. Klünder, J. M. Dahlström, M. Gisselbrecht, T. Fordell, M. Swoboda, D. Guénot, P. Johnsson, J. Caillat, J. Mauritsson, A. Maquet, R. Taïeb, and A. L'Huillier, "Probing Single-Photon Ionization on the Attosecond Time Scale," Phys. Rev. Lett. **106**, 143002 (2011).

[56] C. H. Zhang and U. Thumm, "Streaking and Wigner time delays in photoemission from atoms and surfaces," Phys. Rev. A **84**, 33401 (2011).

[57] J. M. Dahlström, A. L'Huillier, and A. Maquet, "Introduction to attosecond delays in photoionization," J. Phys. B At. Mol. Opt. Phys. **45**, 183001 (2012).

[58] J. M. Dahlström, T. Carette, and E. Lindroth, "Diagrammatic approach to attosecond delays in photoionization," Phys. Rev. A **86**, 061402 (2012), arXiv:1211.2654 .

[59] J. M. Dahlström, D. Guénot, K. Klünder, M. Gisselbrecht, J. Mauritsson, a. L'Huillier, a. Maquet, and R. Taïeb, "Theory of attosecond delays in laser-assisted photoionization," Chem. Phys. **414**, 53 (2013), arXiv:1112.4144 .

[60] E. P. Wigner, "Lower Limit for the Energy Derivative of the Scattering Phase Shift," Phys. Rev. **98**, 145 (1955).

[61] C. A. A. de Carvalho and H. M. Nussenzveig, "Time delay," Phys. Rep. **364**, 83 (2002).

[62] L. V. Keldysh, "Ionization in the field of a string electromagnetic wave," J. Exp. Theor. Phys. **20**, 1307 (1965).

[63] A. S. Landsman and U. Keller, "Attosecond science and the tunnelling time problem," Phys. Rep. **547**, 1 (2015).

[64] K. C. Kulander, "Time-dependent theory of multiphoton ionization of xenon," Phys. Rev. A **38**, 778 (1988).

[65] J. Javanainen, J. H. Eberly, and Q. Su, "Numerical simulations of multiphoton ionization and above-threshold electron spectra," Phys. Rev. A **38**, 3430 (1988).

[66] K. C. Kulander and B. W. Shore, "Calculations of Multiple-Harmonic Conversion of 1064-nm Radiation in Xe," Phys. Rev. Lett. **62**, 524 (1989).

[67] M. Lewenstein, K. C. Kulander, K. J. Schafer, and P. H. Bucksbaum, "Rings in above-threshold ionization: A quasiclassical analysis," Phys. Rev. A **51**, 1495 (1995).

[68] D. N. Fittinghoff, P. R. Bolton, B. Chang, and K. C. Kulander, "Observation of nonsequential double ionization of helium with optical tunneling," Phys. Rev. Lett. **69**, 2642 (1992).

[69] B. Walker, B. Sheehy, L. F. DiMauro, P. Agostini, K. J. Schafer, and K. C. Kulander, "Precision Measurement of Strong Field Double Ionization of Helium," Phys. Rev. Lett. **73**, 1227 (1994).

[70] V. P. Majety and A. Scrinzi, "Dynamic Exchange in the Strong Field Ionization of Molecules," Phys. Rev. Lett. **115**, 103002 (2015).

[71] N. Rohringer and R. Santra, "Multichannel coherence in strong-field ionization," Phys. Rev. A **79**, 053402 (2009).

[72] P. Hohenberg and W. Kohn, "Inhomogeneous Electron Gas," Phys. Rev. **136**, B864 (1964).

[73] W. Kohn and L. J. Sham, "Self-Consistent Equations Including Exchange and Correlation Effects," Phys. Rev. **140**, A1133 (1965).

[74] E. Runge and E. K. U. Gross, "Density-Functional Theory for Time-Dependent Systems," Phys. Rev. Lett. **52**, 997 (1984).

[75] M. Petersilka, U. J. Gossmann, and E. K. U. Gross, "Excitation Energies from Time-Dependent Density-Functional Theory," Phys. Rev. Lett. **76**, 1212 (1996).

[76] O. V. Gritsenko, S. J. A. van Gisbergen, A. Görling, and E. J. Baerends, "Excitation energies of dissociating H2: A problematic case for the adiabatic approximation of time-dependent density functional theory," J. Chem. Phys. **113** (2000).

[77] M. E. Casida, F. Gutierrez, J. Guan, F.-X. Gadea, D. Salahub, and J.-P. Daudey, "Charge-transfer correction for improved time-dependent local density approximation excited-state potential energy curves: Analysis within the two-level model with illustration for H2 and LiH," J. Chem. Phys. **113** (2000).

[78] F. Aryasetiawan, O. Gunnarsson, and A. Rubio, "Excitation energies from time-dependent density-functional formalism for small systems," EPL (Europhysics Lett. **57**, 683 (2002).

[79] C. M. Isborn, B. D. Mar, B. F. E. Curchod, I. Tavernelli, and T. J. Martínez, "The Charge Transfer Problem in Density Functional Theory Calculations of Aqueously Solvated Molecules," J. Phys. Chem. B **117**, 12189 (2013).

[80] O. V. Gritsenko and E. J. Baerends, "Time-dependent Dyson orbital theory," Phys. Chem. Chem. Phys. (2016), 10.1039/C6CP00888G.

[81] A. Szabo and N. S. Ostlund, *Modern Quantum Chemistry* (Dover, Minnesota, 1996).

[82] T. Koopmans, "Über die Zuordnung von Wellenfunktionen und Eigenwerten zu den Einzelnen Elektronen Eines Atoms," Physica **1**, 104 (1934).

[83] N. Rohringer, A. Gordon, and R. Santra, "Configuration-interaction-based time-dependent orbital approach for ab initio treatment of electronic dynamics in a strong optical laser field," Phys. Rev. A **74**, 043420 (2006).

[84] J. B. Foresman, M. Head-Gordon, J. A. Pople, and M. J. Frisch, "Toward a systematic molecular orbital theory for excited states," J. Phys. Chem. **96**, 135 (1992).

[85] T. Klamroth, "Optimal control of ultrafast laser driven many-electron dynamics in a polyatomic molecule: N-methyl-6-quinolone," J. Chem. Phys. **124**, 144310 (2006).

[86] S. Klinkusch, T. Klamroth, and P. Saalfrank, "Long-range intermolecular charge transfer induced by laser pulses: an explicitly time-dependent configuration interaction approach," Phys. Chem. Chem. Phys. **11**, 3875 (2009).

[87] S. Pabst, L. Greenman, P. J. Ho, D. a. Mazziotti, and R. Santra, "Decoherence in Attosecond Photoionization," Phys. Rev. Lett. **106**, 053003 (2011).

[88] S. Pabst and R. Santra, "Strong-Field Many-Body Physics and the Giant Enhancement in the High-Harmonic Spectrum of Xenon," Phys. Rev. Lett. **111**, 233005 (2013).

[89] S. Pabst, M. Lein, and H. J. Wörner, "Preparing attosecond coherences by strong-field ionization," Phys. Rev. A **93**, 023412 (2016).

[90] L. Tao and A. Scrinzi, "Photo-electron momentum spectra from minimal volumes: the time-dependent surface flux method," New J. Phys. **14**, 013021 (2012).

[91] A. Scrinzi, "t -SURFF: fully differential two-electron photo-emission spectra," New J. Phys. **14**, 085008 (2012).

[92] V. P. Majety, A. Zielinski, and A. Scrinzi, "Mixed gauge in strong laser-matter interaction," (2014), arXiv:arXiv:1408.6309v1 .

[93] A. Scrinzi, "Photo-ElectronMomentum Spectra in Strong Laser-Matter Interactions," in *Prog. Ultrafast Intense Laser Sci. Vol. XI* (2015).

[94] A. Karamatskou, S. Pabst, Y.-J. Chen, and R. Santra, "Calculation of photoelectron spectra within the time-dependent configuration-interaction singles scheme," Phys. Rev. A **89**, 033415 (2014).

[95] J. A. You, N. Rohringer, and J. M. Dahlström, "Attosecond photoionization dynamics with stimulated core-valence transitions," Phys. Rev. A **93**, 033413 (2016), arXiv:1508.00760 .

[96] J. A. You, J. M. Dahlström, and N. Rohringer, "Attosecond dynamics of light-induced resonant hole transfer in high harmonic generation," Submitted to Phys. Rev. A .

[97] P. A. Franken, A. E. Hill, C. W. Peters, and G. Weinreich, "Generation of optical harmonics," Phys. Rev. Lett. **7**, 118 (1961).

[98] G. H. C. New and J. F. Ward, "Optical Third-Harmonic Generation in Gases," Phys. Rev. Lett. **19**, 556 (1967).

[99] A. McPherson, G. Gibson, H. Jara, U. Johann, T. S. Luk, I. A. McIntyre, K. Boyer, and C. K. Rhodes, "Studies of multiphoton production of vacuum-ultraviolet radiation in the rare gases," J. Opt. Soc. Am. B **4**, 595 (1987).

[100] M. Ferray, A. L'Huillier, X. F. Li, L. A. Lomprke, G. Mainfray, and C. Manus, "Multiple-harmonic conversion of 1064 nm radiation in rare gases," J. Phys. B At. Mol. Opt. Phys. **21**, L31 (1988).

[101] P. B. Corkum, N. H. Burnett, and F. Brunel, "Above-threshold ionization in the long-wavelength limit," Phys. Rev. Lett. **62**, 1259 (1989).

[102] J. Krause, K. Schafer, and K. Kulander, "High-order harmonic generation from atoms and ions in the high intensity regime," Phys. Rev. Lett. **68**, 3535 (1992).

[103] K. J. Schafer, M. B. Gaarde, A. Heinrich, J. Biegert, and U. Keller, "Strong Field Quantum Path Control Using Attosecond Pulse Trains," Phys. Rev. Lett. **92**, 23003 (2004).

[104] L. E. Chipperfield, J. S. Robinson, J. W. G. Tisch, and J. P. Marangos, "Ideal Waveform to Generate the Maximum Possible Electron Recollision Energy for Any Given Oscillation Period," Phys. Rev. Lett. **102**, 63003 (2009).

[105] I. A. Ivanov and A. S. Kheifets, "Tailoring the waveforms to extend the high-order harmonic generation cutoff," Phys. Rev. A **80**, 23809 (2009).

[106] Z. Chang, A. Rundquist, H. Wang, M. Murnane, and H. Kapteyn, "Generation of Coherent Soft X Rays at 2.7 nm Using High Harmonics," Phys. Rev. Lett. **79**, 2967 (1997).

[107] C. Spielmann, "Generation of Coherent X-rays in the Water Window Using 5-Femtosecond Laser Pulses," Science **278**, 661 (1997).

[108] M.-C. Chen, P. Arpin, T. Popmintchev, M. Gerrity, B. Zhang, M. Seaberg, D. Popmintchev, M. M. Murnane, and H. C. Kapteyn, "Bright, Coherent, Ultrafast Soft X-Ray Harmonics Spanning the Water Window from a Tabletop Light Source," Phys. Rev. Lett. **105**, 173901 (2010).

[109] P. Salières, A. L'Huillier, and M. Lewenstein, "Coherence control of high-order harmonics," Phys. Rev. Lett. **74**, 3776 (1995).

[110] A. Rundquist, C. G. D. Iii, Z. Chang, C. Herne, S. Backus, M. M. Murnane, H. C. Kapteyn, C. G. Durfee, Z. Chang, C. Herne, S. Backus, M. M. Murnane, and H. C. Kapteyn, "Phase-Matched Generation of Coherent Soft X-rays," Science (80-.). **280**, 1412 (1998).

[111] C. G. D. Iii, A. R. Rundquist, S. Backus, C. Herne, M. M. Murnane, H. C. Kapteyn, C. G. Durfee, A. R. Rundquist, S. Backus, C. Herne, M. M. Murnane, and H. C. Kapteyn, "Phase Matching of High-Order Harmonics in Hollow Waveguides," Phys. Rev. Lett. **83**, 2187 (1999).

[112] T. Popmintchev, M.-C. Chen, D. Popmintchev, P. Arpin, S. Brown, S. Ališauskas, G. Andriukaitis, T. Balciunas, O. D. Mücke, A. Pugzlys, A. Baltuska, B. Shim, S. E. Schrauth, A. Gaeta, C. Hernández-García, L. Plaja, A. Becker, A. Jaron-Becker, M. M. Murnane, and H. C. Kapteyn, "Bright coherent ultrahigh harmonics in the keV x-ray regime from mid-infrared femtosecond lasers." Science **336**, 1287 (2012).

[113] M. J. J. Vrakking, "Attosecond imaging," Phys. Chem. Chem. Phys. **16**, 2775 (2014).

[114] E. Goulielmakis, M. Schultze, M. Hofstetter, V. S. Yakovlev, J. Gagnon, M. Uiberacker, A. L. Aquila, E. M. Gullikson, D. T. Attwood, R. Kienberger, F. Krausz, and U. Kleineberg, "Single-Cycle Nonlinear Optics," Science **320**, 1614 (2008).

[115] H. Mashiko, S. Gilbertson, M. Chini, X. Feng, C. Yun, H. Wang, S. D. Khan, S. Chen, and Z. Chang, "Extreme ultraviolet supercontinua supporting pulse durations of less than one atomic unit of time." Opt. Lett. **34**, 3337 (2009).

[116] M. Chini, S. Gilbertson, S. D. Khan, and Z. Chang, "Characterizing ultrabroadband attosecond lasers." Opt. Express **18**, 13006 (2010).

[117] M. Hofstetter, M. Schultze, M. Fieß, B. Dennhardt, A. Guggenmos, J. Gagnon, V. S. Yakovlev, E. Goulielmakis, R. Kienberger, E. M. Gullikson, F. Krausz, and U. Kleineberg, "Attosecond dispersion control by extreme ultraviolet multilayer mirrors," Opt. Express **19**, 1767 (2011).

[118] L. D. Landau and E. Lifshitz, *Quantum Mechanics: Non-relativistic Theory*, 3rd ed. (Oxford: Pergamon, 1977).

[119] J. J. Sakurai, *Modern Quantum Mechanics* (Addison-Wesley, 1994).

[120] M. Y. Ivanov, M. Spanner, and O. Smirnova, "Anatomy of strong field ionization," J. Mod. Opt. **52**, 165 (2005).

[121] A. Gordon and F. X. Kärtner, "Quantitative modeling of single atom high harmonic generation," Phys. Rev. Lett. **95**, 223901 (2005).

[122] G. F. Gribakin and M. Y. Kuchiev, "Multiphoton detachment of electrons from negative ions," Phys. Rev. A **55**, 3760 (1997).

[123] M. Y. Ivanov, T. Brabec, and N. Burnett, "Coulomb corrections and polarization effects in high-intensity high-harmonic emission," Phys. Rev. A **54**, 742 (1996).

[124] M. V. Ammosov, N. B. Delone, and V. P. Krainov, "Tunnel ionization of complex atoms and of atomic ions in an alternating electromagnetic field," Sov. Phys. JETP **64**, 1191 (1986).

[125] U. Schwengelbeck and F. H. M. Faisal, "Ionization of the one-dimensional Coulomb atom in an intense laser field," Phy. Rev. A **50**, 632 (1994).

[126] J. Javanainen, J. H. Eberly, and Q. Su, "Numerical Simulations of Multiphoton Ionization and Above-threshold Electron Spectra," Phy. Rev. A **38**, 3430 (1988).

[127] K. Blum, *Density Matrix Theory and Applications* (Plenum, new York, 1996).

[128] N. Rohringer and R. Santra, "Strongly driven resonant Auger effect treated by an open-quantum-system approach," Phys. Rev. A **86**, 043434 (2012).

[129] A. Karamatskou, S. Pabst, Y. J. Chen, and R. Santra, "Calculation of photoelectron spectra within the time-dependent configuration-interaction singles scheme," Phys. Rev. A **89**, 033415 (2014), arXiv:1403.0352 .

[130] C. de Morisson Faria, M. Dörr, W. Becker, and W. Sandner, "Time-frequency analysis of two-color high-harmonic generation," Phys. Rev. A **60**, 1377 (1999).

[131] C. de Morisson Faria, D. B. š\fievi\ifmmode \acutec\else ć\fi, and G. G. Paulus, "Phase-dependent effects in bichromatic high-order harmonic generation," Phys. Rev. A **61**, 63415 (2000).

[132] K. T. Kim, D. M. Villeneuve, and P. B. Corkum, "Manipulating quantum paths for novel attosecond measurement methods," Nat Phot. **8**, 187 (2014).

[133] M. B. Gaarde, K. J. Schafer, A. Heinrich, J. Biegert, and U. Keller, "Large enhancement of macroscopic yield in attosecond pulse train–assisted harmonic generation," Phys. Rev. A **72**, 013411 (2005).

[134] E. J. Takahashi, T. Kanai, K. L. Ishikawa, Y. Nabekawa, and K. Midorikawa, "Dramatic Enhancement of High-Order Harmonic Generation," Phys. Rev. Lett. **99**, 53904 (2007).

[135] F. Brizuela, C. M. Heyl, P. Rudawski, D. Kroon, L. Rading, J. M. Dahlström, J. Mauritsson, P. Johnsson, C. L. Arnold, and a. L'Huillier, "Efficient high-order harmonic generation boosted by below-threshold harmonics." Sci. Rep. **3**, 1410 (2013).

[136] C. Buth, M. C. Kohler, J. Ullrich, and C. H. Keitel, "High-order harmonic generation enhanced by XUV light," Opt. Lett. **36**, 3530 (2011).

[137] C. Buth, F. He, J. Ullrich, C. H. Keitel, and K. Z. Hatsagortsyan, "Attosecond pulses at kiloelectronvolt photon energies from high-order-harmonic generation with core electrons," Phys. Rev. A **88**, 033848 (2013).

[138] M. C. Kohler, C. Müller, C. Buth, A. B. Voitkiv, K. Z. Hatsagortsyan, J. Ullrich, T. Pfeifer, and C. H. Keitel, "Electron Correlation and Interference Effects in Strong-Field Processes BT - Multiphoton Processes and Attosecond Physics: Proceedings of the 12th International Conference on Multiphoton Processes (ICOMP12) and the 3rd International Conference on Attosecond Physics (ATTO3)," (Springer Berlin Heidelberg, Berlin, Heidelberg, 2012) pp. 209–217.

[139] C. A. Haworth, L. E. Chipperfield, J. S. Robinson, P. L. Knight, J. P. Marangos, and J. W. G. Tisch, "Half-cycle cutoffs in harmonic spectra and robust carrier-envelope phase retrieval," Nature Physics **3**, 52 (2006).

[140] N. Ishii, S. Adachi, Y. Nomura, A. Kosuge, and Y. Kobayashi, "Generation of soft x-ray and water window harmonics optical parametric chirped-pulse amplifier," Optics Letters **37**, 97 (2012).

[141] N. Ishii, K. Kaneshima, K. Kitano, T. Kanai, S. Watanabe, and J. Itatani, "Carrier-envelope phase-dependent high harmonic generation in the water window using few-cycle infrared pulses." Nature Communications **5**, 3331 (2014).

[142] V. Averbukh, U. Saalmann, and J. M. Rost, "Suppression of Exponential Electronic Decay in a Charged Environment," Phys. Rev. Lett. **104**, 233002 (2010).

[143] N. Dudovich, O. Smirnova, J. Levesque, Y. Mairesse, M. Y. Ivanov, D. M. Villeneuve, and P. B. Corkum, "Measuring and controlling the birth of attosecond XUV pulses," Natature Physics **2**, 781 (2006).

[144] J. M. Dahlström, A. L'Huillier, and J. Mauritsson, "Quantum mechanical approach to probing the birth of attosecond pulses using a two-colour field," J. Phys. B At. Mol. Opt. Phys. **44**, 095602 (2011), arXiv:1102.1291 .

[145] S. Zhdanovich, E. Shapiro, M. Shapiro, J. Hepburn, and V. Milner, "Population Transfer between Two Quantum States by Piecewise Chirping of Femtosecond Pulses: Theory and Experiment," Phys. Rev. Lett. **100**, 103004 (2008).

[146] V. S. Yakovlev, *Extremely short light pulses: generation, diagnostics, and application in attosecond spectroscopy*, Ph.D. thesis, Technischen Universität Wien (2003).

[147] C. Buth and R. Santra, "Theory of x-ray absorption by laser-aligned symmetric-top molecules," Phys. Rev. A **77**, 013413 (2008).

[148] C. Buth and K. Schafer, "Theory of Auger decay by laser-dressed atoms," Phys. Rev. A **80**, 033410 (2009).

[149] P. Ranitovic, X. M. Tong, C. W. Hogle, X. Zhou, Y. Liu, N. Toshima, M. M. Murnane, and H. C. Kapteyn, "Laser-Enabled Auger Decay in Rare-Gas Atoms," Phys. Rev. Lett. **106**, 053002 (2011).

[150] E. P. Mansson, D. Guenot, C. L. Arnold, D. Kroon, S. Kasper, J. M. Dahlstrom, E. Lindroth, A. S. Kheifets, A. L/'Huillier, S. L. Sorensen, and M. Gisselbrecht, "Double ionization probed on the attosecond timescale," Nature Physics **10**, 207 (2014).

[151] M. Sabbar, S. Heuser, R. Boge, M. Lucchini, L. Gallmann, C. Cirelli, and U. Keller, "Combining attosecond XUV pulses with coincidence spectroscopy," Rev. Sci. Instrum. **85** (2014).

[152] L. S. Cederbaum, W. Domcke, J. Schirmer, and W. von Niessen, "Correlation Effects in the Ionization of Molecules: Breakdown of the Molecular Orbital Picture," Adv. Chem. Phys. **LXV**, 115 (1986).

[153] J. Leeuwenburgh, B. Cooper, V. Averbukh, J. P. Marangos, and M. Ivanov, "High-Order Harmonic Generation Spectroscopy of Correlation-Driven Electron Hole Dynamics," Phys. Rev. Lett. **111**, 123002 (2013).

[154] J. Biegert, A. Heinrich, C. P. Hauri, W. Kornelis, P. Schlup, M. P. Anscombe, M. B. Gaarde, K. J. Schafer, and U. Keller, "Control of high-order harmonic emission using attosecond pulse trains," J. Mod. Opt. **53**, 87 (2006).

[155] G. Gademann, F. Kelkensberg, W. K. Siu, P. Johnsson, M. B. Gaarde, K. J. Schafer, and M. J. J. Vrakking, "Attosecond control of electron–ion recollision in high harmonic generation," New J. Phys. **13**, 033002 (2011).

[156] J. U. Schmidt-Böcking, R. Moshammer, A. Dorn, R. Dörner, L. P. H. Schmidt, and H, "Recoil-ion and electron momentum spectroscopy: reaction-microscopes," Reports Prog. Phys. **66**, 1463 (2003).

[157] J.-E. Rubensson, J. Lüning, M. Neeb, B. Küpper, S. Eisebitt, and W. Eberhardt, "Photoelectron Soft X-Ray Fluorescence Coincidence Spectroscopy on Free Molecules," Phys. Rev. Lett. **76**, 3919 (1996).

[158] S. Ghimire, A. D. DiChiara, E. Sistrunk, P. Agostini, L. F. DiMauro, and D. A. Reis, "Observation of high-order harmonic generation in a bulk crystal," Nature Physics **7**, 138 (2011).

[159] G. Ndabashimiye, S. Ghimire, M. Wu, D. A. Browne, K. J. Schafer, M. B. Gaarde, and D. A. Reis, "Solid-state harmonics beyond the atomic limit," Nature **advance on** (2016).

Acknowledgements

I would like to thank my supervisor Dr. Nina Rohringer for giving me an opportunity to do my PhD research. It has been and I learned a lot of things during these years. She is always very patient to my speaking with a stammer and immature opinions. Her requests for the accuracy of my writing and my speaking during the discussion always inspire me more deeply thinking.

I would also like to thank all of the group members that I worked with and shared many good life with: Clemens Weninger, who can always solve computer problems and remind me many duties; Song-Bin Zhang, who likes to share me the new paper he reads and some ideas; Victor Kimberg, who teaches me how to work more efficiently; Marcus Dahlström, who works the same projects together with me and we have good time of our cooperation. I am indebted to his fruitful experience and knowledge of attosecond science; Felix Aviat, who often brings us some interesting discussions; Wen-Te Liao, who gives me many useful suggestions on academic career; Laurent Mercadier, who always answers my questions about experiments; and Miguel Silva, whose active attitude often inspires motivation on me.

I also appreciate Anna-Maria Bartsch's help for reminding me some linguistic mistakes in my thesis. As a non-scientist, it is very kind of her to spend extra time on doing this work.

I am thankful for all the people I met in CFEL, and all PhD fellows in the graduate school for our every moment, including courses, PhD seminars, retreats, and social events. I would like to thank our successive IMPRS-UFAST Coordinators – Anja Bleidorn, Sonia Utermann and Julia Quante – for much kindly help.

I wish to thank my landlord Steffen Edler for helping me many duties and giving me high quality life in Hamburg.

I also thank all the friends who encourage, assist, or amuse me.

Finally, I am sincerely grateful to my family. With your support and encouragement, I am able to concentrate on my study, my work and all of my decisions.

Eidesstattliche Versicherung

Hiermit erkläre ich an Eides statt, dass ich die vorliegende Dissertationsschrift selbst verfasst und keine anderen als die angegebenen Quellen und Hilfsmittel benutzt habe.

Hamburg, den ....

(Jhih-An You)